

In situ monitoring of femtosecond laser-induced modifications in dielectrics

Présentée le 2 juin 2023

Faculté des sciences et techniques de l'ingénieur
Laboratoire Galatea
Programme doctoral en manufacturing

pour l'obtention du grade de Docteur ès Sciences

par

Olivier BERNARD

Acceptée sur proposition du jury

Prof. C. Moser, président du jury
Prof. Y. Bellouard, directeur de thèse
Prof. S. Nolte, rapporteur
Dr F. Courvoisier, rapporteur
Prof. J.-É. Moser, rapporteur

Nous sommes de grands fols : « Il a passé sa vie en oisiveté », disons nous ; « je n'ay rien faict d'aujourd'huy. » Quoy, avez vous pas vescu ? C'est non seulement la fondamentale
mais la plus illustre de vos occupations.

We are great fools. 'He has passed his life in idleness,' say we: 'I have done nothing to-day.' What? have you not lived? that is not only the fundamental, but the most illustrious, of your occupations.

— Montaigne, Essais, III, XIII, De l'Expérience (1595)

à ma famille, à mes ami-x-es . . .

Remerciements / acknowledgements

Pour conclure ces quatre belles années et demi de thèse, je souhaite dédier ces quelques pages personnelles à toutes les belles personnes qui m'ont accompagnées, de mes balbutiements dans le monde de l'optique ultrarapide jusqu'à aujourd'hui.

To conclude these four and a half years of PhD, I wish to dedicate these few personal pages to all the kind people who accompanied me, from my beginnings in the world of ultrafast optics to today.

Je remercie infiniment mon directeur de thèse, le Pr Yves Bellouard, pour l'excellent encadrement qu'il m'a fourni ; ainsi que la grande confiance qu'il m'a accordée pour réaliser mes projets de thèse – aussi bien de son initiative que de la mienne, pour la tenue du laboratoire (*le chaos naturel des femtos*) et dans le cadre de l'enseignement. Je ne peux que saluer l'effort qu'il consacre depuis tant d'années au laboratoire, à l'encadrement des doctorant-es et des étudiant-es, ainsi qu'à ses enseignements. *Avocat du diable* par excellence, son « scepticisme positiviste » est une douleur constante mais si formatrice qui n'épargne personne – dans un monde qui va toujours trop vite en faisant trop souvent fi de la rigueur et au recul, pourtant si nécessaire à la science.

I also thank the jury for my thesis: Professors Christophe Moser, Jacques-Édouard Moser, Stefan Nolte, and Dr François Courvoisier, for their interest in this work, and the fruitful discussions during the oral exam.

I wish to acknowledge thereafter the whole staff of Galatea laboratory, my colleagues, with whom I spent close to one sixth (!) of my life: first of all my PhD cohort, Drs.-to-be Ruben 'Pottok' Ricca and Gözden 'Gözdude' Torun ; and all the others I met in a somewhat chronological order: Dr. 'sjef Piet' Vlugter, Sacha Pollonghini, Dr. Julien Gâteau, Dr. Sargis '93' Hakobyan, Dr. Arun Radhakrishnan, Samuel Benketaf, Dr. Saood Nazir, Dr. 'Enri' Casamenti, David Lambelet, Samuel Rey, Dr. Margarita Lesik, Dr. Manon Tardif, Dr. Antoine Delgoffe, Ernesto Gribaudo, Dr. Benedikt Herrman, Dr Daniel Talán Echarri. Thank you all for having kept a thriving research environment with fruitful collaborations, and for all the great moments we have spent together! I give special shout outs to more direct collaborators: Dr. Assim Boukhayma (ex-ICLAB) – who designed the CMOS sensor I used so much in this thesis work, Dr. Andrea Kraemer (ex-ICLAB) – who implemented it, Ruben Ricca – the nano-surgeon, for the collaboration on multilayered materials and dedicating himself to the beer club, Gözden Torun and Dr. Pieter Vlugter, for their encyclopedic knowledge on so many types of glass, and Dr. Benedikt Hermann, for the collaboration on UV-processing and insane ultrafast physics discussions.

Je souhaite ensuite remercier mes encadrant-es qui m'ont amené jusque-là, par ordre chronologique. Je remercie tout d'abord le Pr Dilhaire et le Dr d'Acremont (LOMA, Uni Bordeaux, France) pour l'introduction au monde des laser femtosecondes, avec le lot de réalignement quotidien des oscillateurs. Je remercie ensuite le Dr Setzpfandt (IAP, Uni

Remerciements / acknowledgements

Jena, Allemagne) pour m'avoir introduit à l'optique non-linéaire et intégrée, cette fois avec le lot d'alignement dans des guides d'onde. Enfin, je remercie les Drs Hönninger et Audouard pour m'avoir engagé à Amplitude Systèmes pour faire mon mémoire de master sur de la modélisation, à mes collègues de l'époque pour l'encadrement et la bonne ambiance, tout particulièrement le Dr Bonamis. Je remercie tout particulièrement les Drs Inka Manek-Hönninger et Clemens Hönninger de m'avoir guidé dans cette carrière que je n'aurais su imaginer pendant mes années de master.

Je donne un mot pour mes camarades de physique de l'UBx-I, avec qui on s'est connu pour la plupart sur les bancs grinçants de première année de licence: Olivier « la Pliche », Charles, Dr Xanti, Dr Boju, Marlet, Dorsaf, Xavier, Ferzu et tant d'autres. Je donne un autre mot à mes copaines de Suisse, de Lôz'Angeles, Neuch ou Genf, qui m'ont accompagné, fait découvrir et aimer mon pays d'accueil : Ric mv, Kayus, Marco, Willy le Coon, Maître Kimbo, Ol Watts, Els, Chardon, Anaïs, Jesse, Dr-à-être Dall'Alba (coloc de rêve), Isildur, Luigi, Rémi. Je donne un dernier mot spécial pour mes compères bordeluches à Lôz: Dr-à-être Lucas, Cha (coloc de rêve), et Maître Dupuch.

Merci à vous toutes et tous ! *Thank you all!*

Lausanne, 16 mars 2023

O. B.

Abstract

Over the last decades, the progress made in the generation of laser pulses shorter than a picosecond (10^{-12} s) has allowed us to reach extreme optical power intensities exceeding 10^{15} W cm $^{-2}$. This tremendous power has triggered an abundance of original scientific and industrial applications. Chief amongst them is material processing, and in particular, in-volume processing of transparent materials, which motivates the present work. Femtosecond lasers induce a rich taxonomy of material modifications that can take diverse forms, including: smooth densification, self-organised nanogratings, localised crystallisation, or amorphisation; that will vary in the processing parameter space, and from one material to another.

To date, effective methods for direct observation of laser-induced morphologies are missing. To address this need, this thesis work explores *in situ* methods for direct observation of femtosecond laser-modified zones.

The first one consists in using a quantitative phase-contrast microscopy method: digital holographic microscopy. We propose a feedforward manufacturing method, which uses phase data acquired from the microscope, to feed a semi-analytical model, i.e., a ‘digital twin’. We demonstrate the resilience of this method to quill effects (directionality), and its increased inscription resolution.

The second method consists in using full-field multiphoton microscopy. The interaction between the processing laser, with a decreased energy, and already-written structures, induces harmonics generation. Their signals and emission patterns vary depending on the morphology of the structures. Three different interaction regimes are identified in fused silica with third-harmonic generation, associated respectively with nanopores, nanogratings, and microexplosions. The former shows a correlation between the signal and wet etching rate. This full-field method allows to identify the shape of the exposed modifications, and to study them by fast focal-plane tomography, highlighting their time-resolved formation.

Finally, we present scientific demonstrations and potential applications for these methods. We show that we can inscribe large-scale refractive structures. We then show the validity of the incubation law, and highlight the stochastic nature of the inscription process, using the high contrast allowed by third-harmonic generation, and with a survival analysis. We also show the ability of this method to detect otherwise optically undetectable laser-induced modifications, buried close to a surface. Finally, full-field third-harmonic generation microscopy allows to determine single-shot the nature of some modifications, particularly in the case of ultraviolet femtosecond laser processing.

Résumé

Au cours des décennies passées, les progrès accomplis dans la génération d'impulsions laser plus courtes qu'une picoseconde (10^{-12} s) nous a permis d'atteindre des intensités optiques excédant 1×10^{15} W cm⁻². Cette formidable puissance a provoqué une abondance d'applications scientifiques et industrielles. Parmi elles, le traitement de matériaux, et en particulier, le traitement dans le volume de matériaux transparents, motivent le travail ici présenté. Les lasers femtoseconde génèrent une riche taxonomie de modifications, qui peuvent prendre diverses formes, y compris de la densification localisée, des nanoréseaux autoorganisés, de la cristallisation localisée, ou de l'amorphisation, qui varient dans l'espace de paramètres d'exposition, et d'un matériau à l'autre.

À ce jour, des méthodes d'observation directe des structures induites par laser manquent. Pour pallier ce besoin, ce travail de doctorat explore des méthodes d'observation directes *in situ* des zones affectées par laser femtoseconde.

La première consiste à employer une méthode de microscopie à contraste de phase quantifiée, l'holographie numérique. Une méthode de fabrication par mise en forme d'entrée est proposée, celle-ci utilisant les données du microscope pour optimiser un modèle heuristique semi-analytique. Nous démontrons la résilience de cette méthode d'impression aux effets de plume (directionnalité) et l'augmentation de la résolution d'impression.

La deuxième méthode consiste à utiliser la microscopie multi-photonique en champ plein. L'interaction entre le laser de fabrication, avec une énergie réduite, et la morphologie optiquement hétérogène des modifications provoque la génération d'harmoniques, dont les signaux et les directions d'émission dépendent de ces mêmes structures. Trois différentes régions d'interaction dans la silice fondue sont identifiables par microscopie de troisième harmonique, associées respectivement à des nanopores, des nanoréseaux, et des micro-explosions. La première montre une corrélation entre signal émis avec le taux de gravure chimique. Le champ plein permet de conjecturer sur la forme des modifications, et de les étudier par tomographie par plan focal rapide, mettant en évidence leur formation résolue en temps.

Nous présentons finalement des démonstrations scientifiques et de potentielles applications de ces méthodes. Nous montrons notamment l'inscription de structures réfractives à grande échelle. Nous mettons de même en évidence la loi d'incubation, ainsi que la nature stochastique de l'interaction grâce au fort contraste de la microscopie de troisième harmonique, via une étude de survie. Nous démontrons de même la capacité de détection de structures inscrites sous la surface avec cette méthode, qui sont autrement indétectables. Finalement, la microscopie de troisième harmonique en champ plein permet de déterminer en un coup la nature des modifications, particulièrement dans le cas de l'usinage par laser femtoseconde ultraviolet.

Contents

Remerciements / acknowledgements

Abstract / résumé iii

I	Introduction	1
I.1	General introduction	2
I.2	Towards controlling laser-induced modifications	3
I.2.1	On feedback, and the case of laser-based processes	3
I.2.2	Non-ablative dielectrics processing: a practical summary	5
I.2.3	A processing platform: canvas for femtosecond laser processing	7
I.3	A taxonomy of laser-induced defects	9
I.3.1	Molecular defects in fused silica	9
I.3.2	Morphological structures	11
I.3.3	Asymmetric macro-structures	14
I.4	A taxonomy of observables	17
I.5	Thesis outline	21
II	Monitoring and feedforward control based on phase contrast imaging combined with a digital twin	23
II.1	Methods and setup	25
II.1.1	Principles of digital twin-based processing	25
II.1.2	Processing platform	27
II.1.3	Phase-contrast imaging system using an on-axis digital holographic microscope (DHM)	29
II.2	Digital twin	29
II.2.1	Analytical modelling	29
II.2.2	Discrete pattern description	31
II.2.3	Model optimisation	32
II.2.4	Determining the modulation signal	32
II.3	Experimental demonstration	33
II.3.1	Effect of pattern rotation	33
II.3.2	Inscription of arbitrary patterns	35
II.3.3	Towards sub-diffraction resolution patterns	36

Contents

III Full-field nonlinear microscopy as a means for monitoring laser-induced modifications.	39
III.1 Experimental method	41
III.1.1 Processing platform	41
III.1.2 Imaging optics	43
III.1.3 Sensing and data acquisition	44
III.2 Full-field THG detection of laser-affected zones	45
III.2.1 Scanning and full-field methods of THG imaging	45
III.2.2 Third harmonic response of modifications to different probing polarisation states	48
III.2.3 THG and wet etching selectivity	50
III.2.4 Tomography of laser-induced defects, and their evolution under irradiation	53
III.3 Second-harmonic generation microscopy and multi-photon fluorescence microscopy	55
IV Demonstrations and applications	59
IV.1 Inscription of phase maps	60
IV.2 Observation of laser-induced modifications in complex environments with THG: case studies	62
IV.2.1 Case study I: continuity of inscribed lines in bulk fused silica	62
IV.2.2 Case study II: femtosecond UV processing: waveguides and pores	65
IV.2.3 Case study III: sub-surface exposure of multilayers	68
IV.3 Modification threshold frontier modelling using THG experiments	71
IV.3.1 Incubation law	71
IV.3.2 Reliability analysis	73
IV.3.3 Comparison between different types of transparent materials	75
V Conclusion	79
V.1 Summary of observations	80
V.2 Discussion and outlooks	81
A Appendices	85
A.1 Interactions of ultrafast laser pulses in dielectric media	85
A.1.1 On ultrashort laser pulses	85
A.1.2 Nonlinear propagation of pulses in matter	87
A.1.3 Breakdown mechanisms	89
A.2 Custom wide-field THG objective	92
Bibliography	95
Curriculum vitae	107

I Introduction

I.1 General introduction

Over the last decades, the progress made in the generation of laser pulses shorter than a picosecond (10^{-12} s) has allowed us to reach extreme optical power intensities exceeding 10^{15} W cm $^{-2}$. This tremendous power has triggered an abundance of original scientific and industrial applications. Chief amongst them is material processing, and in particular, in-volume processing of transparent materials, which motivates the present work.

In transparent substrates, short intense pulses trigger nonlinear absorption phenomena, [1–4] such as ‘multiphoton’ absorption, [5] during which the laser radiation is locally absorbed, while it would have been transmitted if it were less intense. Under such conditions, tightly focused ultrashort laser pulses locally transform the transparent medium through which it travels.

In the case of fused silica, ultrafast laser-induced modifications take several forms, depending on processing parameters. These include a localised increase of density and hence refractive index, useful for inscribing direct-write waveguides. [6] Self-organised nanostructures may also appear. [7] These find multiple uses, such as a local increase of etching selectivity [8] – allowing versatile 3D manufacturing of glass components, [9] the design of novel photonics components, [10] and means for storing optical information. [11] These are just two examples amongst many more.

Nonlinear absorption phenomena triggered by femtosecond lasers offer a rich taxonomy of material modifications, that can take diverse forms, including localised crystallisation, [12] or amorphisation, [13] and that will vary from one material to another.

The complex nature of the laser-matter interaction between material and ultrafast laser pulses is at the origin of such diversity. Several modification regimes coexist in the laser-parameter space for a single material, with often unclearly defined boundaries. [14] Extensive tuning of the process parameters for a given substrate is thereby required, until a desired stable laser-exposure regime is identified. Such operation is performed through cumbersome and time-consuming postmortem analysis. The inscription process may also lead to random instabilities while scanning the laser over a surface, or in the volume. [15–17] Finally, the complexity of processing platforms, including the laser source itself, and noise accumulated for each active element, increase the risk of perturbation.

Such issues may be alleviated by implementing control theory, which assumes the existence of methods to monitor the process.

In laser manufacturing in general, *in situ* process monitoring is rarely performed. Only a few examples thereof [18, 19] have been reported in the literature. This arises from intrinsic technical difficulties, as the laser-induced modifications are experimentally difficult to probe optically. In the case of non-ablative femtosecond laser processing in

I.2 Towards controlling laser-induced modifications

the bulk of transparent materials, process monitoring becomes even more challenging to perform, due to the small size of the laser-affected zones, at most a few μm^3 in volume, and often with low optical contrast compared to pristine material.

This thesis work aims at *investigating in situ monitoring methods adapted to femtosecond laser processing of transparent substrates*.

Specifically, we study: (1) an inscription method based on a heuristic model, with *in situ* observation through digital holographic microscopy, (2) nonlinear imaging methods of laser-affected areas, probed with the processing laser itself, and (3) the potential applications and demonstrations of these two methods.

This chapter summarises our current knowledge of the laser process discussed in this work and introduces some foundational background around the topic of process monitoring. Appendix A.1 provides further theoretical considerations.

I.2 Towards controlling laser-induced modifications

I.2.1 On feedback, and the case of laser-based processes

Let us address the main *raison d'être* of this thesis work. Feedback is the condition of a system, in which at least one input and one output are linked together. For an open-loop system, the output directly depends on the input – but not the other way around.

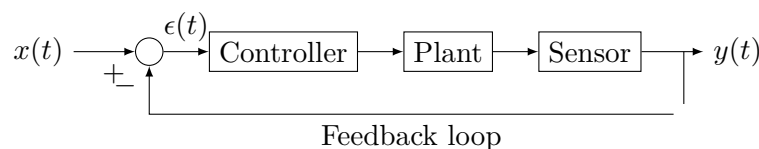


Figure I.1: Representation of an active feedback control system in its simplest form for a generic controller of a ‘plant’ (that defines the entity to be controlled). The user (or a parent process) inputs a set point $\bar{y}(t)$ for the plant. The sensor outputs a process value $y(t)$. The controller takes the error value $\epsilon(t) = \bar{y}(t) - y(t)$ and drives the system according to a control function. In the case of laser process control, the plant would be the material to be processed.

The development of electronics and computers brought control theory to nearly every aspect of science and engineering. It has allowed several technological advancements by introducing arbitrary and more sophisticated controller models by numerically sampling observable information from the plant and processing it numerically before converting it back to the analogical domain. In its simplest form, a feedback system involves two parts: a sensor – which in its general understanding collects information from the plant, that can be one or multi-dimensional (e.g., a temperature information, an image, a vector,

etc.); and a controller, which is able to drive the system depending on the error between the set point $\bar{y}(t)$ and the process value $y(t)$, $\epsilon(t) = \bar{y}(t) - y(t)$, so that the error $\epsilon(t)$ is minimised. Figure I.1 summarises such behaviour.

To work towards implementing a feedback loop, the first step is to identify an observable, i.e., ‘*what to sense*’. This observable should define a pertinent metric, with respect to the process. Let us consider as an example a welding process. One could intuitively think of using the local material temperature as a metric, which implies that there exists a model that relates temperature to a desired welding quality. The model may however require more than just one metric. For instance, in the same example, one could be interested in controlling the width of the weld or avoid the formation of cracks.

This simple example illustrates some of the key issues to address before being able to implement a feedback loop. One is the identification of suitable metrics (that ‘monitor’ the process), two is the existence of a relationship between the metrics and the process quality parameters, and three is the design of a suitable controller to efficiently achieve a process performance.

The difficulty in laser processes is that there is a limited access to the process zone, as it is often small. This becomes even more difficult when dealing with nonlinear processes occurring *inside* the material. Furthermore, a consequence to the small sizes of the processed zones is the fast dynamics required to counteract with deviations from a desired outcome.

Let us now explore in the literature an example of monitoring and controlling in laser-based processes, in general.

Let us consider this time the case of glass welding using femtosecond laser pulses. This topic has been a developing subject of research, with strong interest for integrating in production lines, notably in the consumer electronics, laser components, healthcare, and automotive industries. Its development is however hindered by moving seam joint location, varying weld penetration depth and profile, and the risk of cracks. Controlling the process is therefore critical, and studies aiming at implementing control have been carried. Fischer *et al.* [20] investigated the use of an optical microphone-transducer to detect whether the weld is faulty or not, as the presence of strong peaks in the acoustic signal has been linked to faulty weld. Hecker *et al.* [21] used transverse plasma emission caused by the welding process itself, to identify defects in glass welding. In the case of power modulated laser welding, they report that plasma emission is influenced by gap bridging, irregularities, and defects. A single photodiode can be used for this method.

These examples towards *in situ* sensing in laser-based manufacturing offer insightful guidance towards achieving the goal of this thesis – implementing monitoring and controlling in the context of *non-ablative dielectrics processing*.

Before diving further into the topic, let us first briefly introduce non-ablative femtosecond laser processing of transparent substrates.

I.2.2 Non-ablative dielectrics processing: a practical summary

As an introduction to the case study of this thesis, we picture non-ablative dielectrics processing as a method to locally tailor the properties of a material in three dimensions. A laser beam travels unaffected through a piece of transparent material, but can trigger modifications in the material, if it is intense enough. In this thesis, this intensity is only reached at the focus of the beam. A variety of laser-induced modifications can be generated, depending on process parameters, and the type of exposed dielectric. These modifications bear specific functional properties, some of which being of interest for manufacturing.

In this subsection, we will present the working principle, and some developed applications of this processing method, illustrated by Figure I.2. We give a more formal introduction to ultrashort pulses, their propagation in dielectrics, and mechanisms leading to modifications in Appendix A.1.

Operating principle. Let us picture a typical laser processing platform, with an example pictured in Figure I.3. A femtosecond laser delivers a train of pulses. User- or computer-operated equipment tunes their power and repetition rate, e.g., using a power modulator and a pulse-picker. The polarisation state of the beam is typically controlled as well. Specific optics induce strong intensity at the focal spot, so that the modification can occur there. A 3D-motion controller performs volume processing, either by moving the sample or by scanning the beam over the specimen.¹ We will address this equipment in detail in §I.2.3.

Laser-induced modifications show several properties, which can be used for various applications. Let us discuss a selection of those.

Chemical etching. Some laser-induced modifications, increase the selectivity of some glass to wet etching, most notably in hydrofluoric acid (HF), [24] potassium hydroxide (KOH), [25, 26] and caustic soda (NaOH). [27] This principle allows versatile 3D processing of glass through etching of the exposed volume. This method shows a feature resolution

¹Scanners, e.g., motorised mirrors, can also be used for processing, thereby processing a static sample. This method limits the processing area to the optical field of view (FOV) of the processing optics. Larger field of view optics have, by definition, less focusing power.

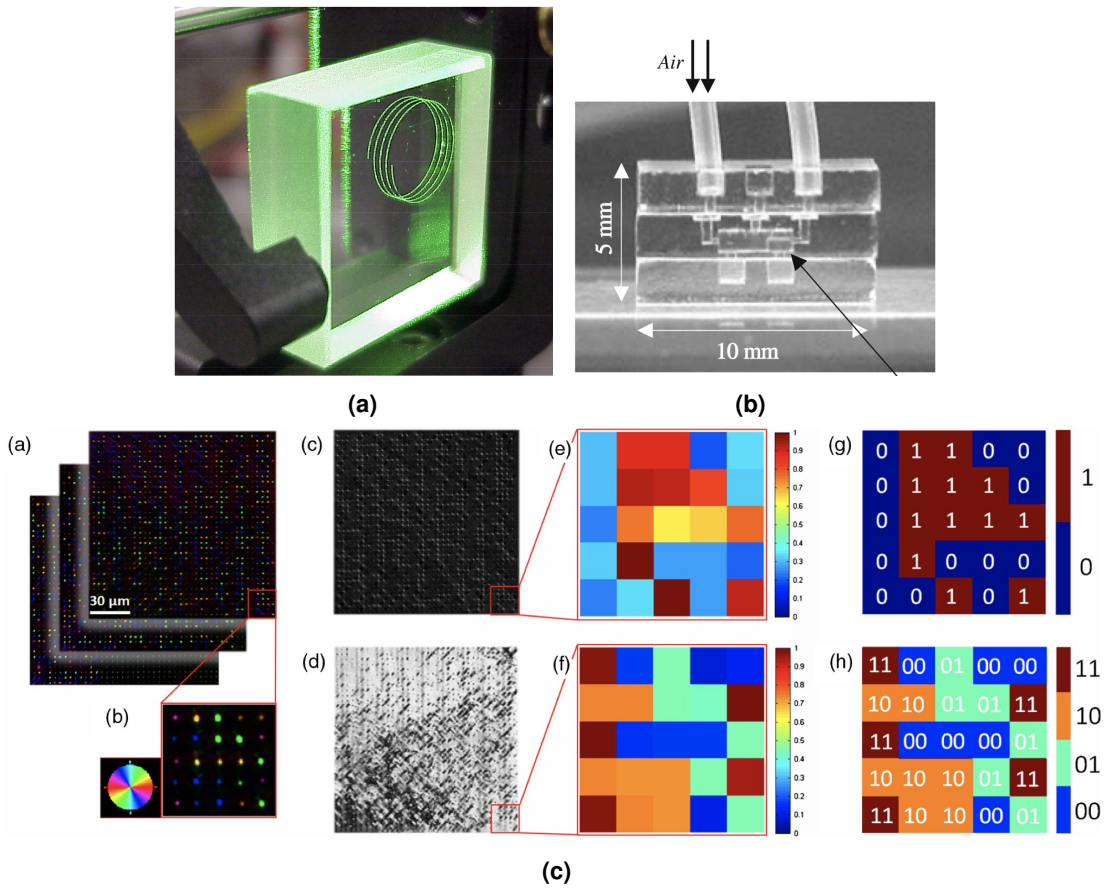


Figure I.2: Selection of applications allowed by non-ablative femtosecond laser processing of fused silica, a representative example of dielectrics. (a) is a photograph of a green light-coupled spiralled waveguide (reprinted from Bado *et al.*). [22] (b) is a photograph of a 3D machined piece (reprinted from Sugioka *et al.*). [23] (c) is a collection of images illustrating 5D optical data storage inscription and readout (reprinted from Zhang *et al.*). [11]

down to approximately 1 μm. [28] Given the high biocompatibility of fused silica, such a feature is ideal for fabricating lab-on-chip experiments, [23, 29] some medical devices, [30] as well as flexures mechanisms, [31] or sensors. [32]

Waveguiding. Some types of modifications have the ability to guide light, through local refractive index increase. [4, 33, 34] This allows direct-write optical circuits, beam delivery onto and collection from a precise area. This method has been integrated with selective etching to create fully direct-write lab-on-chip experiments. [29] Optical circuits can perform complex functions, as sought after in quantum optics experiments. [35] In doped media, direct-write inscription can also create laser-amplifying waveguides. [36]

Data storage. Birefringent modifications in fused silica allow for five-dimensional data storage (i.e., X, Y, Z, polarisation direction, retardance), that can withstand natural degradation for a time longer than the age of the universe – i.e., 13.8×10^9 years. [11] Naturally, this is of significant interest in the prospect of replacing highly consuming data centres by highly stable discs, for archiving infrequently accessed data, with significant prospects in energy savings.

As we have seen, non-ablative processing of dielectrics stems from a very simple principle: exposing matter to intense and ultrashort non-ionising radiation and branches out into a variety of applications. To conclude this section, let us discuss the basic building blocks necessary to get a simple processing platform ready.

I.2.3 A processing platform: canvas for femtosecond laser processing

Laser processing platforms, especially those used for advanced research, may expand to intricate setups, depending on the application. However, very few elements are fundamentally necessary to get a functioning system. Let us here address these building blocks, and discuss some methods to implement them, as well as common additional equipment.

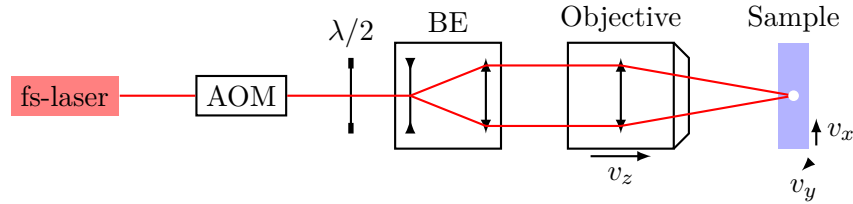


Figure I.3: Schematic of the main components of typical femtosecond laser processing platform. A laser source outputs a linearly polarised beam. An acousto-optic modulator (AOM) controls the beam power. A half-wave plate rotates the linear polarisation state ($\lambda/2$). To fit the entrance pupil diameter of the objective lens, a fitting beam expander (BE) magnifies the beam. The objective lens then focuses the beam in the volume of the sample. To achieve three-dimensional processing, the sample is set onto a two-dimensional (x, y) platform, while a translating stage (z) carries the objective lens, to shift the focal plane, and therefore, the depth of the modified area.

Laser source. The source must achieve the required optical intensities needed to obtain the sought-after modifications, with $I_{\text{th}} \gtrsim 5 \times 10^{12} \text{ W cm}^{-2}$ for fused silica.² Assuming a typical diffraction-limited beam diameter at focus of $2.5 \mu\text{m}$, and a pulse duration $\tau_p = 200 \text{ fs}$, the typical minimum energy threshold would be $E_{\text{th}} \simeq 50 \text{ nJ}$. Furthermore,

²Optical pulse intensity is defined as $I = E_p/(\tau_p A_w)$, with E_p the pulse energy, τ_p the pulse duration, and A_w the area at focus. For an ideal Gaussian beam ($M^2 = 1$), we write $I = E_p/(\pi w_0^2)$, with w_0 being the beam waist at $1/e^2$.

repetition rates over 1 MHz typically induce thermal accumulation effects.³ Successive pulses should overlap with each other to create continuous modifications, thereby a too low repetition rate, or a too high scanning speed, is detrimental to the process itself. The linear pulse density writes $\delta = \nu/v$.⁴ In this thesis, we typically use a repetition rate of $\nu = 100$ kHz. This rate, with a scanning speed $v \in [0.1 \text{ to } 10 \text{ mm s}^{-1}]$, attainable with conventional translation stages, reaches pulse densities of $\delta \in [10 \text{ to } 1000 \mu\text{m}^{-1}]$. Conventional industrial Yb-based femtosecond amplifiers typically operate with repetition rates $\nu < 1$ MHz, $E_p < 1 \mu\text{J}$ and $\tau_p \in [150 \text{ to } 500 \text{ fs}]$.⁵ These lasers operate around $\lambda = 1030 \text{ nm}$ – and harmonics can be efficiently generated, notably at $\lambda_{3\omega} = 343 \mu\text{m}$.⁶

Power and polarisation control. An economical method for controlling the laser power consists in using a motorised half-wave plate with a polariser. This method is however slow, with typically a few Hz. A faster method consists in using an acousto-optic modulator (AOM), often included in laser outputs, which allows amplitude modulation with bandwidths well above 100 kHz. The polarisation state is usually kept linear. Wet-etching rate is often polarisation-dependant on the scanning orientation. The most common economic method consists in using a single motorised half-wave plate to orientate it. Electro-optic modulators (Pockels cells) allow fast tuning of the polarisation state, including circular and elliptical states,⁷ with bandwidths > 1 MHz. [37, 38]

Optical delivery. The optics used to focus the beam into the sample are of uppermost importance, given the inverse square dependency on the beam size of the peak power. The objective lens' specifications must therefore attain a small enough beam size considering peak power, and highest transmittance. Given the relatively short spectral linewidth of most common femtosecond amplifiers, special focusing objective lenses can be used, with optimised anti-reflection coatings to enhance transmittance.⁸ Objective lenses, able to achieve small spot sizes, usually have a large entrance pupil diameter, larger than most

³Thermal accumulation is the gradual increase in temperature near the laser-affected zone, by the consecutive heating induced by several pulses. This effect becomes critical in such processes when the material locally becomes partly liquid – modifications there take different morphologies, such as micro-bubbles of various sizes. These effects are not considered in this thesis. Note that the threshold repetition rate to obtain such effects can be much lower for other types of materials, that are here not considered.

⁴Using this quantity for comparison is valid only if beam sizes between experiments are similar. Radiant exposure (unit J mm^{-2}) is otherwise a more robust quantity. Linear pulse density however allows to easily compare exposure conditions between fixed (point) and scanning (line or curve) exposures, as further seen in this thesis.

⁵Yb:fibre laser amplifiers are typically used, but often have a spectral linewidth limiting their pulse duration to $\tau_p > 250$ fs. Regenerative amplifiers can reach shorter pulses $\tau_p > 150$ fs, but are usually limited to relatively low repetition rates $\nu < 100$ kHz, and must be water-cooled.

⁶The exact wavelengths vary depending on the amplifying medium, and optical design of the laser oscillator and amplifiers.

⁷This requires additional waveplates, namely quarter-wave plates – see Ref. [37].

⁸Poor transmittance may also cause damage to the focusing optics.

laser beam diameter output. To match the former, a beam expander is therefore often needed. Typically, high numerical aperture $NA > 0.2$ objectives are desired, although this is usually at the expense of the working distance, and the field of view.

Adaptive optics. Additional equipment can be added to the processing platform. A notorious example is adaptive optics, such as deformable mirrors and spatial light modulators (SLM). These elements can be used to reduce aberrations caused by certain high refractive index materials, like diamond, [39] or implement holographic writing. [40] For this case study however, we use the most run-of-the-mill platform as a building block, from which we append monitoring and controlling methods.

Section summary. In this section, we have introduced basic principle of control, that we narrowed down to the need of such systems for our case study: femtosecond laser processing of dielectrics. We introduced the manufacturing process itself, with its applications, as well as the canvas on which this doctoral work has been carried. Now that the stage has been set, let us address in more details what this process physically consists in, so that we can identify possible control mechanisms.

I.3 A taxonomy of laser-induced defects

Laser-induced modifications can take several forms, and appear concomitantly at different scales (e.g., molecular defects inside mesoscopic structures, voids). As these modifications are the key elements of the functional properties we wish to control, we lay out here a taxonomy of known modifications for fused silica, the material of choice for this thesis work. We will first address the smaller scale type of modifications first – molecular ones, then scale up to morphological ones, and some other aspects.

I.3.1 Molecular defects in fused silica

Tightly focused femtosecond lasers trigger nonlinear absorption, which, under sufficient optical intensity, triggers ionisation. Appendix A.1.3 discusses the physical phenomena leading to ionisation. As laser-induced free electrons thermalise, they may cause disruptions in the molecular lattice in the exposed area. Here, we address examples of known bulk laser-induced molecular defects in fused silica.

After photoionisation, free carriers self-trap in SiO_2 in approximately 300 fs. These excitons take the form of an electron coupled to an oxidised atom (here, Si^+), separated by a distance about the interatomic size. The induced excitons then decay exponentially

with estimated lifetimes of (34 ± 8) and (338 ± 67) ps at room temperature. [41] It appears that electrons travel a small of distance before trapping. [42] Their creation has been shown to be significantly caused by avalanche ionisation. [41]

Modifications may evolve into non-bridging oxygen hole centres (NBOHCs), i.e., broken Si–O bonds, either from radiolysis of hydroxyl (OH) groups⁹, or of the glass network itself. These defects have a wide absorption band at $4.80(51)$ eV,¹⁰ and a thin asymmetric one at 1.97 eV. [43]

Laser exposure can also release oxygen atoms from the glass lattice. The normally quadravalent silicon atoms therefore may lose either one or two oxygen atoms, becoming oxygen-deprived centres, abbreviated ODC(I) and (II), respectively. In the first case, this takes the form of a relaxed vacancy between two Si atoms, that can be annealed for UV transmission, [44] and in the second, it takes the shape of a divalent Si atom.

Irradiated fused silica commonly shows an absorption band at 5.8 eV, identified as ‘ E'_γ -centres’ thanks to correlation with electron paramagnetic resonance (EPR). These centres exist at both surface and bulk and take the form of unrelaxed oxygen vacancies. [43]

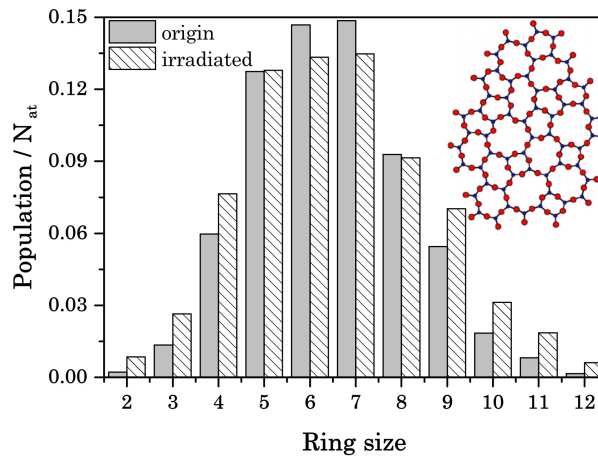


Figure I.4: Modelled, normalised distribution of sizes of SiO₂ rings in fused silica, for pristine and femtosecond laser-exposed fused silica. The inset shows a coloured representation of the atomic arrangement of SiO₂ rings, as first theorised by Zachariasen. [45] Reprinted from Shcheblanov *et al.* [46]

Fused silica is a glass: SiO₂ molecules arrange themselves in rings of statistically distributed sizes. [47, 48] Femtosecond-laser irradiation often changes this arrangement, with increased density of four- and three-element rings. These structural changes can be observed with Raman spectroscopy, with peaks appearing at 490 and 605 cm^{-1} , for four- and three- element rings, respectively. [46, 49]

⁹Hydroxyl groups are common impurities in fused silica. Different ‘OH-grade’ types of glass exist.

¹⁰The value under parenthesis represents the full width at half maximum of the band – here, 0.51 eV.

I.3 A taxonomy of laser-induced defects

Colour centre	Absorption bands / eV	PL bands / eV	Stokes shift / cm^{-1}
ODC(I)	7.6	4.4 and 2.7	
ODC(II)	3.15, 5.05 and 6.9	4.4 and 2.7	
NBOHC	1.97 and 4.8	1.9	
E'_γ centre	5.78	none	
STE†	5.2	not reported	
4-Si-O ring			490
3-Si-O ring			605

Table I.1: Molecular defects of fused silica created by laser exposure, with their associated absorption, photoluminescence (PL) bands, and Stokes shift. Adapted from Skuja. [43]. †: STEs decay in < 1 ns.

We summarise the optical activity of the laser-induceable defects presented in this section in Table I.1. They are often an undesired outcome of extreme laser exposure, typically in fibres. Nonetheless, they form the backbone of larger scale modifications that are useful to our process.

I.3.2 Morphological structures

With increased exposure, ultrafast laser-induced modifications typically expand beyond the atomic scale into the μm -scale.

Homogeneous modifications (alias type I)

Davis *et al.* [6] first identified that exposing fused silica with short pulses ($\tau_p < 150$ fs) induced homogeneous refractive index increase, in the order of $\Delta n \simeq 1 \times 10^{-3}$. These variations were thought to arise from the cumulative effects of molecular defects, [6] but more likely emerge from local densification. [50] This can take the form of increased four- and three- element ring structures. NBOHCs have also been identified in this regime, causing photoluminescence, and increased absorption in both visible and UV spectra. [49] This type of modification has been exploited to write free-form waveguides in glass, ultimately for inscribing direct-write optical circuits in glass substrates. [35, 51]

Nanogratings (alias type II)

Strongly anisotropic laser-induced structures, as illustrated after etching in Figure I.5, appear in a variety of materials, [53, 54] which have first been identified by Shimotsuma *et al.* [7] as periodic planar structures. Their orientation is perpendicular to the electric field of the beam, [52] and the laser pulse envelope shapes their period and contrast. [18] The strong birefringence, capable of inducing negative phase shift, arises from the composite

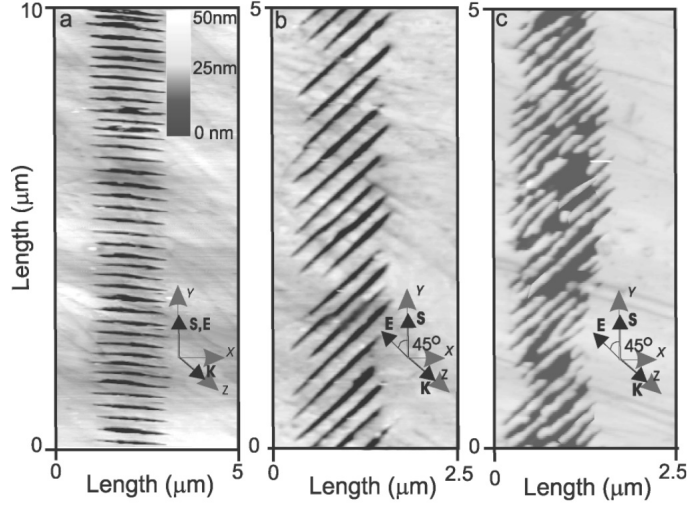


Figure I.5: Top-view section of a laser-affected zone: atomic force microscope (AFM) topographic image of wet-etched nanogratings, with (a) polarisation parallel to scanning speed vector (reported as \mathbf{E} and \mathbf{S} respectively), (b, c) at 45° . (a, b) were inscribed with pulses of wavelength $\lambda = 800$ nm and pulse energy $E_p = 300$ nJ. (c) was inscribed with $\lambda = 400$ nm, $E_p = 150$ nJ. The self-arrangement of gratings perpendicular to laser polarisation, and increased etchability (here, to HF) is revealed. Reprinted from Bhardwaj *et al.* [52]

structure of these modifications, see Figures I.5 and I.6.¹¹ They appear at a wide range of processing parameters, typically for pulses of duration $\tau_p \in 70$ to 200 fs, and above a low pulse energy threshold $E_p > 70$ nJ. At longer pulses, they appear for pulse energies $E_p < 300$ nJ

The physical mechanisms leading to the formation of self-organised nanogratings have been debated since they have been first observed. Shimotsuma *et al.* [7] suggested that these periodic structures arise from the interference between the incident light and the Langmuir wave - causing periodic modulation of the electron concentration in the plasma. Bhardwaj *et al.* [52, 56] suggested that nanoplasma spheres arise from previously written, laser-induced hotspots. More recently, Rudenko *et al.* [57] suggested two simultaneous mechanisms: interference between the incident light with locally scattered waves (inducing λ -scale structures), and multiple coherent scattering ($\lambda/2$ -scale structures). This model

¹¹Regular anisotropy at the molecular level induce the birefringent in crystals. However, structures whose scales lay between the molecular, and the wavelength of observation, induce *form* birefringence. Nanogratings fit this definition. Let us consider a regular assembly of planes of refractive index immersed in a material, of refractive indices of n_1 and n_2 , respectively. We write the fractions of total volumes of the former $f_1 = t_1/(t_1 + t_2)$, and of the latter $f_2 = 1 - f_1$, with t_1 the thickness of the thin plates and t_2 the thickness of the space in-between. See Figure I.6 for a schematic. We can write: [55]

$$n_e^2 - n_o^2 = -\frac{f_1 f_2 (n_1^2 - n_2^2)^2}{(1 + f_1)n_2^2 + f_2 n_1^2} \quad (\text{I.1})$$

with n_e and n_o the extraordinary and the ordinary axes indices, respectively. Note that this equation implies that such an assembly behaves as a negative uniaxial crystal.

has recently been refined with additional hydrodynamics considerations. The analogous effect that appears on surfaces (commonly designated as ‘laser-induced periodic surface structures’, or LIPSS), that has been observed and studied for several decades, may share a common electromagnetic origin, although the growth mechanisms are physically different. [58, 59]

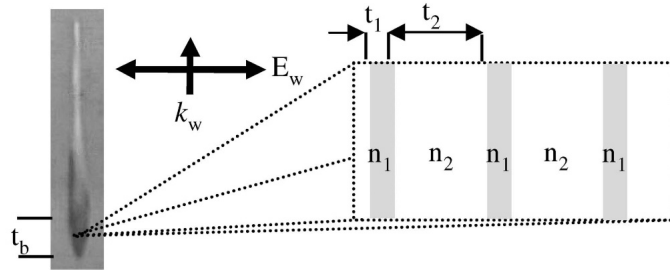


Figure I.6: Schematic of laser-induced nanogratings in glass. E_w and k_w represent the electric field and the wave vector, respectively, of the processing beam. Left: cross-section of a laser-affected zones, with the laser coming from the bottom; right: schematic representation of two media of refractive index n_1 and n_2 , inducing form birefringence. Reprinted from Bricchi *et al.* [60].

Nanogratings have been used in several applications, from optical elements to micromechanical devices. Their stark form birefringence, has made them interesting for inscription of polarisation converters, especially given their wide band of operation, as broad as 200 to 2100 nm in fused silica, with post-annealing. [44] By tuning both the birefringence angle and retardance, five-dimensional data storage has been shown, achieving record data intensity. [61] Cai, Libertun and Piestun [62] inscribed holograms in glass using nanogratings. They have been of high interest for developing direct-write phase plates, notably for spin-orbit optics. [63] As shown in Figure I.5, nanogratings enhance wet-etching selectivity along their orientation. This element is the backbone of 3D micromachining of glass using femtosecond lasers. [9, 24]

Nanopores (alias type X)

A more recent discovery was the presence of a regime consisting of smaller-scale pores, stretched in one direction, which exhibit birefringence albeit having high transmittivity. [38] Figure I.7 provides an illustration. They occur in silica glass at specific processing conditions: exposure with few pulses $n < 100$ pulses, a specific range of pulse duration $\tau_p \in [250 \text{ to } 400 \text{ fs}]$, and most notably with low numerical aperture $NA < 0.2$.

Further reviews showed that they appear in several grades of fused silica. [64] As suggested previously, a recent theoretical development suggested that these pores are specific types of nanovoid structures and are precursors to nanogratings. [59]

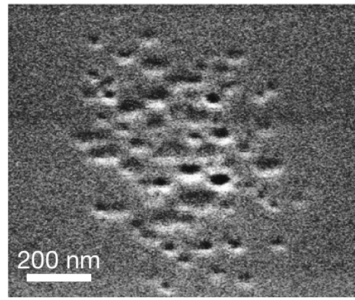


Figure I.7: Cross-section scanning electron microscope image of a laser-affected zone consisting of nanopores. Reprinted from Sakakura *et al.* [38]

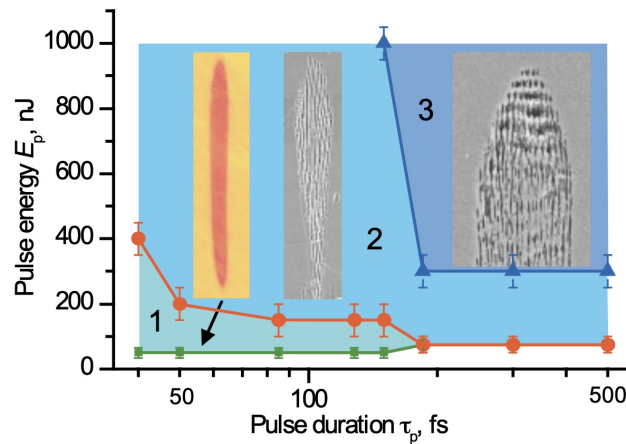


Figure I.8: Morphologies of modifications as a function of pulse duration and energy, obtained with a Ti:Al₂O₃ laser ($\lambda = 800$ nm), and a numerical aperture of NA = 0.65. Reprinted from Taylor *et al.*, [56] itself derived from Hnatovsky *et al.* [14]

Process maps

These types of structures discussed above appear after exposure with femtosecond pulses at different processing parameters, and for specific materials. Several studies approached the limits in processing parameters separating these types of modifications in processing maps, as shown in Figure I.8.

I.3.3 Asymmetric macro-structures

Laser beams are usually represented as perfectly symmetric along the optical axis, as well as in time in the case of pulsed lasers. However, as ultrafast dynamics occur at similar timescales to the pulse duration, deviations from this approximation yield perturbed outcomes. Appendix A.1.1 provides a discussion about those asymmetries in ultrafast pulses. It is indeed usually desirable to have the most circular beam profile, unchirped

pulses, to alleviate the possible symmetrical issues caused by pulse asymmetry. Such effects may however be difficult to compensate in processing systems or be even sought after in specific cases (i.e., non-reciprocal writing).

Quill-writing

A notable, usually accidental feature of femtosecond lasers is pulse-front tilt, as described in Appendix A.1.2. [65] This is typically caused by misalignment of the pulse compressor at the output of ultrafast lasers. Using standard autocorrelator measurements, this appears as a longer-than-expected pulse, as this method cannot directly resolve pulse-front tilt. More advanced methods like frequency resolved optical gating (FROG) can measure this effect. [66] Beam ellipticity may also contribute to such effects, although they are easier to measure and to compensate optically.

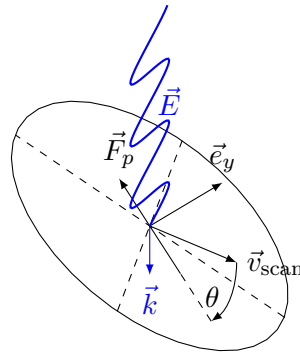


Figure I.9: Representation of the effects of pulse-front tilt and ellipticity when performing scanning exposure. The beam comes at an arbitrary linear polarisation parallel to the electric field \vec{E} , at a wavevector $\vec{k} \perp \vec{E}$. The beam travels in a sample at a speed \vec{v}_{scan} . The pulse-front tilt can be represented as an elevation angle θ , also relative to \vec{v}_{scan} . The pulse-front tilt induces, when exposing a fluid of free electrons, an upwards ponderomotive force \vec{F}_p .

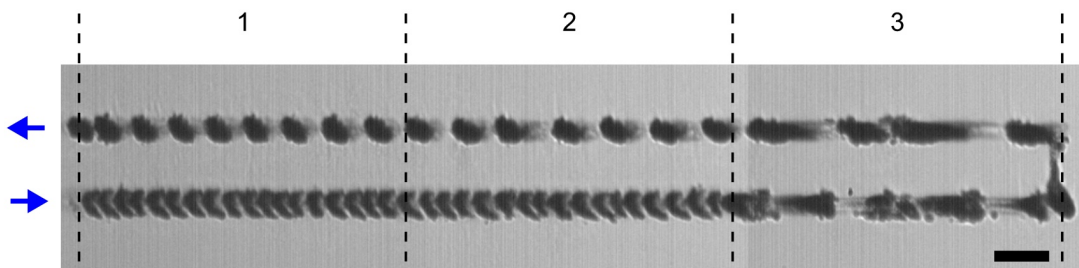


Figure I.10: Bright field microscope images of ablated lines written on a fused silica surface, using a simultaneous spatio-temporal focused beam (SSTF), with strong pulse-front tilt. Blue arrows on the left indicate the writing direction, and polarisation is parallel to the scanning direction. Numbers 1, 2, and 3 indicate scanning speed: 5, 10 and 50 $\mu\text{m s}^{-1}$, respectively. Scale bar: 50 μm -long. Reprinted from Vitek *et al.* [67]

Figure I.9 shows a representation of these effects. In the context of a scanning exposure, a dependence of the scanning direction on the structure of the modified zones, caused by pulse-front tilt, has been shown. This effect is dubbed ‘quill-writing’. [68] Notably, under certain circumstances, this effect can be so strong that different regimes occur depending on the writing direction and tilt level. [69] Also, in the context of simultaneous spatio-temporal focusing (SSTF), pulse-front tilt emerges [70]¹², for which quill-writing is also observed, [67] and pictured in Figure I.10. The influence of pulse-front tilt has been explained by the influence of the ponderomotive force over free charges. This force drives these charges out of the zone of high intensity down its gradient, that is here out of the optical axis.

Effect of aberrations

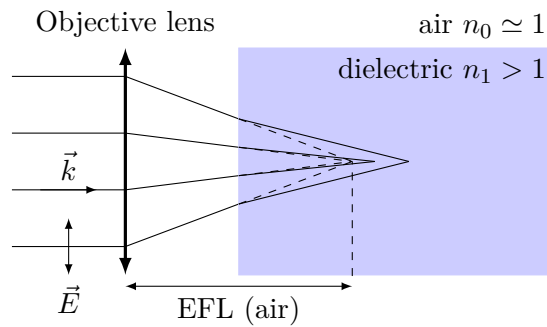


Figure I.11: Ray representation of aberrations caused by the air-material interface, when tightly focusing in the bulk. The beam comes at a polarisation \vec{E} , with the wavevector \vec{k} normal to the air-dielectric interface. The beam is focused by an ideal, dry objective lens, of effective focal length EFL. Light is subject to refraction as it enters the material and, as it is tightly focused, the paraxial approximation becomes unreliable. Therefore, the focus length extends depending on the distance of a single ray to the optical axis. Note that if the beam comes towards the interface at an angle, additional aberrations are induced, in the form of optical coma.

Light waves are subject to aberrations, defined as a property of optical systems to spread light over an area, larger than what is predicted by paraxial approximation. Reducing the aberrations in optical systems has been historically the most significant endeavour in the field, with significant results in both scientific and consumer equipment. However, when focusing in bulk material, light travels through an air-material interface, which causes strong aberrations, as pictured in Figure I.11. Index-matching immersion is a usual method to decrease aberrations in microscopes, but difficult to implement in scanning methods over large areas. For processing, especially in the case of high refractive index materials such as diamond ($n_{\text{diam}}(\lambda = 1.03 \mu\text{m}) = 2.39$), adaptive optical methods can

¹²Kühn *et al.* [71] have theoretically demonstrated that pulse-front tilt symmetrisation for simultaneous spatio-temporal focusing is possible, using specific optical design.

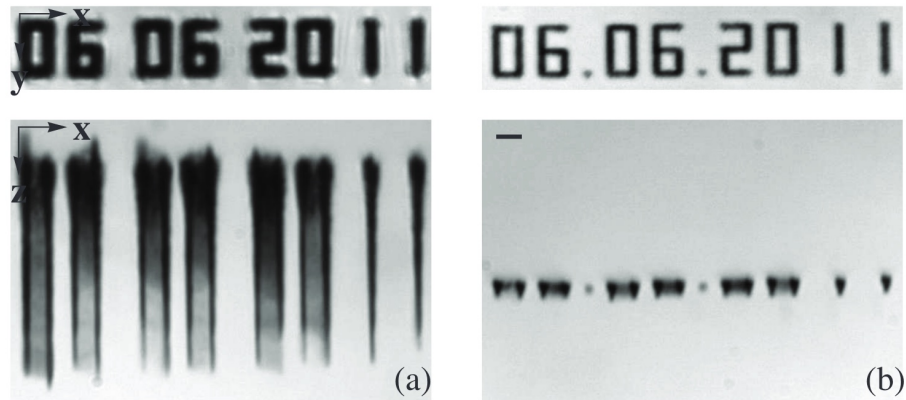


Figure I.12: Top (xy), and side (xz) views of a date inscribed in bulk diamond with a femtosecond laser. (a) shows the uncorrected outcome with aberrations, while (b) shows the outcome when they are compensated for by adaptive optics. Aberrations notably strongly expand the laser-affected zone in the direction of the optical axis. Scale bar: $5\ \mu\text{m}$. Reprinted from Simmonds *et al.* [39]

decrease them without requiring immersion, [39] as pictured in Figure I.12. Aberrations notably cause geometrical distortions of the modifications. [72, 73]

In this section, we have presented the variety of possible structures that femtosecond laser pulses can generate in glass. This variety arises from the complexity of laser-matter interaction processes. Given their outstanding complexity, performing *ab nihilo* characterisation methodologies is indeed long and difficult, with several post-mortem studies. The need for *in situ* monitoring and further controlling is manifest, as it would (a) alleviate the need for such intensive post-mortem experiments (e.g., wet etching, electron microscopy) for process calibration, and (b) allow for more resilient processes through control.

I.4 A taxonomy of observables

Let us now discuss here the available methods to probe the aforementioned types of laser-induced modifications. Note that we will limit on methods that can be easily integrated in a processing platform. For instance, electron spin resonance spectroscopy is a common method for detecting and characterising defects in glass, but the required equipment is too large to implement for *in situ* operation. Likewise, we do not consider methods requiring vacuum. Let us first discuss methods reported in the literature that have been devised for *in situ* monitoring, controlling, or that can be adapted to this specific application.

Phase information

Given the variety of modifications inducing refractive index change in glass, quantitative phase imaging is a natural method to consider. Most notably, Bricchi *et al.* [60] first measured the transmitted phase in laser-induced nanogratings, using scanning interferometry. This method is precise but slow as it requires scanning to form a phase map. Phase imaging techniques are plenty, most of them are however qualitative in nature, most notably phase-contrast microscopy. Some quantitative phase-contrast microscopy methods of laser-induced defects have been reported. Digital holographic microscopy as a wide-field quantitative phase imaging has been explored, [74] and pump-probe transverse phase imaging using Normarski microscopy, has also been studied for processing with high energy pulses. [73]

A notable challenge with implementing such a method is the required phase contrast. Laser-induced modifications, with low energy $E_p < 1 \mu\text{J}$ locally vary the refractive index in a range of $\Delta n < \pm 1 \times 10^{-2}$, in a small volume of roughly $1 \times 1 \times 10 \mu\text{m}$. *In situ* methods able to resolve minute dephasing for small volume must be determined.

Spectral activity

As mentioned in §I.3.1, several types of laser-induced molecular defects may exhibit photoluminescence, or increased absorption. An exhaustive summary of photoluminescence bands in fused silica is also presented in Table I.1. Significant spectroscopic work has been performed to identify and characterise the laser-induced defects, in several types of glass, given the importance of research into defects in glass optical fibres. Some examples of in-line probing have been demonstrated. Beaudier *et al.* [75] have demonstrated that *in situ* probing of NBOHC fluorescence in fused silica is a precursor to UV nanosecond laser-induced damage (in this study, $\tau_p = 8 \text{ ns}$, $\lambda = 266 \text{ nm}$).

Second harmonic generation (SHG)

Biological molecules typically exhibit strong second-order nonlinearity, given their highly non-centrosymmetric structure, [77] therefore SHG microscopy has seen significant development in this field. [78] Glass and centrosymmetric crystals, on the other hand, show a nil $\chi^{(2)}$, therefore bulk SHG is forbidden.¹³ Nonetheless, SHG occurs in optically damaged centrosymmetric media (e.g., fibres, bulk glass) after optical exposure [80] with a phenomenon dubbed optical poling. [81]¹⁴ Performing imaging of these regions has been performed, in what was originally coined as ‘dc electric field imaging’. [82] The

¹³SHG microscopy in the context of centrosymmetric crystal processing is naturally an option that has been exploited, e.g., in the case of lithium niobate that has a strong d_{32} value. [79]

¹⁴This effect is similar to thermal poling, which induces a dc electric field in non-centrosymmetric medium, such as glass, by applying high voltage. It has been shown that long exposure induces a semi-permanent periodic dc electric field, breaking the glass symmetry, hence allowing SHG.

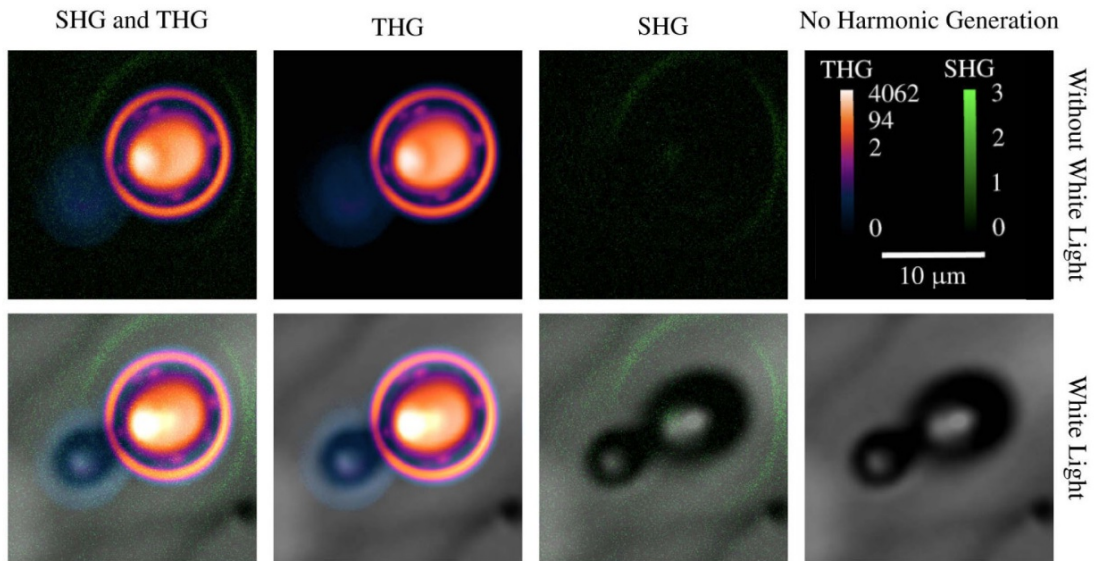


Figure I.13: Femtosecond laser-induced bubbles in fused silica, imaged using second- and third-harmonic generation microscopy, with and without white light background. All three imaging techniques highlight different areas, with THG notably being especially intense near the optical interfaces. Reprinted from Young *et al.* [76].

presence of enhanced SHG in femtosecond laser-processed glass is therefore not to be ignored. Interestingly, Young *et al.* [76] observed SHG in laser-induced bubbles in fused silica, as reprinted in Figure I.13. Finally, exposure of highly doped glass cause ionic migration, which causes giant local dc electric field embedment, able to generate strong SHG. [83]

Third-harmonic generation (THG)

THG is enhanced by interfaces, and optical heterogeneities. [84] Given the morphological nature of many femtosecond laser-induced modifications in dielectrics, and lack thereof in unexposed material, THG microscopy stands out as a potential efficient tool to detect presence of interfaces. Many laser-induced modifications (e.g., nanogratings, nanovoids, nanopores) show such glass-air interfaces.¹⁵ First studies of using THG as a tool for microscopy have been carried by Barad *et al.* [85] on optical fibres, then by Müller *et al.* [86] with biological samples, an application which became fruitful. [87–89] Studies have investigated using THG microscopy for analysing laser-written structures, [90–94] while others investigated the nature of the interaction with this method, including quill-writing. [95, 96].

¹⁵THG can as well be enhanced by resonance in the presence of a fitting electronic transition.

Chapter I. Introduction

An interesting point to raise in the case of THG is its sensitivity to birefringence. While phase-matching conditions forbids THG in isotropic and homogeneous materials, anisotropic materials can show significant THG. When exposed to fitting polarisation states, phase-matching conditions can be fulfilled. To discriminate the contributions from optical interfaces to the ones from birefringence, Oron *et al.* [89] have shown that using circularly polarised light eliminates the former to highlight the latter. This aspect is of scientific interest, considering the recent formalisation of three-photon Stokes-Mueller polarimetry, [97] and interest from the biology community. [37]

Conical harmonics generation in filaments

In a recent development, Grigutis *et al.* [98] have shown that during femtosecond pulses processing through filamentation ¹⁶, a cone of THG emission is observed. The angle of emission is shown to be exclusively dependent on the processed material, and follows noncollinear phase-matching conditions, considering the period of the filament-induced nanogratings. Such beams also emit conical second harmonic generation, as reported by Ardaneh *et al.* [99]

Diffraction by nanogratings

The periodic nature of type II nanogratings has triggered interest in attempting to observe their potential behaviour as diffraction gratings. Their typical period is however $T < 400$ nm, which requires using a UV source, focused on the same spot as the processing beam yet at an angle. Such an experiment is therefore difficult to achieve. An exploratory work from Mauclair *et al.* [18] showed that the periodicity of the nanogratings is indeed controllable, albeit the most significant processing parameter being pulse duration, which is not easily tuneable.

Summary

Figure I.14 provides a summary of the different methods considered, and Table I.2 provides the probed physical quantities with the associated references.

These methods come with varying implementability. In the case of harmonics generation and multiphoton fluorescence, the same laser can be used for both processing the material and probing it, significantly alleviating the requirements in terms of experimental complexity. Squier and Müller [90] notably took advantage of this practicality.

¹⁶A filament is a specific case of a femtosecond pulse propagating in matter: by tuning the pulse energy with the numerical aperture, the condition in which self-focusing is counter-balanced with defocusing caused by local ionisation. Laser-affected zones can therefore cover the whole sample depth, which is useful for high-speed processing, such as cutting.

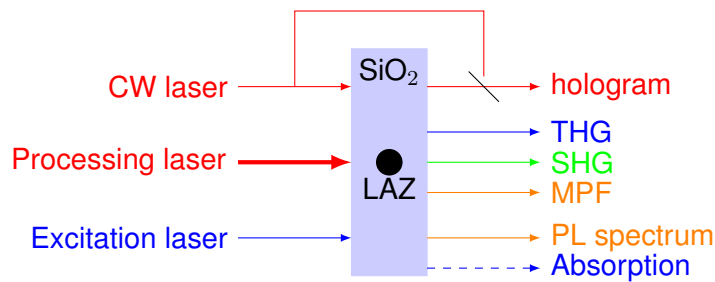


Figure I.14: Summary of the proposed monitoring methods. Holographic microscopy provides phase information through wavefront sensing. The processing laser itself can generate third-, second- harmonic generation, and multiphoton fluorescence in the laser-affected zones. Finally, a separate UV excitation laser can trigger photoluminescence, or be absorbed, by defects.

Method	Probed quantity	Scale	Associated refs.
Quantitative phase imaging	$\Delta n, n_e - n_o$	macro	[60, 73, 74]
Second harmonic generation	$\chi^{(2)}, E_{dc}$	meso	[81–83]
Third harmonic generation	$\chi^{(3)}, \vec{\nabla}n $	meso	[91, 92, 94–96]
Direct PL, or absorption probing	N_{defect}	micro	[75]
Nanograting diffraction	T_{grating}	meso	[18]

Table I.2: Available monitoring methods of laser-affected zones, reported in the literature.

Measuring photoluminescence and absorption requires, in the case of laser-exposed fused silica, additional UV probing, which is difficult to achieve efficiently with the IR-antireflective coated optics needed for processing. Such a method is however fitting in the context of UV-laser processing. [75] *In situ* measurement of diffraction caused by nanogratings is an experimentally difficult endeavour, due to the required illumination at an angle from the optical axis. It also needs a UV source, considering the typical 200 nm period of nanogratings.

Quantitative phase imaging requires an external laser source, whose wavelength can be close to the processing one. This means that imaging can be performed coaxially, significantly simplifying optical delivery. Holography is a method of choice here, as no special optics are required, such as Wollaston prisms for Normarski microscopy. However, a reference beam has to be brought to the sensor.

I.5 Thesis outline

In this introduction, we have shown the fundamental principles of non-ablative femto-second laser processing of dielectrics, its complexity, and a great challenge for its development: to characterise *in situ* the process outcome. As we have seen, several studies have been carried out, with varying levels of success and capacity to implement in an industrial setting.

Chapter I. Introduction

In this thesis, we strive to investigate new approaches to address this problem. Several criteria were selected to appreciate which ones to privilege. First, we will study methods proven *ex situ*, but not yet *in situ*. This choice emerges from the fact that, implementing known methods *in situ* will yield a significant amount of data, for which prior observations in the literature could give important insight. Another criterion is naturally the implementability into an existing setup, with as little hindrance to the inscription capabilities as possible. Several methods taking advantage of complex experimental setups (e.g., transverse imaging, diffraction) were deemed detrimental to this criterion. In this work, all proposed methods are optical in nature, and, in particular, use trans-illumination,¹⁷ out of experimental convenience.

This thesis is divided into three chapters, arranged in themes. The first chapter consists of a study regarding the viability of quantitative phase imaging, a method mentioned in §I.4. This method requires computational power, as purely optical methods only allow either average phase measurements (e.g., Michelson interferometer), or qualitative phase retrieval (e.g., Normarski microscope). Here, we use digital holographic microscopy to quantitatively probe refractive index modifications caused by laser exposure. The computational power needed to retrieve this map is however significant, therefore live control is not achievable. Nonetheless, through heuristic modelling and high data throughput, we show that a digital twin-based input shaping method can reduce directional effects and can reach finer inscription resolutions.

The second chapter of this thesis focuses on nonlinear imaging techniques. Previous studies used high-resolution nonlinear imaging to resolve structures hidden inside the laser-affected zones. Here, we use a photon-counting array to collect the second-, third-harmonic, and multiphoton fluorescence emissions in the far-field. We can observe significant variations in the signal, that we correlate with different types of modifications.

The third chapter of this thesis consists in an assembly of demonstrations of the methods studied in the previous chapters. We will show examples of inscription of low-loss phase maps in fused silica, using digital-twin based input shaping. We will use third-harmonic generation microscopy to unravel certain aspects of the light-matter interaction, most notably the statistics leading to modification, the law ruling the threshold number of pulses needed for pulses of a given fluence to trigger a modification. We will also address other insights.

¹⁷Trans-illumination means that probing light is travelling through the studied sample, there are therefore two distinct illumination and collection (or imaging) lenses. The opposite method is *epi*-illumination, where light is reflected by the sample at an angle. A specific case of *epi*-illumination is reflection illumination, using a single lens for both illumination and collection.

II Monitoring and feedforward control based on phase contrast imaging combined with a digital twin

This chapter is based on: O. Bernard and Y. Bellouard. 'On the use of a digital twin to enhance femtosecond laser inscription of arbitrary phase patterns'. In: *Journal of Physics: Photonics* 3.3 (2021), p. 035003. ISSN: 2515-7647. DOI: 10.1088/2515-7647/abf743

Chapter II. Monitoring and feedforward control based on phase contrast imaging combined with a digital twin

As seen in the previous chapter, laser-modified structures have a different refractive index compared to pristine material, that may also introduce form birefringence. Hence, quantitative phase-contrast imaging comes as a method of choice for monitoring laser-affected zones. This is typically performed by measuring interfering wavefronts.

For implementing quantitative phase-contrast microscopy, we have chosen digital holographic microscopy (DHM) [101–104] as a convenient method for obtaining wide-field, *in situ* phase images of transparent substrates. The phase is retrieved computationally from the hologram. Several steps of image processing are required to separate amplitude and phase contributions to the hologram.

Being computationally intensive, this method is limited for active control, but as we will see in this chapter, it is nonetheless useful for wide-field monitoring of laser-written patterns. As such, it is useful for monitoring the coupling between laser-affected zones.

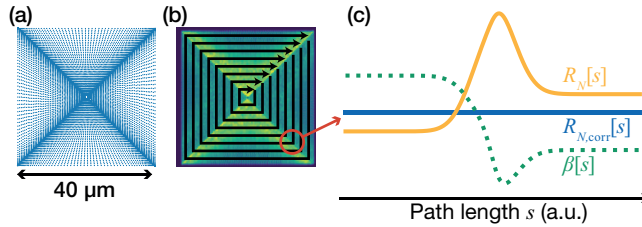


Figure II.1: Representation of the digital twin-based processing, used for equalising the phase pattern inscribed by a complex shape, i.e. concentric, clockwise, and expanding squares. (a) shows the position profile as the platform travels through the motion program. The dynamics of the platform are clearly identifiable. (b) shows the modelled phase map expected for such a motion programme with constant pulse energy, with the motion pattern overprinted. (c) is a visualisation of the compensation process on a corner. $R_N[s]$ is the retardance induced as the beam travels along the track (path length s). Near the corner, retardance peaks, and values further diverge away depending on which direction the beam travels (asymmetry). Using the digital twin, a compensation vector $\beta[s]$ can be deduced, so that the inscribed retardance $R_{N,cor}[s]$ is constant.

Here, we use digital holographic microscopy to feed a numerical model we call a *digital twin*. Considering a laser scanning path, this model predicts the shape of the induced phase plate. From this model, we show that we can deduce an energy modulation vector to induce a direct-write arbitrary phase map with the same path. Figure II.1 illustrates this process.

II.1 Methods and setup

II.1.1 Principles of digital twin-based processing

Phase-contrast digital holographic microscopy is an interferometric imaging method, with an example pictured in Figure II.2. One beam is imaged in transmission, as in a conventional microscope. It creates a hologram after interfering with a reference beam, generated from the same source. Typically, a motorised delay line adjusts the optical path difference between both beams to find optimal coherence, allowing higher hologram contrast.

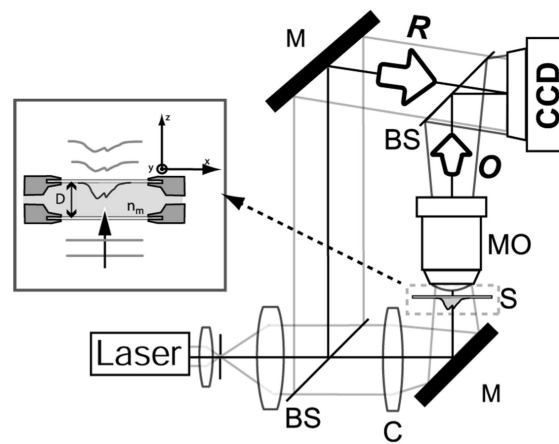


Figure II.2: Typical configuration of a transmission digital holographic microscope (DHM). A beam-splitter separates the reference beam (**R**) from the object beam (**O**). The latter images the region of interest in the specimen (**S**), in both absorption, and phase. A hologram forms on the array sensor (here, CCD). This allows retrieving both the intensity and the phase of the wavefront, thereby performing quantitative phase-contrast imaging. Reprinted from Marquet *et al.* [104]

An array sensor acquires the hologram – from which a reconstruction algorithm deduces the wavefront $\Psi(u, v)$. Thanks to the rich information carried by the hologram, numerical lenses are applied to numerically adjust the focus. From the complex reconstructed wavefront, the phase map is digitally retrieved through Fourier filtering.

In the context of laser processing, wide-field phase images can be used to optimise the parameters of a numerical model of the process, commonly called a ‘digital twin’. Such a model takes the exposure parameters (including the laser scan path) and simulates a single array output: the expected retardance map.¹ If accurate enough, the digital twin allows swift testing of several parameters, without physically carrying the experiments. Developing a digital twin is by itself a modelling endeavour, with a knack at quick solving

¹In this thesis, we define *retardance* as the difference between the refractive index of the laser-affected area, and the pristine material $\Delta n = n_{LAZ} - n_0$. In practice, the DHM measurement is performed at a fixed linear polarisation state.

Chapter II. Monitoring and feedforward control based on phase contrast imaging combined with a digital twin

and efficiently using experimental data. Given the lack of the generation of laser-induced retardance, the model implemented here is heuristic. Optimising the simulations with the actual exposure conditions, and experimental retardance maps, determines the digital twin parameters, using nonlinear optimisation algorithms.

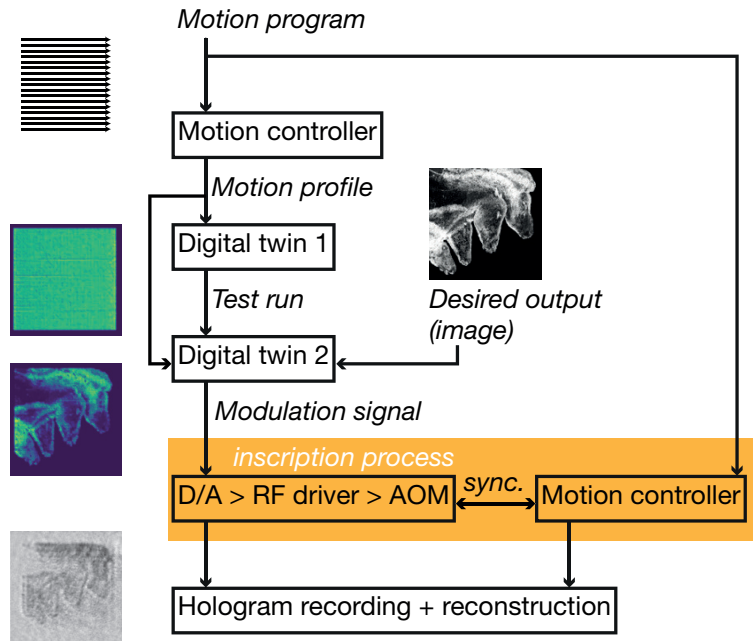


Figure II.3: Diagram of the digital twin-based control process here considered. A calibration run with the laser beam off collects the measured positions as a function of time (*motion profile*) from the motion controller (instructions given in the *motion program*). A first run in the digital twin yields the base phase map (*test run*). A second run, using the same motion profile and the data outputs from the test run, generates the *modulation signal* needed to achieve a *desired output*, in the form of an image. A fast AM module emits this modulation signal, while being synchronised with the motion program, to achieve the desired output. Process outcome can be immediately controlled using the built-in digital holographic microscope. The model correctly predicts both the needed input-shaped modulation signal and the process output. As an illustration, the pattern chosen here is a prehistoric painting of horses from the Grotte Chauvet at Vallon Pont-d’Arc (France).

Once the digital twin is optimised, it can assist inscription of phase maps. Figure II.3 presents the detailed algorithm flow chart. A *blank run* outputs the exact positions of the processing platform from the motion program at regular time intervals, considering acceleration profiles. These positions are satisfyingly reproducible in this context. Modelling the stages’ dynamics replaces this step when considering larger phase maps.

The motion profile is then used to generate a ‘canvas’, with constant irradiation parameters. Specifically, areas exposed with an accelerating or a decelerating beam would get increased exposure, and therefore different phase values. This is called the *test run*. This modelling part is used to optimise the process parameters with an experimental phase map.

From the test run, the parameters for the desired output can be deduced. This user input can be a constant value, as in Figure II.1. Any arbitrary image can function as input, as in Figure II.3, which can be seen as a ‘desired perturbation’ from the pattern obtained using constant illumination. Considering the motion profile, the model outputs an amplitude modulation (AM) signal, representing the pulse energy signal the beam should follow at a given position and time, thanks to the motion profile.

The modulation signal is emitted, synchronised with the motion. A Python script on a computer loads the signal onto a digital-to-analogue converter, connected to an acousto-optic modulator, through a fixed-frequency RF driver. Both need to be accurately synchronised. Implementing semaphores in the motion program allows this, by triggering pulses activating the modulation signal, which is segmented to this effect.²

In-line DHM allows to monitor the outcome of the process and is used to accurately optimise the model parameters. For the method currently presented, we perform this step manually, as a calibration step.

II.1.2 Processing platform

This experiment is built around an existing laser processing platform, as shown in Figure II.4. Two orthogonal servo translation stages (PI Micos GmbH) move the sample in the \vec{e}_x and \vec{e}_y directions, defining a plane parallel to the focal plane. A vertical stepper stage displaces the objective lens, hence the focal plane. A computer numerical control (CNC) motion controller drives the stages, using machine control instructions similar to G/M-code.

In the first step of the algorithm, a motion program is carried while the positions are saved periodically every 1 to 10 ms in the controller’s dual ported RAM (DPRAM).³ Given its reduced capacity (120 positions before overflow), data is saved on the PC every move, to retain high precision. A semaphore triggers saving, and later keeps the inscription process synchronised with the signal. Here, an instruction in the motion program triggers the semaphore, then waits for the memory to be fully copied. Once it is done, the PC program pulls the semaphore down, and the program resumes.

²**On semaphores.** The motion controller emits a TTL signal that acts as a gate, **SHUTTER**, allowing the beam through the platform. A rising **SHUTTER** triggers the amplitude modulation signal for this movement as well, allowing a beam modulated as desired through. Once the movement is performed, the script loads the next signal segment, and another semaphore, **HOLD**, is raised, to prevent the motion controller from going further. Once loading is finished, **HOLD** is lowered by the script, and processing can continue until the end.

³DPRAM allows simultaneous writing and reading RAM variables by multiple users, here by the motion controller and by the PC, respectively. In this case, positions values are written at every machine tick in 48 bit-format, during a movement, and stops doing so when either the DPRAM is full, or the movement stopped.

Chapter II. Monitoring and feedforward control based on phase contrast imaging combined with a digital twin

A modulation signal for a dense $40 \times 40 \mu\text{m}$ square is computed in typically 5 s on a 2.4 GHz Intel Core i5 processor. In the inscription process, the modulation signal is uploaded to the digital-to-analogue converter (Digilent, Analog Discovery 2). The semaphores are here used to trigger the signal, so that it is synchronised with the motion program. The analogue signal is sent into an RF-driver that commands the AOM to modulate the laser power.

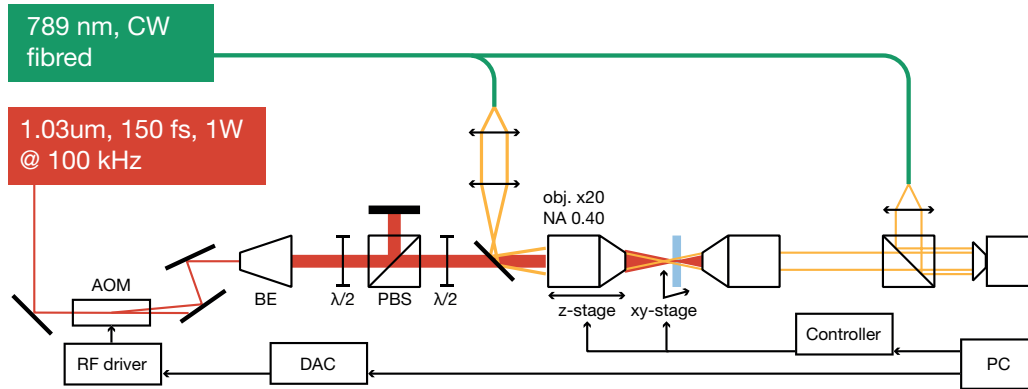


Figure II.4: Schematic of the processing setup, with an integrated transmission digital holographic microscope (DHM). An Yb: fibre oscillator and a Yb-based regenerative amplifier generate the pulses. Acousto-optic modulator (AOM), driven through an RF driver, modulates their power. A beam expander (BE) adjusts the beam size to fit the entrance pupil of the machining lens. A half-wave plate ($\lambda/2$) and polarised beam splitter (PBS) split the beam towards other experiments. A second half-wave plate control the linear polarisation stage. The machining lens focuses the beam to achieve high intensity in focus. To achieve holography, a fibre pigtailed-CW diode laser is split between a reference and an object beam, the latter illuminates the sample through both the machining and collecting lenses. After recollecting the object beam, both merge in front of the camera, which captures the hologram. The PC runs the motion controller's software, as well as the digital twin-based process by driving a digital-to-analogue converter (DAC), modulating the laser power. The camera sends data to the PC, on which the reconstruction program runs.

Figure II.4 shows the processing platform with the built-in DHM. This platform uses as femtosecond laser source a Yb: fibre mode-locked oscillator operating at 40 MHz, pulse-picked at 100 kHz for amplification in a Yb-based regenerative amplifier (Amplitude Systèmes SA, S-Pulse HR SP). The system outputs 150 fs FWHM-long pulses (FROG measurement, GRENOUILLE, Swamp Optics), and a maximum of 1 W of average power. An acousto-optic modulator (AOM) diffracts pulses at the first order depending on the RF power delivered by the driver, modulated by an external source (here, the digital-to-analogue converter). After modulation, the beam is expanded using an adjustable beam expander to fit the entrance pupil of the machining lens (here, 8 mm), so that the highest numerical aperture allowed by the lens (hence smallest spot size) is achieved. A motorised half-wave plate controls the linear polarisation direction. The beam is focused using a high-power objective lens (20x, 0.40 NA, Optosigma PAL-20-NIR-LC00). With fitting entrance beam conditions (i.e., alignment, beam diameter, here 8 mm), a spot diameter of $2.5 \mu\text{m}$ is achieved. Pulse intensities can therefore reach 1 PW cm^{-2} .

II.1.3 Phase-contrast imaging system using an on-axis digital holographic microscope (DHM)

We perform laser processing with a coaxial DHM observing the region of interest (ROI) around the focal spot of the machining beam. The DHM (Lyncée Tec SA) fibre pigtailed laser source operates CW at 794.5 nm. A fibre splitter splits the beam between a reference, directly brought near the camera, and an object beam. The latter illuminates the ROI coaxially, as it travels through the machining objective lens. A lens defocuses the object beam before it combines with the machining beam, so that the illuminated field is wider than the machining spot at the focal plane of the latter.⁴ The ROI is imaged through a high-magnification DIC microscope lens (Leica Microsystems N PLAN EPI 100x/0.85 NA). Both reference and object beams then merge, using a 50:50 beam splitter. to generate a hologram in the sensing plane of the CMOS camera. The reconstruction software (Lyncée Tec SA) processes the data from the camera, and converts the hologram into amplitude and phase maps, at a framerate roughly 10 fps.

II.2 Digital twin

The fundamental model behind the digital twin relies on a physical model, detailed in this section. First, the effect of several pulses to the phase map will be considered, followed by a development into numerical considerations (discretisation), then optimisation of parameters, and finally the generation of modulation signals.

II.2.1 Analytical modelling

The model is inspired from the work of Chichkov *et al.*, [105] developed in the context of ablation, and derived from a two-temperature model. [106] Here, we expand this model to consider the anisotropic effects discussed in §I.3.3.

We consider bursts of fixed number of pulses, rather than individual ones, to alleviate computing power. The high repetition rates used during exposure, here $\nu_{\text{rep}} = 100 \text{ kHz}$, and the relative slow frequency of motion profiling, ranging 100 to 500 Hz, motivate this choice. A burst typically contains 200 to 1000 pulses, depending on the motion profiling frequency used. Given the slow scanning speeds, pulses overlap significantly (OL > 99 %).⁵ In this heuristic model, we assume every pulse in a burst arrives at the same position, as the beam size is much larger than the shift between consecutive pulses.

⁴Effectively, the focus of the object beam lies beneath the focus of the machining beam. A numerical lens compensates for this effect.

⁵Overlap is a dimensionless quantity, representing the *already exposed area* an incoming pulse travels through. It writes

$$\text{OL} = 1 - \frac{v_s}{2w_0\nu_s}$$

Chapter II. Monitoring and feedforward control based on phase contrast imaging combined with a digital twin

We consider the problem to be two-dimensional, as we consider a single focal plane. In other words, the exposure happens in a single z position and in polar coordinates $(O, \vec{e}_\rho, \vec{e}_\phi)$. A burst of pulses generates a modification at the origin O . The retardance induced by this burst defined as $R_1(\rho, \phi)$ can be heuristically described with a function of the pulse fluence F , the apparent fluence threshold F_{th} , and a polar distribution of the energy $\Xi(\rho, \phi)$, expressed as:

$$R_1(\rho, \phi) = r_0 \ln \left(\frac{F}{F_{\text{th}}} \Xi(\rho, \phi) \right) \quad (\text{II.1})$$

where F_{th} is the threshold fluence for which a burst with a superior maximum pulse fluence will induce a measurable retardance increase in the material, and r_0 is a normalised retardance value, here set to unity. Both quantities are calibrated experimentally before exposure, using the DHM. In practice, we rewrite the ratio F/F_{th} as $(1 + f)$, a normalised dimensionless fluence value, while r_0 is kept to preserve the physical dimension of the equation. Note that a pristine material has a defined retardance value of 0 nm, and the model predicts relative variations.

Let us now consider the n -th burst. To take into account the effect of the previous burst, this model is recursive, hence, each step $R_n(\rho, \phi)$, $n < N$ must be computed, with N being the total amount of bursts in the exposure. Similarly to an arithmetic progression, each step takes the form $R_n(\rho, \phi) = R_{n-1}(\rho, \phi) + \Delta R_{(n-1) \rightarrow n}(\rho, \phi)$, with the latter element to be computed. Consecutive pulses modify the material in a nonlinear manner. Indeed, an already modified substrate has a very different response to exposure than a pristine one, in what is referred as *saturation*. Indeed, laser-induced nanostructures atop the focal plane increase scattering, and therefore reduce the effective optical intensity near the focal point. A simple way to account for this effect is to modify Equation II.1, and multiply the threshold fluence by $[1 + \alpha R_{n-1}(\rho, \phi)]$, with α being a saturation factor. A pristine area would still have an effective fluence threshold of F_{th} , but an already exposed one would increase its value. We can express the retardance, replacing F/F_{th} with $(1 + f)$, as such:

$$R_n(\rho, \phi) = R_{n-1}(\rho, \phi) + r_0 \ln \left[\frac{(1 + f)\Xi(\rho, \phi)}{1 + \alpha R_{n-1}(\rho, \phi)} \right] \quad (\text{II.2})$$

In this equation, $\Xi(\rho, \phi)$ represents the spatial distribution of the retardance induced by a single burst. This distribution comes from the pulse shape, but also other anisotropic aspects, such as pulse-front tilt. Considering a perfectly Gaussian retardance imprint, we would write $\Xi(\rho, \forall \phi) = \exp(-\rho^2/w_0^2)$. To encompass all the directional effects, and considering that we use a roughly Gaussian beam, we approximate a modified polar

with v_s the scanning speed, w_0 the beam waist, and ν_p the pulse repetition rate.

Gaussian distribution:

$$\Xi(\rho, \phi) = \exp\left(\frac{-\rho^2}{w_0^2 [1 - e^2 \cos^2(\phi - \phi_0)]}\right) \quad (\text{II.3})$$

where e introduces an elliptical parameter of the distribution, ϕ_0 its absolute orientation, and w_0 a beam size for the $e = 0$ case. All these parameters, except w_0 which is fixed, are devised experimentally through model optimisation.

By developing all elements together, we write the final equation:

$$\frac{R_n(\rho, \phi) - R_{n-1}(\rho, \phi)}{r_0} = \ln\left(\frac{1 + f}{1 + \alpha R_{n-1}(\rho, \phi)}\right) - \frac{\rho^2}{w_0^2 [1 - e^2 \cos^2(\phi - \phi_0)]} \quad (\text{II.4})$$

that describes the relative increase of retardance with exposure.

II.2.2 Discrete pattern description

Equation II.4 defines the analytical sequence we use in the context of the digital twin. To compute this progression effectively, let us consider converting it to a discrete equation.

The laser irradiates a moving sample, hence the positions of successive bursts vary. To simplify computation, and for switching between polar coordinates $((\rho, \phi)$, for Equation II.4) and cartesian coordinates $((x, y)$, for linear sample displacement) we define a retardance array $R[z]$ with $z \in \mathbb{C}$ being the position expressed as a complex number: $z = x + iy$, and $z = \rho e^{i\phi}$. The n -th pulse has an added contribution $\Delta R_n[z; z_n, R_n]$, with z_n and z_{n-1} being the centre positions of the n -th and $(n - 1)$ -th pulse. Thanks to the conversion in complex positions, relative polar positions are easily computable: $\rho = \|z\|$, and $\phi = \arg(z)$.

The array $R[z]$ is much larger (width $\sim 100 \mu\text{m}$) than the typical modification size ($w_0 = 1 \mu\text{m}$). To alleviate computation, we calculate variations in the array with a ‘moving square’ method, centred on z_n . $\Delta R_n[z; z_n]$ is only calculated in the vicinity of z_n , in a square $2w_0$ of side length, so that only the significant variations are appended to $R[z]$.

We consider as initial condition $R_{n=0}[\forall z] = 0$. To account for energy modulation, we consider f to be dependent on the burst n : f_n . In discrete form, Equation II.4 writes:

$$\frac{\Delta R_n[z; z_n]}{r_0} = \ln\left(\frac{1 + f_n}{1 + \alpha R_{n-1}[z]}\right) - \frac{\|z - z_n\|^2}{w_0^2 [1 - e^2 \cos^2(\arg(z - z_n) - \phi_0)]} \quad (\text{II.5})$$

II.2.3 Model optimisation

To correctly predict the output of the inscription process, the model parameters, namely α , e , and ϕ_0 , must be adjusted to the actual experiment platform. In practice, we use a target similar to the one shown in Figure II.5, with concentric squares. This allows to highlight the pulse anisotropy inherent to any laser processing system. Once this target is inscribed, the experimental phase map of the target is retrieved.

To optimise the parameters, the motion profile is uploaded to the model. We perform optimisation with the Broyde-Fletcher-Goldfard-Shanno nonlinear optimisation algorithm (L-BFGS-B), [107] which has the advantage of being bound-constrained, to facilitate convergence. The optimisation step must be performed for any significant change in experimental conditions, like optics change, different material.

II.2.4 Determining the modulation signal

All of Equation II.5 can be computed, after optimisation of parameters. Let us now consider the case of varying f_n , the modulation signal, so that the final phase map nears the input map, i.e., $R_N[z] \propto R_{\text{des}}[z]$, with N being the total number of bursts considered. The test run generates a phase map $R_{\text{test}}[z]$, depending on the motion profile provided. Assuming the digital twin provides an accurate prediction, it can serve as a reference for computing a modulation signal, able to inscribe the desired output.

The modulation signal must be expressed as a function of time. Motion profiling gives the burst ordinal number, its position, and time. Therefore, retardance needs to be expressed in terms of motion path length quantised by bursts: s_n . Motion positions do not, however, correspond to the array mesh: quantisation is used to derive $R_n[s_n]$ from $R_n[z]$.

Quantisation gives both $R_{\text{des}}[s_n]$ and $R_N[s_n]$. From there, we assume that f_n must be computed considering the *derivation* of $R_N[s_n]$ from its mean. It must also be pondered by R_{des} at-large. A simple formulation writes:

$$f_n = R_{\text{des}}[s_n] [\gamma_0 - \gamma_1 (R_N[s_n] - \langle R_N[s_n] \rangle)] \quad (\text{II.6})$$

where γ_0 and γ_1 are two arbitrary parameters, optimised by comparing the corrected model outputs with the inputs. The unbound nonlinear BFGS algorithm [107] is used to fit these parameters in a reduced amount of time.

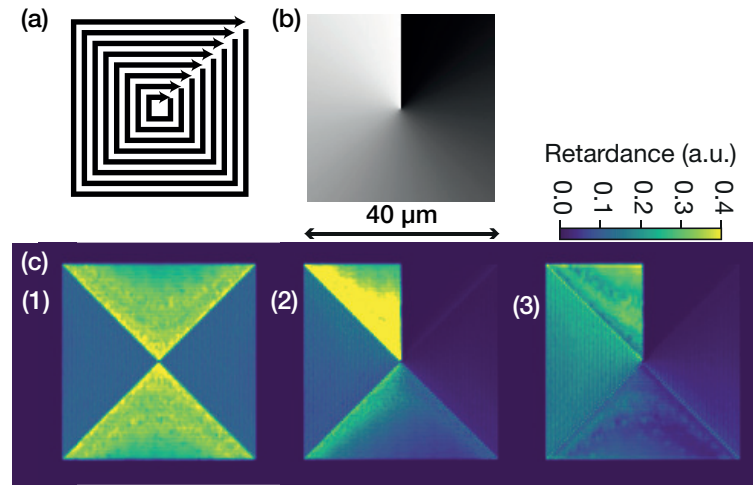


Figure II.5: Illustrations of the functioning of the digital twin. (a) is a drawing of the motion program, consisting in expanding, clockwise, and concentric squares. (b) shows the desired output image, here the phase map of an optical vortex, taken as an example. (c.1-3) show model outputs, exposing with (c.1) constant energy (i.e., no modulation), (c.2) *naive* modulation (ignoring modelling), and (c.3) digital twin-generated output. The need for path compensation is highlighted by the difference between (c.2) and (c.3), aiming to achieve the phase map on (b).

To illustrate the algorithm steps, Figure II.5 shows examples of a specific path strategy, virtually compensated to inscribe an optical vortex. This shows that this method is viable for compensating directional effects. The difference between the ‘naive’ process, that does not take into account the anisotropic character of the beam, and the digital twin-assisted processes are highly significant. The coming section proves this experimentally.

II.3 Experimental demonstration

This section addresses experimental observations, and discussions around them. The first subsection focuses on the effect of pattern rotation, more specifically the one Figure II.5 presents, to verify the validity of the model, especially in the case of anisotropic behaviour. The second subsection shows the inscription of arbitrary phase maps using this method. The last subsection discusses the achievable resolution. All experiments are performed in 0.25 mm-thin, optically polished fused silica samples (Corning 7980 0F).

II.3.1 Effect of pattern rotation

As a demonstration of the validity of the digital twin, we compare its predictions to experimental phase maps acquired using the *in situ* DHM. We use a shape like the one previously considered, which exhibits strong directionality: this motion program shows lines inscribed in four different directions. The high magnification of the imaging lens

Chapter II. Monitoring and feedforward control based on phase contrast imaging combined with a digital twin

allows to inscribe small yet dense structures: the line pitch is $0.5\ \mu\text{m}$, while the largest concentric square has a width of $40\ \mu\text{m}$. This pattern is highly non-optimal, given the many sequences of strong acceleration and deceleration of the moving stages, and the high density of lines. Its purpose serves in benchmarking the process, so that it is more resilient under more conventional exposure conditions. However, in an ideal isotropic case, all quadrants would appear similar to each other. To verify the digital twin's resilience, we inscribe the same pattern four times, rotated by 15° each time.

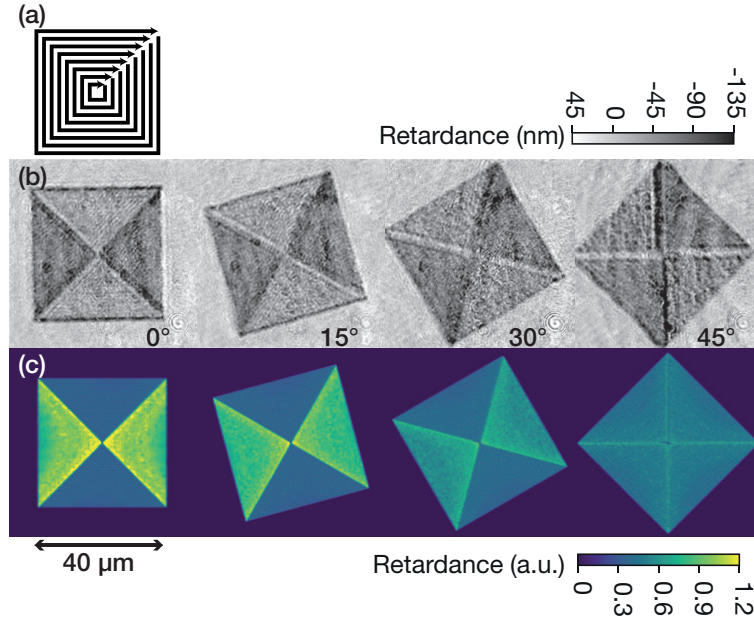


Figure II.6: Rotation of a highly directional motion pattern, as drawn in (a). (b) shows the experimental phase maps acquired through the DHM, for different orientations. (c) shows the model predicted output for the same exposure conditions. At 0° , the pattern clearly displays four quadrants. As the angle increases, these quadrants dim until they are indiscernible at 45° .

Figure II.6 shows experimental results compared with the predicted outputs of the digital twin. The dependency on the pattern output is indeed highly dependent on its direction. At 0° , ⁶ quadrants appear, depending on the writing direction. This highlights that there are preferred directions for the inscription process, despite the beam being circular and the material itself being isotropic. Increasing the angle reduces this contrast, until the point where all quadrants become similar. The boundaries between quadrants remain visible, as they represent sharp discontinuities in scanning speed, which likely induce different types of modification.

The digital twin correctly predicts the shape of the phase maps, depending on the angle. The ellipsoidal distribution presented in §II.2.1 here correctly encompasses the process anisotropy.

⁶The angles are defined by rotating the coordinate system of the motion controller along the \vec{e}_z axis. 0° corresponds to the native coordinate system, i.e., the X stage exclusively moves on the \vec{e}_x axis.

The model satisfies the modelling conditions. Let us now address its capability to generate fitting modulation signals.

II.3.2 Inscription of arbitrary patterns

To test the digital twin, we use the same motion program as before. Two situations are tested: a case with *naive* modulation, i.e., the test run is ignored and replaced by a constant value, and a second case, where it is used. As per the preceding subsection, the case at 0° is taken as it shows the strongest possible anisotropy for this motion pattern, as another way to benchmark the digital twin.

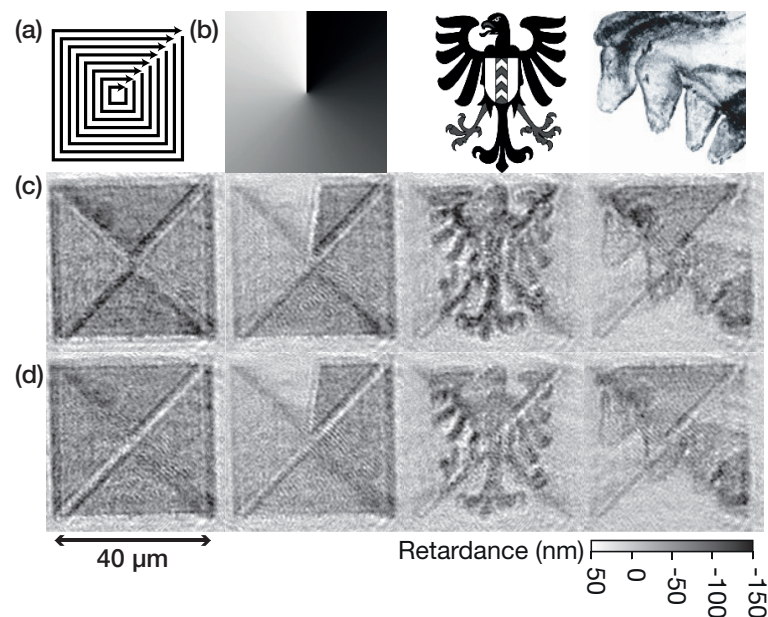


Figure II.7: Arbitrary phase map inscription with a square pattern, as drawn in (a). (b) shows the three input images chosen: a first-order vortex phase-plate, the seal of the city of Neuchâtel (Switzerland), and a reproduction of a prehistoric painting of horses (Grotte Chauvet, France). Rows (c, d) show phase images of inscription processes, on the leftmost column targeting a constant phase, then rightwards those shown in (b). Row (c) uses the *naive* process, while row (d) uses the digital twin-assisted process. Note that the quadrants fade away thanks to the digital twin, although their edges still appear, as they are not correctly taken into account. These represent an extreme case of sharp discontinuity.

Figure II.7 shows that, despite the highly anisotropic behaviour of the inscription, and the extreme path chosen, the process can compensate it. As imprints of the quadrants can be seen in (c), they are significantly dimmed in (d). However, they do not entirely vanish, which can be explained by a lack of refinement of the polar distribution.

Chapter II. Monitoring and feedforward control based on phase contrast imaging combined with a digital twin

In the other cases, the pattern edges still appear significantly. This can be explained by the sheer increase in pulse density near these edges: the modulation energy is close to the modification threshold, so that excess modification occurs with many more pulses. A refinement of the saturation model could alleviate this issue.

Other physical phenomena known to appear around laser-affected zones are not explicitly considered here, most notably stress. [108] Although expected to be low at such regimes, [109] modelling its effects would certainly increase the quality of the predictions and modulation generation, especially with a high density of lines, or discontinuities, in the pattern trajectory. Additional digital maps could be appended to this model to enrich sharp calculations, such as a stress map.

II.3.3 Towards sub-diffraction resolution patterns

In this experiment, bursts allow a precision in space of approximately 500 nm. This is smaller than both the spot size and the diffraction limit. However, nonlinear processes can beat the diffraction limit and generate features smaller than it, such as nanogratings. It is therefore of interest to see if we can generate such features. The problem lies in the DHM itself. Its lateral spatial resolution is limited to 1.3 μm , and hence cannot resolve such feature sizes.

To increase the writing resolution, we adopt a raster scanning method. Lines are written across the whole processing area in the same direction, i.e., from left to right. §IV.1 demonstrates further the advantages of this scanning method when writing phase maps. This strategy allows to avoid path changes in the centre of the exposed area, by reducing sharp discontinuities. The effect of directionality is moderated, as a single writing direction is kept. Motion sampling is also more consistent during motion profiling, which will reduce position uncertainty: this is necessary to achieve effective sub- μm precision.

We use Moiré patterns to reveal periodic sub-diffraction limit structures in a scale observable by the DHM. The base pattern is a vertical grating, inscribed by horizontal scanning. Two overlaid patterns of same period, rotated at an angle, generate larger-scale Moiré fringes. It appears if both patterns are within the depth of focus of the imaging lens. The period of the Moiré fringes D depends on the period of the inscribed patterns p , and the tilt angle between them α . The relationship between these quantities writes $D = p / (2 \sin(\alpha/2))$. Under small-angle approximation, it writes $D \simeq p/\alpha$. Four experiments are performed: considering two periods p (1250 and 1428 nm), 64 and 56 lines respectively), and two tilt angles (8° and 12°).

Figure II.8 shows Moiré patterns achieved using this inscription method, observed with the phase output of the DHM. In the case of 56 lines, the calculated period is 1.71 μm , while the predicted one is 1.75 μm . In the case of 64 lines, an inconsistency appears: the

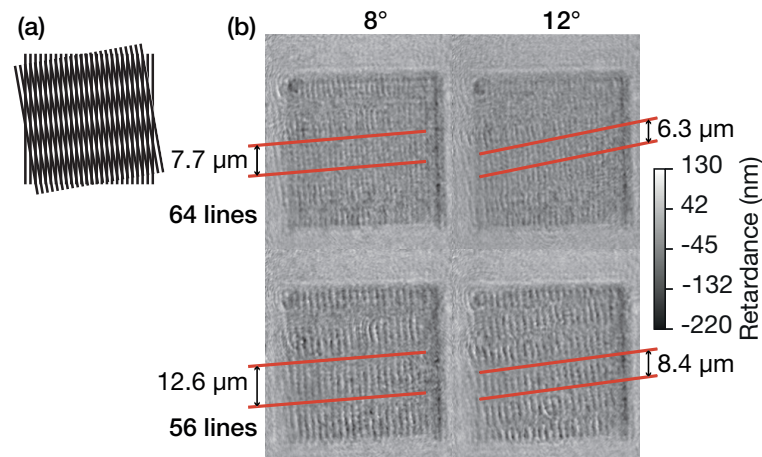


Figure II.8: Digital twin-assisted inscription of stacked Moiré fringes. The square size is $40\ \mu\text{m}$. (a) shows the principle of Moiré fringes with 80 lines at 10° , four wider beating fringes appear. (b) shows four examples of Moiré patterns to identify the smallest writeable structures using this method. The fringes are highlighted as well.

calculated periods are 1.08 and $1.32\ \mu\text{m}$ (for 8° and 12° respectively), while the predicted period is $1.25\ \mu\text{m}$. This is probably caused by inconsistencies in the writing process – as features get close to the spatial sampling rate (roughly $500\ \text{nm}$).

These observations confirm the ability to inscribe patterns with a smaller resolution than the diffraction limit. It seems that in this case, the process is limited by the spatial sampling rate of the process. These structures are nonetheless particularly difficult to observe and characterise *in situ*.

Conclusion and outlook

Femtosecond modification of bulk dielectrics is of physically complex nature, difficult to model. Further perturbations add to the complexity of the problem, make this process anisotropic, and nonlinearly dependent on several parameters. However, this does not mean that modelling is entirely impossible. As shown in this chapter, heuristic modelling on a band of process parameters is possible. This type of modelling will nonetheless be bound to the observation method used, and requires calibration, although fast.

In conclusion, we have shown that (a) a digital twin, built on a generated retardance model that takes beam anisotropy into account, can be used and tuned to correctly reproduce experiments virtually; (b) a DHM is a viable tool measure retardance, and to tune the model parameters; (c) can produce satisfying energy modulation, for arbitrary phase plate inscription, capable of writing smaller-than-diffraction limit structures, and (d) the method is robust enough to the effects caused by different writing strategies.

Chapter II. Monitoring and feedforward control based on phase contrast imaging combined with a digital twin

Although some issues remain, such as contributions from laser-induced stress, this approach provides a canvas from which further modelling can be performed in an efficient manner. Thanks to *in situ* observation, the digital twin can be tuned rapidly to correctly predict femtosecond laser exposure experiments.

III Full-field nonlinear microscopy as a means for monitoring laser- induced modifications.

Contents of this chapter have been pre-printed in: O. Bernard, A. Kraxner, A. Boukhayma, C. Enz, Y. Bellouard and J. Squier. *Third-harmonic generation monitoring of femtosecond laser-induced in-volume functional modifications*. preprint. 2023. DOI: 10.1364/opticaopen.22040459.v1

Chapter III. Full-field nonlinear microscopy as a means for monitoring laser-induced modifications.

As ultrafast laser sources matured, coherent nonlinear microscopy has emerged over the last two decades as a new modality for three-dimensional imaging in general. Amongst them, third-harmonic generation (THG) is a particularly interesting case in the context of observing laser-induced modifications. Endogenous image contrast results with THG: the coherent conversion process efficiency dramatically increases when intense light irradiate non-homogeneous optical media. [85] In practice, these conditions can be met using a mW-average power femtosecond laser, that is tightly focused (several micrometre spot size). Although predominately used for biological microscopy, [111] this method can also be used to image laser-induced modifications inside transparent materials in three dimensions, as demonstrated in Ref. [86] (see also Ref. [76] for a pragmatic implementation of THG microscopy).

This chapter considers two other nonlinear processes. Non-resonant second-harmonic generation (SHG) microscopy appears in media, where there is no inversion symmetry, e.g., non-centrosymmetric, or poled materials. Femtosecond laser-induced poling of glass is known to significantly enhance SHG in metal-doped glass samples, [83] but also fused silica. [81] Finally, multiphoton fluorescence is observable as well, where the material is excited by the n -th harmonic, and emits at a wavelength larger than that of the laser.

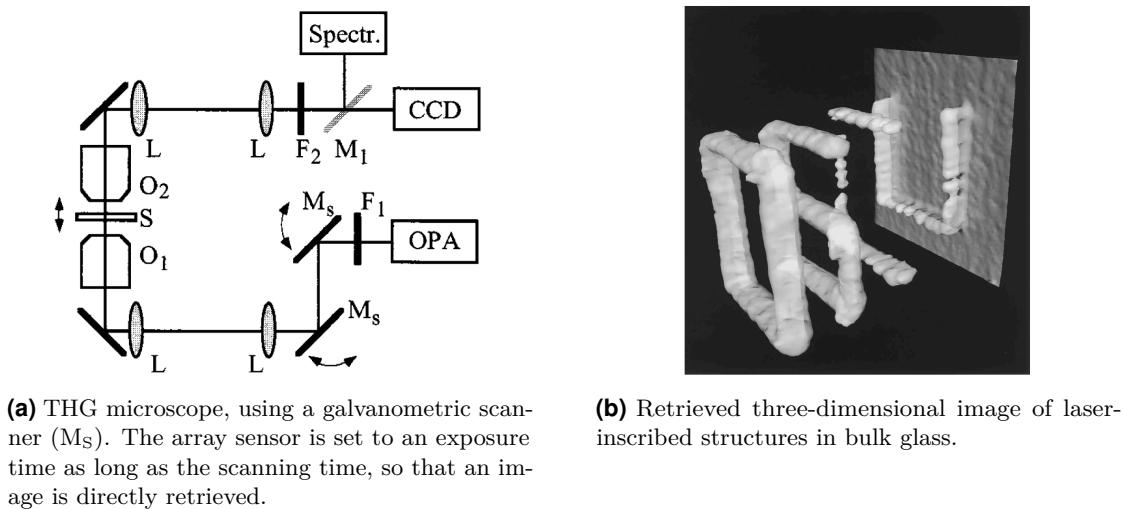


Figure III.1: Example of a pioneering work related to third-harmonic generation microscope imaging of laser-induced defects in glass, from Squier and Müller. [90]

As demonstrated in Refs. [90, 91], and pictured in Figure III.1, THG microscopy is an interesting choice for *in situ* imaging of the femtosecond laser-induced modifications in bulk glass. So far, these studies limited themselves to 3D imaging attempts of the contour of laser-modified zones, with no *a priori* correlation with the nature of the modification and in particular, their functional properties. Furthermore, these studies focused on exploiting laser scanning THG microscope arrangements, to form an image of the modified zones.

This study aims at expanding the capabilities of *in situ* THG, SHG, and MPF as characterisation tools, and to extract functional process parameters and incubation laws for a given material.

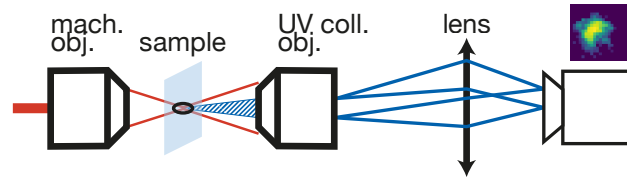


Figure III.2: Working principle of the in-situ, full-field third-harmonic generation (THG) microscope. A machining pulse modifies the material, which then irradiates the modified area with a sub-threshold fluence to generate THG. The area in focus acts as a diffraction-limited source of third-harmonic photons. The size of the source is at most the minimum waist of the objective at the focal point, i.e., $2.5\ \mu\text{m}$. An imaging objective lens collects all emitted THG, that forms an image on an array sensor. The far-field distribution (full-field) of THG is thereby retrieved.

Here, we explore the far-field intensity distribution (full-field) of THG, also called a ‘fingerprint’, thanks to a new type of low-noise CMOS imager capable of few-photons acquisition. Our study of laser-induced, SHG- and MPF-enhancing modifications is performed in scanning mode only. Figure III.2 pictures a working principle of this method. Full-field imaging obtained at a rate exceeding 100 FPS is achieved, out of which we correlate the shape of the THG fingerprints with functional properties of the exposed glass. By using a simple matrix of dots mapping the relevant laser parameters, we can identify the modification parameter space for the material, including singular regions, where selective etching is locally enhanced.

III.1 Experimental method

III.1.1 Processing platform

To perform this study, we developed a dedicated laser processing platform, as pictured in Figure III.3. The first part of the beam line (top half of Figure III.3) is common with the experiment presented in Chapter II, i.e., the source emitting at $1030\ \text{nm}$, and the AOM. Given the laser source considered here, SHG and THG occur at $515\ \text{nm}$ and $343\ \text{nm}$, respectively. A beam expander adjusts the beam size so that it fills the entrance pupil of the processing microscope objective lens (Thorlabs, Inc., MicroSpot LMH-20X-1064, $\text{NA} = 0.40$). This focusing optical system reaches a beam size of $2.5\ \mu\text{m}$.

Two piezoelectric stages displace the sample under the objective lens, while a third one displaces the processing objective lens along the optical axis, achieving 3D processing. A controller, connected to the PC, drives all three stages (Mad City Labs, Inc.). A

Chapter III. Full-field nonlinear microscopy as a means for monitoring laser-induced modifications.

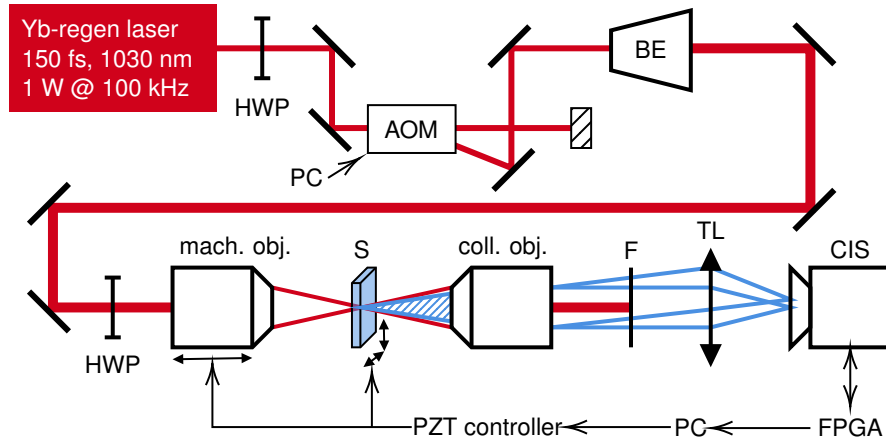


Figure III.3: Schematic of the combined laser processing platform with in-line THG microscopy. An Yb-based oscillator-amplifier system generates femtosecond pulses. An external acousto-optic modulator (AOM), controlled by the PC, modulates their energy. A beam expander (BE) adjusts the beam size to fit the entrance pupil of the machining lens. A half-wave plate (HWP) controls the linear polarisation state. A piezoelectric stage (PZT) displaces the machining lens, to control the position of the focal plane relative to the sample. 2D orthogonal PZT stages displace the sample. The collection lens collects all radiation coherently emitted from the laser interaction in the sample. Depending on the studied process (second- or third-harmonic generation, multiphoton fluorescence), a filter (F) only allows the desired radiation through. A tube lens (TL) then generates an image on the photon-counting image sensor (CIS). A dedicated FPGA drives the sensor, interfaced through the PC. This experiment allows simultaneous processing and nonlinear microscopy.

digital-to-analogue converter (Digilent, Analog Discovery 2) controls an RF driver, itself driving the AOM. This modulator acts as both a power modulator and a gate, to let pulses through.

Depending on the nonlinear process of interest, either of two collection objective lenses collect the image. For SHG and MPF microscopy, as their emission spectrum is in the visible range (in particular, 515 nm for SHG), we use a commercial objective lens (Olympus Corp., UMPlanFl 100X/NA0.9). As the central wavelength of the third harmonic is 343 nm, for which usual glass and anti-reflective coatings are unfit, we developed a custom objective lens, detailed in Appendix A.2. The collections lens is set on 3D manual translation stages for alignment purposes. The beam at infinity is then filtered, according to the method chosen: $\lambda_{BP,THG} = 343(5) \text{ nm}^1$ for THG ($\varnothing 12.5 \text{ mm}$ Edmund Optics, Inc. # 39-307), $\lambda_{BP,SHG} = 515(5) \text{ nm}$ ($\varnothing 12.5 \text{ mm}$ Edmund Optics, Inc. # 65-092) for SHG, and $\lambda_{LP,MPF} < 950 \text{ nm}$ ($\varnothing 25.0 \text{ mm}$, Thorlabs, Inc. FESH0950) for MPF. A tube lens then focuses the beam onto the photon-counting CMOS array sensor.

¹Values under parenthesis indicate the full width at half maximum (FWHM) of the bandpass filter.

III.1.2 Imaging optics

Third harmonic signal occurs at 343 nm. Most conventional imaging lenses use broadband antireflective coating centred around visible wavelengths, i.e., typically 400 to 800 nm, therefore they are unfit for THG imaging. Most objective lenses are achromatic (or achromat), which are composed of various glass of negative or positive dispersion, typically arranged in doublets or triplets. As an example, a common type of glass used in optical design is the flint N-SF5.² Its absorption coefficient at the THG wavelength is $\alpha_{\text{N-SF5}}(\lambda = 343 \text{ nm}) = 1.2 \text{ cm}^{-1}$, which is significantly high. [112]³ In the case of flint glass, their values imply significant absorption of already minute UV light. SHG and MPF suffer less from this effect, given that they happen in the visible spectrum, where conventional objective lens performance is satisfying.

Dedicated optics for THG are therefore desirable for lossless imaging of THG. In a scanning microscopy approach, using a single condenser (e.g., an aspherical lens) lens made of UV-compatible glass is sufficient, given that preserving the image quality is not required. For imaging, this approach is not acceptable, as strong aberrations would be present. To overcome this problem, we designed a custom-made objective lens out of off-the-shelf components, able to image THG with little aberration. As it needs to operate only at 343 nm, its design is much simpler than one for an achromat, as there is no need for dispersion correction, and only UV-compatible glass is needed. For experimental convenience, the objective lens should be infinity corrected.⁴

We use a three-lens design, so that the system is both infinity-corrected and has minimal aberrations. Figure III.4 shows the simulated and experimental characterisation of the custom objective lens. Test chart observation shows that the system's resolving power is higher than 228 cycles/mm⁵, and that the minimum achievable resolution is 0.97 $\mu\text{m}/\text{pixel}$. Simulations predict that the system resolves higher spatial frequencies, up to the diffraction limit at roughly 1400 cycles/mm. Appendix A.2 reports more details about the objective lens design.

²A flint glass has high dispersion, i.e., a low Abbe number $V < 50$. Conversely, a crown glass has low dispersion, with $V > 50$. Arrangements of both types allow achromat design, e.g., achromat doublets.

³The absorption coefficient is defined as in Beer-Lambert law, is calculated from the complex refractive index \underline{n} . It writes as $\alpha = 4\pi\Im(\underline{n})/\lambda$. $\Re(\underline{n}) = n$ refers to the conventional refractive index.

⁴An infinity-corrected optical system does not directly form an image after its exit pupil – all exiting beams at focus are parallel. This, despite the added complexity, allows adding filters without disturbing the wavefront, and hence the image, as well as changing the tube lens for prototyping.

⁵This value is experimental determined by observation of the smallest resolvable element in the test chart. Here, the smallest one of the chart is observable, i.e., group # 7, element # 6 – corresponding to a resolution of 228.1 cycles/mm. Line pairs density in USAF 1951 test charts are determined as such: $\text{Res} = 2^{\text{group} + (\text{element} - 1)/6}$.

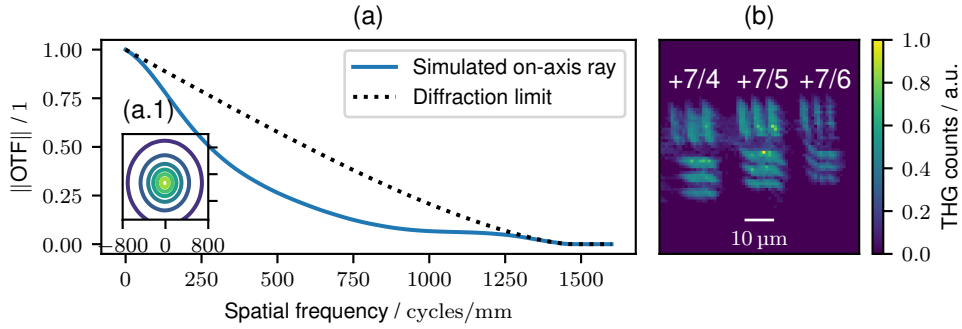


Figure III.4: Characterisation of our custom-made objective lens. (a) shows the simulated modulation transfer function of the optical system ($MTF \equiv \|OTF\|$, OTF being the complex optical transfer function), with the FFT method. The difference in values of the tangential and the sagittal axes are hardly discernible. The diffraction limit of the system, i.e., without aberrations, is plotted with a dotted line. The inset (a.1) shows the plotted simulated contours of the MTF on the image plane, highlighting the rotational symmetry of the system. (b) shows the acquired image of a negative 1951 USAF target (group #7, elements 4 to 6) imaged with the system, and exposed to 343 nm light. The smallest group on (b) is clearly visible, indicating a resolving power higher than 228 cycles/mm, confirmed by the simulation in (a). We can deduce that the resolution on the sensor is $0.97 \mu\text{m}/\text{pixel}$.

III.1.3 Sensing and data acquisition

As the collection lens is optimised for UV light collection, using this custom objective lens, let us now address the sensor used for acquisition. SHG and THG remain weak conversion processes. Consequently, special detection methods need to be used.

To fulfil this objective, we used a low-noise CMOS sensor developed at the Integrated Circuits Laboratory of Prof. Christian Enz at EPFL. This sensor is based on pinned photodiodes, and show a nominal peak noise of $0.34 e_{\text{RMS}}^-$. It shows a good quantum efficiency in the visible spectrum, down to UV, with $QE(\lambda = 343 \text{ nm}) \simeq 50\%$. Its ultra-low noise architecture allows photon counting over a 320×240 pixels image, at video rates up to 100 FPS, and at room temperature. [113] Sensor parameters are adjusted so that the full dynamic range of the sensor is used, i.e., to avoid over- or under- exposure. An FPGA device generates the control signals and allows data acquisition.

A custom-made Python library handles exposure experiments. The controller for the piezoelectric stages is controlled through USB. It can send trigger signals, which are used to synchronise emission with displacement of the stages. Another custom-made library handles communication with the FPGA, and data transfer. This allows exposure and measurement experiments to be performed in a single program, without user intervention.

In this section, we have discussed the integration of the full-field nonlinear microscope into a femtosecond laser processing platform. Particularly, we addressed the arrangements needed for those phenomena with low conversion rates, and collection of UV light. Let us now discuss observations carried out with this method.

III.2 Full-field THG detection of laser-affected zones

III.2.1 Scanning and full-field methods of THG imaging

Let us first compare THG fingerprints with scanning THG, which can both be achieved using the same experimental platform. Scanning mode is achieved by scanning the volume in which the modification lies and using the image sensor as a ‘single pixel’ detector, i.e., by summing the signal of all pixels. On the other hand, the full-field mode is here carried as focal-plane tomography: the full images are acquired by moving along the optical axis.

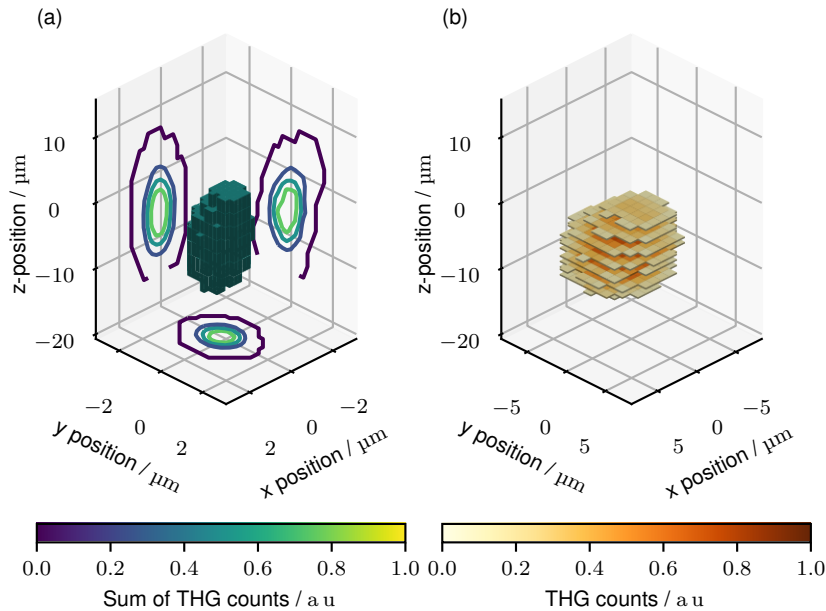


Figure III.5: Comparison between (a) 3D scanning THG versus (b) focal-plane, full-field THG tomography (b) of a laser-induced area, exposed at 9.72 J cm^{-2} with 14 pulses. (a) reports as a volume with voxels, with projections onto the three axes. (b) pictures stacked planes of full-field images, acquired, and plotted at the Z position relative to the inscription focal point. Note that (a) and (b) have different lateral scales.

Figure III.5 reports the results of these observations. Using the scanning mode, the expected ellipsoidal shape of the modification appears, with dimensions of roughly $2.5 \times 2.5 \times 15 \mu\text{m}$. [14, 91] With tomographic mode, this modification shows that the signal spreads much farther than what is expected, despite correct focusing, and as per measurements reported above, with a resolution of roughly $1 \mu\text{m}/\text{pixel}$. The emitted

Chapter III. Full-field nonlinear microscopy as a means for monitoring laser-induced modifications.

THG therefore *appears* as a much wider volume, with dimensions of about $6 \times 6 \times 10 \mu\text{m}$. In the sequel, we will address this difference in scale between both modes. The scanning mode reveals the contour of the laser-affected zones, while full-field images contain useful information with respect to the functional properties of laser-affected zones.

Let us now study the full-field response of several different modifications, exposed with different parameters. We consider an experimental matrix of exposed dots, separated by $3 \mu\text{m}$, so that the most exposure conditions can be inscribed in the $100 \times 100 \mu\text{m}$ range allowed by the stages, while avoiding crosstalk between neighbouring exposed areas. Processing pulse fluence ranges $F \in [3.9 \text{ to } 7.2 \text{ J cm}^{-2}]$, spaced linearly along the X-axis. Number of pulses ranges $n \in [1 \text{ to } 1 \times 10^5]$, geometrically spaced along the Y-axis. Once the modification is inscribed, the fingerprint is acquired. We use a probing pulse fluence of $F_p = 2.3 \text{ J cm}^{-2}$, a value high enough to trigger significant THG, while avoiding sensor saturation, and further damage to the affected area.⁶

Figure III.6(a) shows the THG scanning results, compared with (b) polarised light microscopy. Both show strongly different images: (a) shows a relatively smooth increase of birefringence as the overall exposure increases, (b) shows clearly identifiable regions. These regions show different THG fingerprints, with a selection of them reported in (c).

A first region appears, called Z1, for high fluence values $F > 7 \text{ J cm}^{-2}$ and few pulses $n \in [5 \text{ to } 50]$, that is not observable with polarised light microscopy. Full-field fingerprints of this region expand up to roughly $6 \mu\text{m}$ in width, and their 2D distribution is relatively smooth. A second region called Z2, highlighted by THG, exists for low fluence values $F < 7 \text{ J cm}^{-2}$ but with many pulses $n > 1 \times 10^3$. THG emission there is more minute than in Z1, and scattering of the fingerprints increases with fluence. A third region, Z3, for intense pulses $F > 9 \text{ J cm}^{-2}$ and many pulses $n > 100$ pulses, shows intense THG and strong scattering. This region appears with polarised light microscopy, as peak THG appears around $F = 10 \text{ J cm}^{-2}$ and $n = 500$. Between those regions, areas of lower THG appear, which we call ‘rifts’.

The presence of clearly separated regions indicates that different microstructures are present. The difference in THG fingerprints corroborate this explanation. Those structures show enhanced THG before overexposure (either in number of pulses or pulse energy) changes the structure, reducing THG efficiency. For extreme exposure parameters, i.e., region Z3, THG will appear in all cases, and those modifications are observable on polarised microscopes.

The smooth THG fingerprints in Z1 can be explained by the presence of sub-wavelength nanopores, see Figure III.7c, as the processing parameters are similar to what Sakakura *et al.*[38] have shown, i.e., type X. THG in Z2 could be explained by nanogratings, see Figure III.7a, as processing parameters lie in Regime II. If these areas are overexposed,

⁶In fused silica, our own observations show that $F_p < 3 \text{ J cm}^{-2}$ prevents further damage.

III.2 Full-field THG detection of laser-affected zones

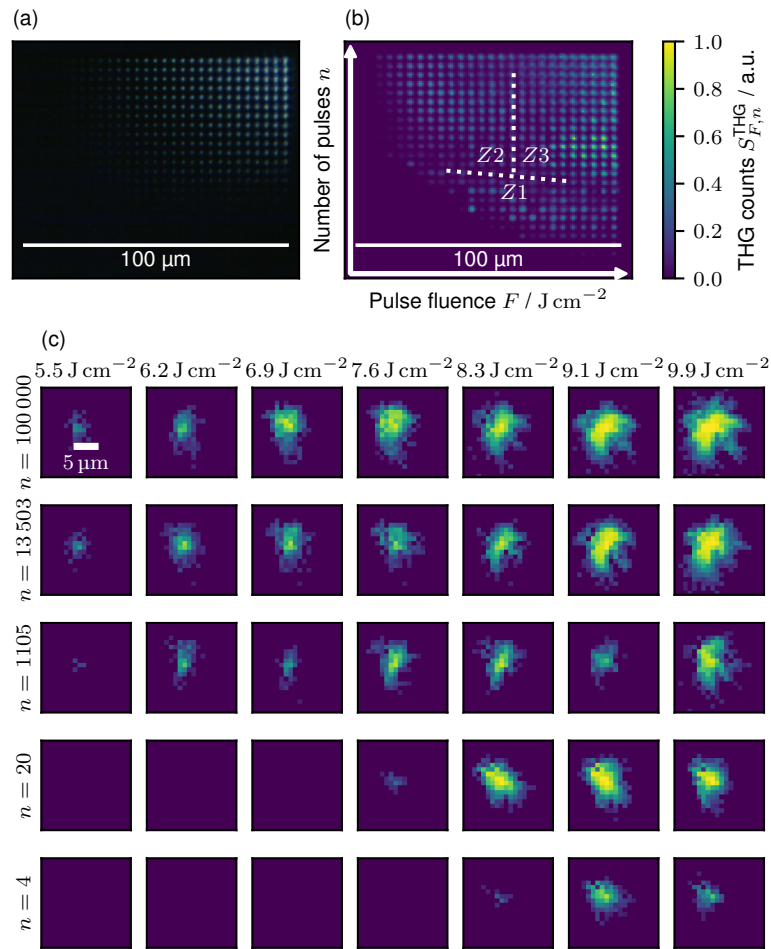
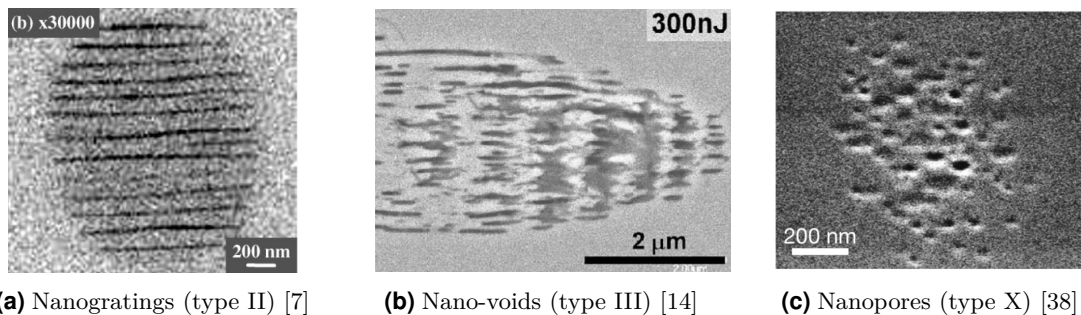


Figure III.6: Full-field THG detection of several laser-induced defects in fused silica, arranged in an $80 \times 70 \mu\text{m}$ -large experimental matrix, with varying pulse fluence (x-axis) and number of pulses (y-axis). (a) shows the polarised light microscope image of the experimental matrix. (b) shows the scanning THG image of the same matrix (scanning step of $0.5 \mu\text{m}$). (c) shows THG fingerprints of a selection of modified areas, with exposure conditions reported in the axes. The scale bar in (c) follows the calibrated resolution of $1 \text{ pixel}/\mu\text{m}$. All THG images are acquired on the inscription focal plane ($\Delta z = 0 \text{ mm}$).



(a) Nanogratings (type II) [7] **(b)** Nano-voids (type III) [14] **(c)** Nanopores (type X) [38]

Figure III.7: Scanning electron microscope images of a selection of femtosecond laser-induced modification in bulk fused silica.

Chapter III. Full-field nonlinear microscopy as a means for monitoring laser-induced modifications.

they lose optimal THG. Another interesting aspect of THG is the presence of a clear boundary between structures that enhance THG, and those that do not. We show that this boundary can be modelled with an incubation law later in §IV.3.

III.2.2 Third harmonic response of modifications to different probing polarisation states

So far, we have limited ourselves to a single input polarisation state. However, parametric processes, such as THG, strongly depend on polarisation states. Switching the probing polarisation relative to the inscription one is therefore of interest, as comparing these may yield information from the structures of the laser-affected zones. In the previous sections, we have only considered the case $\vec{E}_{\text{pump}} \parallel \vec{E}_{\text{probe}}$.⁷ Turning the half-wave plate by 45° after exposure allows to measure the case $\vec{E}_{\text{pump}} \perp \vec{E}_{\text{probe}}$. Adding a quarter-wave plate to the beam line turns the beam into a left- $\vec{E}_{\text{probe}} \odot$, or right-handed $\vec{E}_{\text{probe}} \ominus$ circularly polarised one. Note that no polariser is applied on the detector.

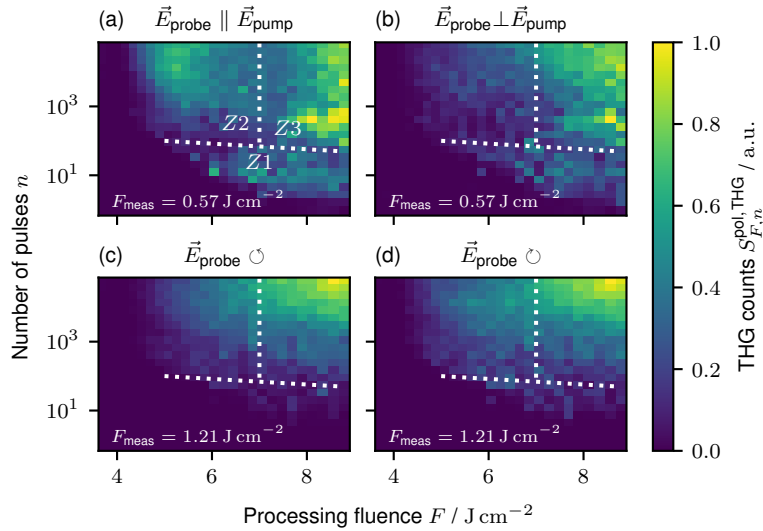


Figure III.8: Third-harmonic generation signal response of the laser-affected spots in fused silica, measured using different polarisation states. (a) shows the sum of THG signal for a parallel linear polarised probe, (b, c, d) for a perpendicular, a left-handed, and a right-handed probe, respectively. The probing fluence values are annotated at the bottom of each map. While linearly polarised light shows relatively similar region boundaries, although with different signal level depending on the orientation. Circularly polarised map shows very different patterns, more relatable to what is observed using polarised-light microscopy, cf. Figure III.6(a).

⁷We call ‘pump’ the processing beam, and ‘probe’ the THG-, SHG-, or MPF- generating one.

Figure III.8 reports signal maps at modification centres ⁸ for four different polarisation states, namely (a) parallel, (b) perpendicular, (c) left-, and (d) right-handed circular polarisation. Case (a) was the one considered in the previous subsection. Circular polarisation requires more pulse fluence to achieve satisfying contrast, therefore the probing value is adjusted, and Figure reports its values.

Comparing (a) and (b) highlights the disappearance of enhanced signal in Z2. Structures there are therefore likely to be strongly anisotropic. This corroborates the hypothesis that this area is associated with highly elongated nanogratings. We suggest that enhanced THG there may be caused by optimal interface arrangement compared to the probing polarisation. The background THG there and in the other cases is caused by fulfilling phase matching by the uniaxial nature of nanogratings. ⁹ These structures indeed behave optically as uniaxial crystals, through form birefringence, as mentioned in §I.4. The observable THG background, ramping in signal with increasing fluence, may be caused by the expansion of optical surfaces. Z1 appears equally in both linear polarisation cases. We associate this region with quasi-isotropic structures. However, strong variations from one point to the next may indicate the existence of a geometrical optimum for THG generation. Z3 also appears in both cases, with some variations. Extreme damage caused by laser irradiation there may enhance THG by both strong form birefringence, and the presence of multiple interfaces, see Figure III.7b.

Comparing (a-b) with (c-d) shows that the mechanisms leading to enhanced THG with a circularly polarised probe are different. The increase with both processing pulse fluence and number of pulses is linear, and no region can be identified as previously. Circularly polarised light induces THG exclusively where birefringence allows phase-matching, removing the contribution from the interfaces. [37, 89, 114] Note that both circular orientations maps are similar – we can therefore assume there is no chiral structure embedded in glass. [114]

Figure III.9 reports a selection of THG fingerprints of the same experiment as above. There, we see strong variations depending on probing polarisation.

⁸Signal maps are scanning THG images, i.e., where the sum of all pixels is considered. As data is collected instantly after exposure, immediate measurement is possible, and much faster than full range scanning, as in Figure III.6(b).

⁹Phase-matching is a condition for harmonics generation, related to the conservation of momentum. For THG, it writes: $\vec{k}_{3\omega} = 3\vec{k}_{\omega}$, with ω being the angular frequency of the incoming pulse. The coherence length, for which both fundamental and third-harmonic beams stay in phase, writes: $l_{\text{coh}} = \pi/\Delta k = \lambda/[6(n_{3\omega} - n_{\omega})]$. Assuming homogeneous fused silica, with $n_{\omega} = 1.45$, $n_{3\omega} = 1.4871$, $\lambda = 1030$ nm, we have $l_{\text{coh}} = 6$ μm , which is smaller than the feature size, and allows critical phase matching, hence strong THG enhancement. Because the refractive index varies with the wavelength, different arrangements of polarisation states may occur in uniaxial and biaxial crystals. Interfaces themselves locally allow phase matching, hence THG in other regions. The effective third-order dielectric tensor $\chi^{(3)}$ being a rank four tensor (four-wave mixing), accepts, in the case of THG, three polarisation states l, m, n as input, and one k as output. The difference in behaviour observed here between the input polarisation states highlight this effect.

Chapter III. Full-field nonlinear microscopy as a means for monitoring laser-induced modifications.

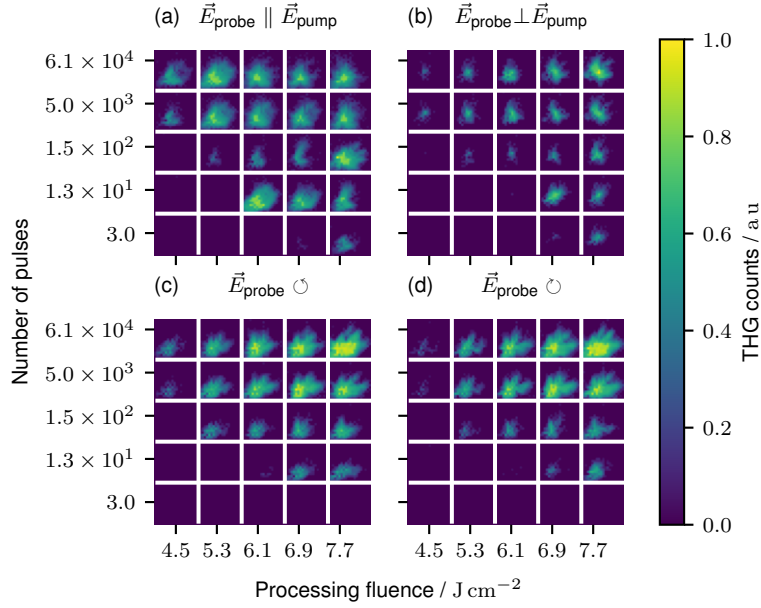


Figure III.9: Selection of THG fingerprints for the four different polarisation states considered. For each state, we report sixteen examples with selected processing fluence values and numbers of pulses. Note that, as previously, probing fluence for linearly (a, b), and circularly (c, d) polarised light is $F_p = 0.57$ and 1.21 J cm^{-2} , respectively.

First, we notice between (a) parallel and (b) perpendicular polarisation that THG fingerprints are relatively different, even in region Z1 that we identified as relatively similar in the case of scanning THG. The behaviour is otherwise generally the same, with region Z3 appearing in both cases, and Z2 lacking a peak in the second. Interestingly, shapes in (a) appear significantly wider than in (b), where they are more chaotically dispersed. For (c, d) circular polarisation states, THG fingerprints are similar one-to-another.

Considering the assumptions made above, we can explain the diffuse fingerprints in (a) for the most efficient THG in Z1 and Z2, as mostly resulting from optical interfaces. Outside of these regions, fingerprints are otherwise like (b-d). The more chaotic structures found in (b-d), that we associate with fulfilment of phase-matching, might be caused by the complex morphologies of laser-affected zones at scales smaller than the diffraction limit, resulting in complex scattering.

III.2.3 THG and wet etching selectivity

As THG seems to reveal different structures in the process maps, it comes naturally to test the associations made above between THG and morphology by investigating correlation with functional properties of the laser-affected zones. In particular, we observe

III.2 Full-field THG detection of laser-affected zones

that the behaviour of THG in laser-induced modifications, in the parameter space, is similar to a significant functional property: the accelerated wet etching rate. [115] To see the correlation between both properties, we inscribe lines of similar parameters to the experiment reported above.

To compare exposure conditions of dots, as reported above, against those of lines, as typically performed for wet etching studies, we associate the number of pulses n for a dot, with scanning speed v_s for a line. Assuming the beam size at focus w_0 , the equivalent linear pulse density writes $n_l = n/w_0$. From there, scanning speed can be deduced. It writes $v_s = \nu_p/n_l = \nu_p w_0/n$, with $\nu_p = 50$ kHz being the repetition rate.

2.5 cm-long lines of selected processing parameters are inscribed across a $25 \times 25 \times 0.25$ mm fused silica sample, using the platform presented in Chapter II. Then, we wire-cut the sample in three parts, perpendicularly to these lines. Two of them are etched and the last one is kept for archiving. Etching is then performed (see the caption of Figure III.10), and we measure the etched lines lengths with a bright-field optical microscope.

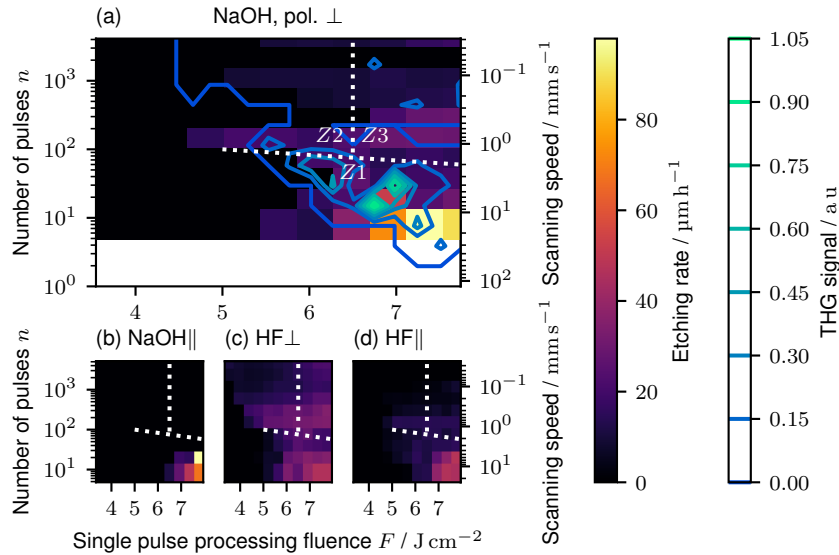


Figure III.10: Maps of wet-etching rates of laser-induced modified lines in fused silica, depending on etchant, polarisation state, and processing parameters. The etching processes are 3 h long and consist of 2.5 wt% HF at room temperature, and 5 wt% sodium hydroxide (NaOH) at 90 °C. Lines are written with perpendicular $\vec{E} \perp \vec{v}_{\text{scan}}$ or parallel $\vec{E} \parallel \vec{v}_{\text{scan}}$ linear polarisation. Contour lines printed over (a) show the corresponding THG signal data (see Figure III.6).

Figure III.10 reports the comparison between wet etching rates and THG signal over an area of processing parameters, for two different etching processes, and linear polarisation states. Both THG signal and etching rates, especially with caustic soda (NaOH), peak

Chapter III. Full-field nonlinear microscopy as a means for monitoring laser-induced modifications.

at approximately $F = 7 \text{ J cm}^{-2}$ and $n = 10$ pulses. A small offset between those peaks is visible. This may be caused by slightly different beam deliveries, and by the approximation that modifications have the size of the beam spot at focus.

The region previously identified as Z1 (bottom-right) shows a strong etching rate in both NaOH and hydrofluoric acid (HF), although less starkly so for the latter. In the case of a \perp polarisation, the overall area where etching occurred is similar to THG. For both cases with a \parallel polarisation, THG decreases immediately after this peak. Ochoa *et al.* reported polarisation independence of the etching rates in such regimes, [116] conflicting with observation of absence of selectivity with \parallel polarisation for NaOH. [27]

The region Z2 (top-left), identified as nanogratings, shows a HF-etching behaviour identical to what has been reported in literature, i.e., preferred etching with \perp polarisation. However, in the Z1 regime, etching becomes isotropic, as values become similar. Molecular defects are suspected agents in enhancing the etching rate in this region, as recently reported by Casamenti *et al.* [27] Enhanced etching in Z2 and Z3, mainly with HF with \perp polarisation, is suspected to emerge from nanogratings.¹⁰

There are however no known laser-induced modifications in fused silica showing resonance at 343 nm (3.6 eV), therefore we suspect THG-enhancement in Z1 emerges from pores.

To verify this assessment, we perform a 10 h-long annealing step at 300 °C on exposed specimens and compare them with scanning THG before and after annealing. The sample is set in an oven, heated up at a rate of 1 °C min^{-1} and cooled down after 10 h at a rate of -1 °C min^{-1} . Such a thermal process has been shown to remove all etching selectivity in fused silica. [27]¹¹

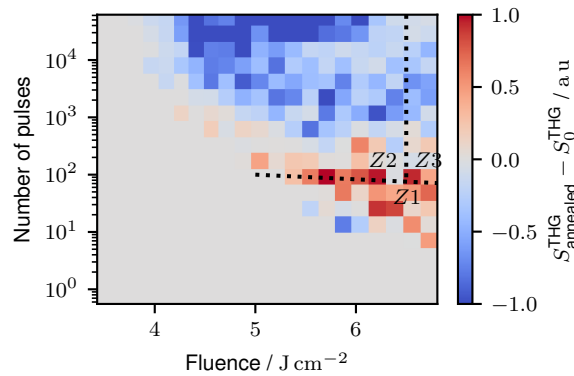


Figure III.11: Difference of THG signal of the experimental matrix on fused silica, before and after annealing. The sample has been annealed at 300 °C for 10 h.

¹⁰Nanogratings grow perpendicularly to the polarisation direction. HF is suspected to etch faster when percolating along their orientation.

¹¹Annealing is indeed known to quench molecular defects such as colour centres introduced by laser exposure in fused silica. [43]

Figure III.11 shows the difference in THG signal before and after annealing. We see that these values indeed vary – the intensity around Z1 increases, while it decreases around Z2.

Etching rate in Z1 is expected from the literature to collapse, indicating the origin of enhanced etching comes from molecular defects. Nonetheless, THG signal increases relatively to Z2 – therefore both quantities are not directly related *at all times*. Nonetheless, both defects and pores can indeed coexist, especially considering potential dissociation of the oxygen atoms, in a mechanism proposed by Sakakura *et al.* [38]¹² Nanopores emerge from molecular defects, during consecutive irradiation by ultrafast pulses. Furthermore, the wide yet smooth expansion of the THG fingerprints implies the presence of nanostructures, all smaller than the diffraction limit. We therefore hypothesise that THG and wet etching rate are two *correlated* quantities – related by the mechanisms of their formation, which may explain the slight shift between peak wet etching and peak THG, as in Figure III.10.

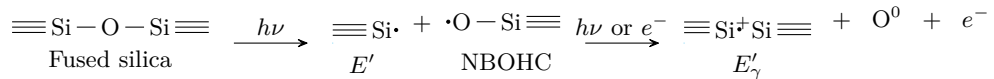
III.2.4 Tomography of laser-induced defects, and their evolution under irradiation

A significant advantage of nonlinear microscopy methods is that, like nonlinear absorption, the volume of interaction is tightly limited in all three dimensions. Therefore, we can perform focal-plane tomography of laser-affected areas along the optical axis. To this effect, we collect THG images by scanning over a range of $\pm 15 \mu\text{m}$ centred on the focal spot of the machining beam.

Figure III.12(a) reports examples of focal-plane tomography performed on four modified areas, exposed with four different pulse fluence $F \in [6.8 \text{ to } 13.2 \text{ J cm}^{-2}]$, and at six different exposure times, expressed in number of pulses $n \in [32 \text{ to } 1 \times 10^5]$. We write every image acquired at a given z position $S_{F,n}(x, y, z)$. Their values are normalised to the absolute maximum value measured $S_{\text{max}} = \max(S_{\forall(F,n)}^{\text{THG}}(x, y, z))$. 3D data is projected on the axes and plotted in contours, for which we write $S_{q_i, F, n}^{\text{THG}}(q_j, q_k) = \sum_{l \in (x, y, z), l \neq i} S_{F, n}^{\text{THG}}(x, y, z)$. (b) shows in full lines the plots of the sums of the 3D images as a function of the number of pulses n , written $S_{\text{tot}, F, n}^{\text{THG}} = \sum_{xyz} S_{F, n}^{\text{THG}}(x, y, z)$.

We notice that, for high fluence and few pulses (see image at $F = 10.9 \text{ J cm}^{-2}$, $n = 32$ pulses), the acquired THG volume is confined in a sphere of diameter approximately the width of the focal spot. As the pulses accumulate, this sphere enlarges

¹²The mechanism proposed by Sakakura *et al.* [38] is the following: a pulse generates NBOHCs and E' centres (see §I.3.1). After further multiphoton ionisation, or impact ionisation by neighbouring hot electrons generated during the avalanche, an oxygen atom dissociates:



Chapter III. Full-field nonlinear microscopy as a means for monitoring laser-induced modifications.

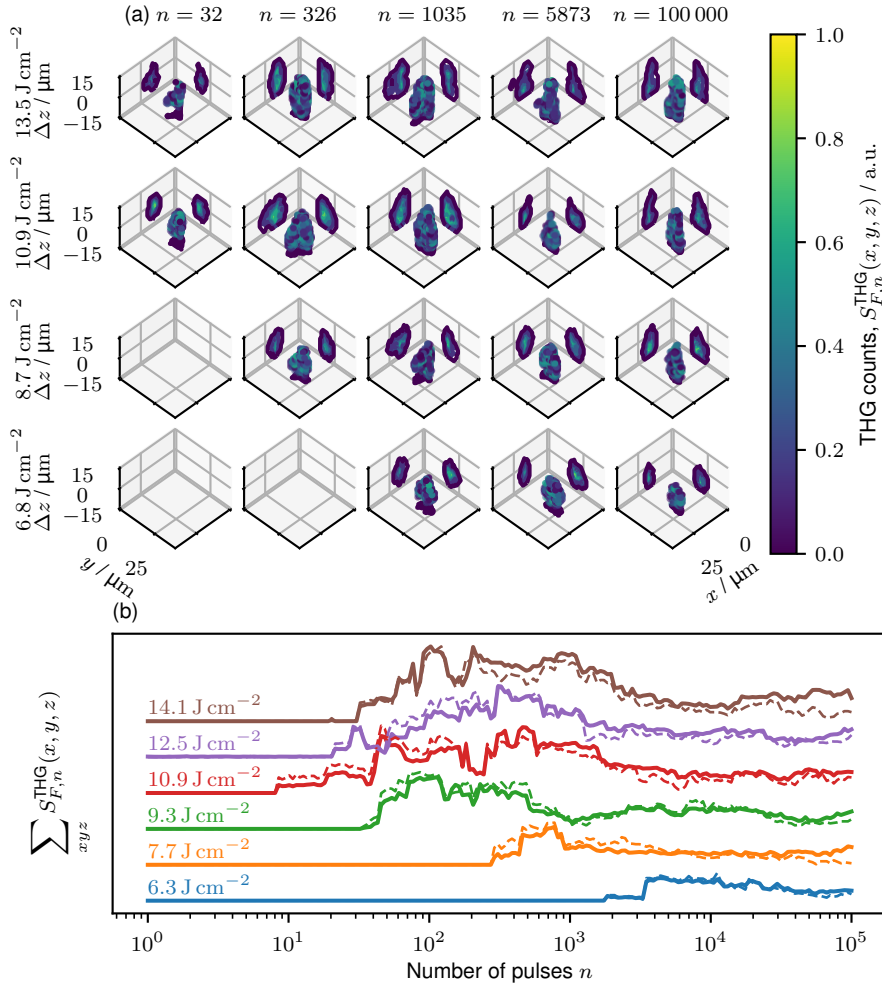


Figure III.12: Tomography of four different laser-induced modifications in fused silica (arranged vertically). LAZs inscribed with the same fluence are imaged between each irradiation period - essentially showing a timelapse (arranged horizontally) of the evolution of the same LAZ after a given exposure time. The probing fluence is $F_p = 0.5 \text{ J cm}^{-2}$. Four sets of 3D volumes at five different times are plotted in (a). (b) shows plots of the sums (along the three directions) of the signals for six sets. Thinner dashed lines represent the sum of the signals at $\Delta z = 0 \text{ } \mu\text{m}$, similarly to the scanning data, as reported previously. Note that the plain and dashed lines are not to scale with each other. The appearance of the modification at threshold is contained at first around the inscription focal point $\Delta z = 0 \text{ } \mu\text{m}$, then expands in all directions before travelling downwards.

(see $F = 10.9 \text{ J cm}^{-2}$, $n = 326$ pulses), then thins along \vec{e}_z (see $F = 10.9 \text{ J cm}^{-2}$, $n = 10 \times 10^5$ pulses), which matches the expected plume shaped behaviour. [117] Note that the centre of the LAZ travels towards negative Δz , i.e., towards the incoming beam. (b) shows this behaviour as well. Generally, signals appear with $n < 50$ pulses for $F > 9 \text{ J cm}^{-2}$. This threshold increases for lower fluence values, see Figure III.6(b), as further discussed in §IV.3.1. This occurs for both the overall sum and the sum at $\Delta z = 0 \text{ } \mu\text{m}$. Signal

III.3 Second-harmonic generation microscopy and multi-photon fluorescence microscopy

peaks, drops, and stabilises at a fixed value. The behaviour between experiments varies significantly, implying that the processes behind modification generation and growth may be of stochastic nature, as further discussed in §IV.3.2.

A plausible explanation to these observations is that, for high fluences, nanopores in the vicinity of the focal point appear. They behave as strong, localised THG emitters. As the number of pulses increase, these pores multiply and grow, specifically towards negative Δz , which induces scattering on the newly generated UV-light. The overall efficiency reduces as the structures coalesce into nanogratings. For low fluence values, modifications appear after a much higher number of pulses, and develop directly into the second step.

III.3 Second-harmonic generation microscopy and multi-photon fluorescence microscopy

Thanks to the nonlinear nature of the interaction, other modalities than THG are generated simultaneously with a single source. Here, two others are considered: second-harmonic generation (SHG), and multiphoton fluorescence (MPF).

To compare all three modalities, we inscribe an experimental matrix as pictured in §III.2.1. We first measure scanning THG as above. We then replace the imaging optics, namely the objective lens, and the fitting optical filter for the studied modality. The same experimental matrix is then probed, and data is collected. Note that in the case of MPF, the filter also allows SHG (centred at 515 nm) through, therefore the difference between both must be considered.

Figure III.13 reports all three modalities, with (a) separate heat maps and (b) stacked contour plots, for easier comparison. While THG exhibits the same behaviour as previously, SHG and MPF follow a much simpler behaviour at first glance. Both modalities increase with inscription fluence and number of pulses, albeit at slightly different rates. Indeed, they both notoriously exhibit a similar behaviour to the birefringence patterns, as in Figure III.6. Note that MPF has a non-negligible background, likely caused by ambient light, considering the allowed band by the optical filter, $\lambda_{BP} \in [400 \text{ to } 950 \text{ nm}]$.¹³

Increase in SHG is correlated to what we identified as Z3. SHG may arise there from local symmetry breakage caused by laser-induced E-field embedment, i.e., optical poling. This may be enhanced by phase matching through form birefringence. Such a property has been studied in doped glass to obtain extremely high SHG conversion. [83] In the case of fused silica processing, we do not foresee a significant advantage in using SHG compared

¹³Note that the Si-based sensor has a peak QE > 70 % for $\lambda \in [400 \text{ to } 600 \text{ nm}]$.

Chapter III. Full-field nonlinear microscopy as a means for monitoring laser-induced modifications.

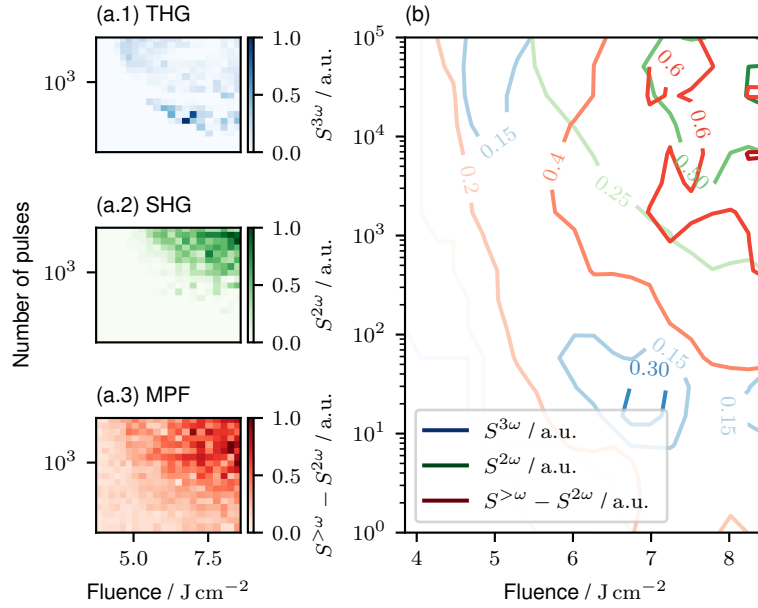


Figure III.13: Scanning nonlinear microscopy of different nonlinear microscopy processes on exposed points in bulk silica, as a function of the exposure parameters. (a) shows the raw output maps for, from top to bottom, second-harmonic generation (SHG, $S^{2\omega}$), third-harmonic generation (THG, $S^{3\omega}$), and multiphoton fluorescence (MPF, $S^{>\omega} - S^{2\omega}$, removing the SHG contribution). (b) shows the contour maps summarising the position of the main peaks for every method considered. Remarkably, only THG signal is strongest around $F = 6.5 \text{ J cm}^{-2}$ and $n = 10$. Both MPF and SHG increase with both fluence and number of pulses, although the former does so at a lower threshold.

to THG, as there is no specific advantage compared to birefringence measurement. Nonetheless, such a method can prove as robust as THG in the case of metal doped glass, or other dielectrics in which exposure leads to local poling.

Increase in MPF may be caused by laser-induced glass defects, as discussed in §I.3.1. Different contributions, mostly NBOHCs and ODC(II)s may be expected. However, the need to subtract the SHG signal from the overall visible light significantly decreases the contrast. No specific regions can be identified, except a slight increase with exposure dose. Hence in this case, the information carried by these modalities is limited.

Conclusion

In this chapter, we have addressed the ability to use full-field nonlinear microscopy for *in situ* characterisation of femtosecond laser-induced defects in fused silica. Most of the study performed here focuses on THG microscopy, as this modality provides rich information content on laser-affected zones. Other modalities may nonetheless be of value for other materials, where these are more sensitive, such as metal-doped glass. [83]

III.3 Second-harmonic generation microscopy and multi-photon fluorescence microscopy

In the specific case of THG, we have shown that full-field THG imaging provides rich information on the structures of sub-diffraction limit structures, in the form of complex THG full-field *fingerprints*. The origin of their surprisingly large size, compared to beam and structure size, is yet to be explored. A hypothesis regarding this characteristic stems from nonlinear scattering of the probing beam by the embedded structures. Their largest size w is significantly smaller than the probing wavelength: $\lambda/w < 10$, but can be relatively close to the third harmonic $\lambda/w \lesssim 3$. Given the stark refractive index contrast, and size of the structures, the Rayleigh-Gans-Debye approximation is not applicable.¹⁴ The chaotic shape of the THG fingerprints may arise from the emission of a strongly distorted THG wavefront, as each element acts as an independent emitter with a different phase. This would explain why the structures strongly perturb an otherwise diffraction-limited optical system and appear differently for different polarisation states. Porosity has been shown to increase harmonics generation, in both plasmonic and biological environments. [118–121]

This hypothesis could explain the elements demonstrated in this chapter. THG is sensitive to various types of modifications, therefore it is a tool to identify possible interaction regimes without *ex situ* measurements. One of such modifications, previously reported as Z1, show strong etching rate correlated with high THG signal. We showed that this correlation may be caused by pores, while defects are suspected to be the main driving force behind etching in Z1.

Finally, we demonstrate the ability of this method to resolve fast focal-plane tomography. Given the complex scattering medium, this method cannot directly resolve the actual shape of the modifications, but with fitting modelling and reconstruction algorithms, resolving the sub-diffraction limit shape of the medium may be resolvable.

¹⁴The Rayleigh-Gans-Debye approximation is widely used in nonlinear scattering, assuming little dephasing caused by the individual scattering elements. It formally writes $kd|n-1| \ll 1$, with $k = 2\pi/\lambda$ the incident light wavevector, d the linear dimension of the particle, and $n-1$ the relative complex refractive index of the particle in its medium. Here, assuming $d = 100$ nm, we have $kd|n-1| = 0.3$.

IV Demonstrations and applications

Contents of this chapter have been published in: O. Bernard and Y. Bellouard. ‘On the use of a digital twin to enhance femtosecond laser inscription of arbitrary phase patterns’. In: *Journal of Physics: Photonics* 3.3 (2021), p. 035003. ISSN: 2515-7647. DOI: 10.1088/2515-7647/abf743, and pre-printed in: O. Bernard, A. Kraxner, A. Boukhayma, C.ENZ, Y. Bellouard and J. Squier. *Third-harmonic generation monitoring of femtosecond laser-induced in-volume functional modifications*. preprint. 2023. DOI: 10.1364/opticaopen.22040459.v1

In the previous chapters, we have explored two different *in situ* monitoring methods. The first one, through phase imaging, allows direct observation of a functional value, the refractive index change. The second one, relies on observing the nonlinear reaction of modifications, at a significantly faster rate.

We demonstrated these methods as working principles. They can be adjusted to perform more intricate experiments and be applied to other substrates. This chapter presents a selection of such experiments. The first section suggests a pragmatic expansion of Chapter II, towards the inscription of large-scale arbitrary phase maps using raster scanning. The second section studies the usage of THG for observing modifications in substrates under varying conditions: direct-write lines, UV-exposure, and sub-surface modification in multilayered surfaces. The last one uses THG as a tool for reliability analysis: through several consecutive exposures, we use the increase in THG to study incubation effects in several glass.

IV.1 Inscription of phase maps

In Chapter II, we developed a digital-twin based method for inscribing direct-write phase maps in bulk fused silica. Thanks to displacement profiling of the scanning path, combined with heuristic modelling, we showed that this method is a step towards path-independent processing. Another interesting aspect is the high inscription resolution of the method, as shown in §II.3.3. In this part, we inscribe phase maps using raster scanning, which is particularly appealing for its simplicity and rapidity.

First, we consider the same pattern size as considered previously, i.e., $40 \times 40 \mu\text{m}$. We inscribe parallel lines separated by a pitch of $0.5 \mu\text{m}$, at a speed of $v_s = 100 \mu\text{m s}^{-1}$. With 120 samples acquired per line, the average spatial sampling period is about $0.4 \mu\text{m}$, which is about a third of the size of the modifications. At the ends of the lines, the effective sampling period is lower, as scanning accelerates or decelerates. This effect is hereby considered when performing model optimisation, to reduce overexposure at the pattern edges. We inscribe a selection of arbitrary phase patterns as examples. Note that other strategies exist to bypass issues related to acceleration and deceleration. One is to overscan the area, and to turn the laser on only when a certain cruising speed is reached.

Figure IV.1 shows a set of laser-inscribed patterns using raster scanning. The similarity between (b) input image, (c) measured phase, and (d) is remarkable, both in axial resolution and contrast. Inscription takes 1 min to complete.

$40 \times 40 \mu\text{m}$ -large patterns are too small for several potential applications. A trivial test case of this inscription method would be to increase the inscription size. Given the limited memory of the platform, sub- μm profiling is not achievable for displacements larger than $100 \mu\text{m}$. Therefore, for larger patterns, we assume this displacement to be negligible, as the acceleration area is inversely proportional to the overall area. We

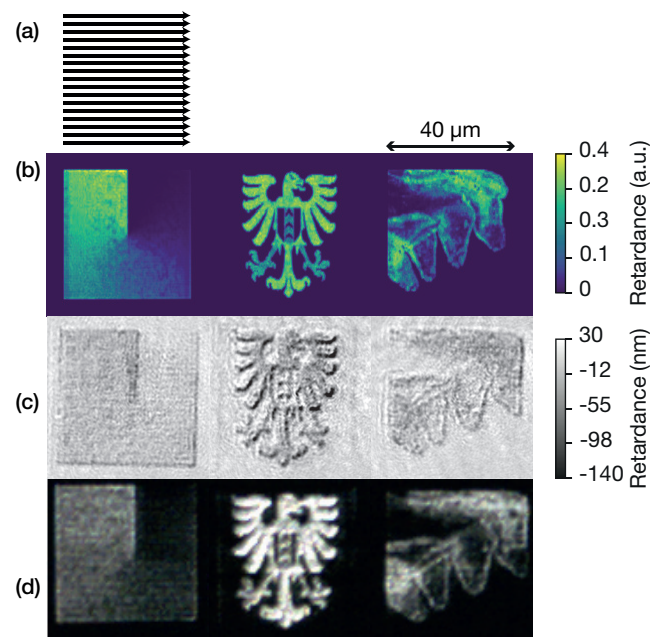


Figure IV.1: Patterns written with a (a) raster scanning strategy, (b) modelled output, (c) phase maps acquired by the DHM, (d) polarised-light microscope image (40x magnification, 0.75 NA). Input images, from left to right: first-order vortex phase-plate, seal of the city of Neuchâtel (Switzerland), reproduction of prehistoric painting of horses painted circa 30 000 BCE in the Chauvet cave, France.

therefore feed *predicted* positions to the model, with a pitch of $1\ \mu\text{m}$. As a demonstration of inscription of larger scale patterns, we use this method to inscribe a $5 \times 5\ \text{mm}$ -large pattern, considering a line pitch of $1\ \mu\text{m}$, and a speed of $2\ \text{mm s}^{-1}$, equating to a linear pulse density of $n_l = 50\ \mu\text{m}^{-1}$.

Figure IV.2 shows an example of a large-scale inscribed pattern. Such an inscription process takes approximately 4 h to complete. It shows that the inscription process is indeed upscalable.

This method relies on Type II modifications (nanogratings), which show strong form bi-refringence but non-negligible amplitude contributions as well, through mostly scattering. A further approach to improving this method would be to use Type X modifications, as shown by Sakakura *et al.*, [38] to inscribe large-scale, embedded in bulk glass refractive optical elements.

¹Image URL: https://commons.wikimedia.org/wiki/File:Ch%C3%A2teau_de_Neuch%C3%A2tel_en_automne.jpg

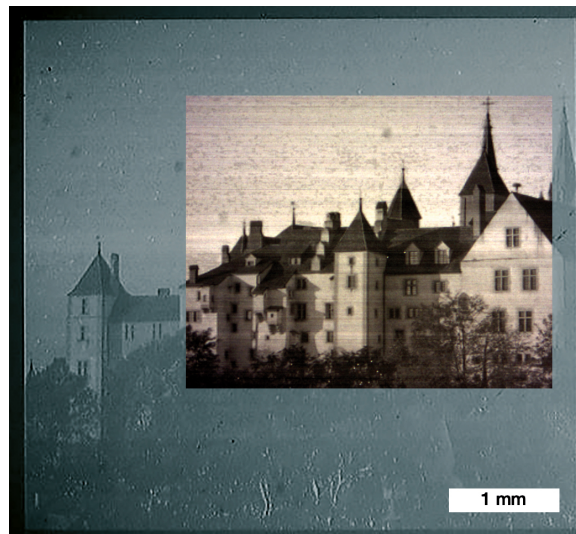


Figure IV.2: 5 mm-wide square pattern written using raster scanning. The wide image comes from a low magnification, dark-field digital microscope. The inset comes from a polarised-light microscope with trans-illumination, and 5x magnification. The input image comes from Martouf, CC0, via Wikimedia Commons.¹

Phase-contrast microscopy methods are useful to study large-scale structures, a property we took advantage of in this section, and in Chapter II. Let us now address using third-harmonic generation microscopy to probe matter more locally, as we have shown in Chapter III.

IV.2 Observation of laser-induced modifications in complex environments with THG: case studies

In Chapter III, we addressed the case of THG in the specific case of exposing *dots* in bulk. This approach allows to perform a significant number of experiments, and eases data interpretation. Yet, exposure experiments are typically carried out by scanning. There is therefore a strong interest in studying inscribed lines with THG. Another interesting case-study is the laser exposure of multilayered materials to achieve exotic material phases.

IV.2.1 Case study I: continuity of inscribed lines in bulk fused silica

We have shown that THG is well adapted for characterising exposed dots *in situ*. The question naturally arises as to whether it can do so in the more practical case of lines, and if it can resolve their structures.

IV.2 Observation of laser-induced modifications in complex environments with THG: case studies

To achieve this, we inscribe lines with varying exposure parameters. A first experiment (1) considers a fixed pulse fluence $F = 7.33 \text{ J cm}^{-2}$ and varying linear pulse density $n_l \in [2 \text{ to } 40 \text{ } \mu\text{m}^{-1}]$. The second (2) has a fixed linear pulse density $n_l = 2.00 \text{ } \mu\text{m}^{-1}$, and varying pulse fluence $F \in [7.4 \text{ to } 10.7 \text{ J cm}^{-2}]$. Lines are $90 \text{ } \mu\text{m}$ -long, written consecutively crosswise, so that a $100 \times 100 \text{ } \mu\text{m}$ -square is filled. Once the lines are inscribed, full-field THG images are retrieved along the line with a step of $0.2 \text{ } \mu\text{m}$. This will allow to identify the nature of the modifications.

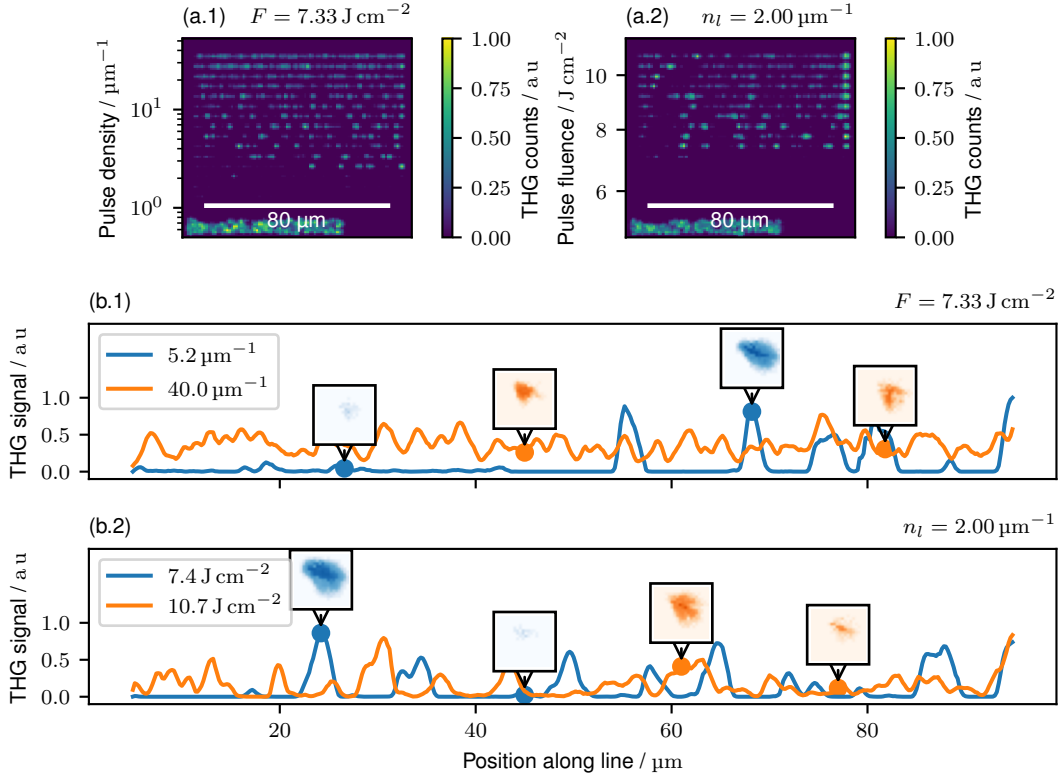


Figure IV.3: THG profile of laser-inscribed lines. Two experiments are shown, (1) with a fixed fluence and varying speed (i.e., pulse density n_l), and (2) with a fixed pulse density and varying fluence. (a.1, 2) show the scanning THG images. (b.1, 2) show the THG signal measured along selected lines, with insets of wide-field images at selected positions.

Figure IV.3 shows, for each experiment (1) and (2), the scanning THG images (a.1) and (a.2). We can already see that lines appear discontinuously, but notably less so for increasing pulse density, as in (a.1). Interestingly, fluence has, besides the threshold, little significant effect on line continuity.

Figure IV.3(b.1) and (b.2) report the THG signal along four selected lines in total. (b.1) highlights a remarkable feature: low pulse density lines show high contrast, widely separated hotspots. Some signal lower than 10% the maximum also appears at times. On the other hand, higher pulse density lines are more continuous, without hotspots.

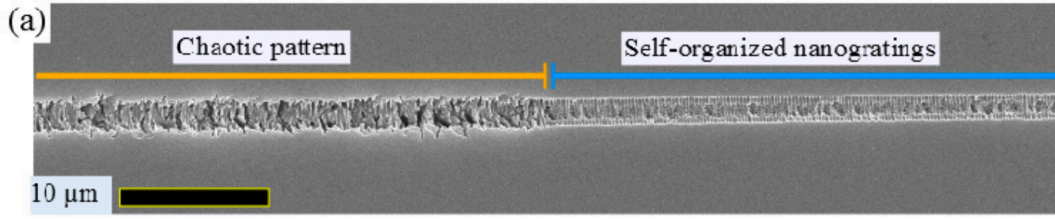


Figure IV.4: Scanning electron microscope image of an intermittent pattern, written on the surface of a fused silica specimen. Chaotic patterns appear between regions where self-organised nanogratings occur. Reprinted from Groothoff *et al.* [16]

Insets report a selection of THG fingerprints at their associated points. The highlighted hotspot in (b.1) at $n_l = 5.2 \mu\text{m}^{-1}$ (blue) has a smooth yet large fingerprint. Others points at $n_l = 40.0 \mu\text{m}^{-1}$ (orange) appear more chaotic.

Interestingly, in (b.2), the lower fluence $F = 7.4 \text{ J cm}^{-2}$ shows some hot spots, with one reported as having a similar shape as the one reported in (b.1). The higher fluence $F = 10.7 \text{ J cm}^{-2}$ shows more hot spots, albeit less contrasted so. Their THG fingerprints appear more chaotic.

These observations imply that the inscription process is stochastic. Literature reports such observations for surface exposure, [16, 17] as illustrated in Figure IV.4. Lines become more continuous with increasing pulse density, and does so also with fluence, although less significantly so. We assume that the *event* leading to such THG enhancement is associated to a random variable, itself depending on F : X_F . One can therefore write its probability $P(X_F)$. With this understanding, increasing line density is associated with a higher number of experiments, while fluence increases the probability of triggering an event. We see that, for $F = 7.33 \text{ J cm}^{-2}$, continuous modification is reached with $n_l > 20 \mu\text{m}^{-1}$. Trivially, we can assume that this probability is worth $P(X_F) = 2\%$, assuming a beam size of $2.5 \mu\text{m}$. Fracture stress in glass is probabilistic, as it emerges from random flaws in the specimen. Its behaviour typically follows the Weibull distribution [122, p. 192].² We will discuss a probabilistic analysis of low-enhancing THG in §IV.3.

Correlating this result with the etching experiments carried yields a valuable hindsight: etching rates, especially in the case of NaOH, peak at $F = 7.5 \text{ J cm}^{-2}$ and $n = 10$ pulses. We suspect that efficient etching is correlated with *line continuity*, and hence to a level of percolation, as visible with THG. Indeed, these modifications were thought to be defect-driven, as selective etching vanishes after low-temperature annealing, [27] while THG does not, as per §III.2.3. Nonetheless, theory does not prevent both molecular

²The cumulative fracture probability, governed by the Weibull distribution, writes for a given stress σ : [122, p.192]

$$F(\sigma) = 1 - \exp(-(\sigma/\sigma_c)^m)$$

with σ_c being a characteristic stress value, and m the Weibull modulus.

defects and nanopores to appear concurrently during exposure, as even the latter may develop from the former. [38] Note that overexposure leads to reduced etching rates, which may be an indication that these two phenomena are coupled. It is interesting to notice that HF-etching is relatively sensitive in this regime as well, although etching with nanogratings ($n_l > 100 \mu\text{m}^{-1}$) is more frequently studied.

IV.2.2 Case study II: femtosecond UV processing: waveguides and pores

Femtosecond-laser processing allows to inscribe direct-write waveguides in fused silica. [4] This process is however highly pulse duration-sensitive, [14] and difficult to obtain using the inscription setup presented in Chapter III. The spectral bandwidth sets the lower boundary for the pulse duration – reducing it further requires spectral broadening, which is experimentally difficult to achieve. Nonetheless, frequency-doubling the same pulses has been shown to increase reliability of waveguides inscription. [123] Given the increasing performance of laser amplifiers, harmonics can be efficiently generated. Here, we are interested in processing with frequency-tripled beams, i.e., UV pulses.³

When writing with UV, local THG enhancement of an already tripled beam would reach a ninth harmonic of 114 nm, that cannot be detected by conventional means. In this experiment, exposure is performed using a high-power femtosecond laser amplifier (Tangor 100, Amplitude Systèmes SA), frequency-tripled with a 30 W maximum output power at 343 nm, and $\tau_p = 500$ fs. THG observations are performed using the same setup as the preceding subsection. The frequency-tripled beam is focused using a Cassegrain-type, infinite conjugate, UV-coated reflector objective (10X/0.22NA, ReflXTM Edmund Optics, Ltd). We approximate the beam size as being $w_0 = 1.6 \mu\text{m}$. The pulse energy is fixed at $E_p = 200$ nJ, therefore pulse fluence is $F \simeq 10.5 \text{ J cm}^{-2}$. The pulse repetition rate is fixed at $\nu_p = 200$ kHz, and scanning speed v_s varies geometrically from 50 to 10 mm s^{-1} : linear pulse density $n_l = \nu_p/v_s$ therefore varies from 4 to 20 μm^{-1} .

Previous experiments showed that in such exposure conditions, direct-write waveguides appear for low linear pulse densities $n_l < 4.5 \mu\text{m}^{-1}$, and porous modifications appear with more. [124] An efficient wet-etching regime has also been identified for UV processing. Waveguides, that in essence consist of increased refractive index, are known to be THG-enhancing. [91, 92, 96] Here, the sharp transition between waveguiding and porous regimes forms an interesting case study for full-field THG, as the origin of scattering can be identified.

³The process to achieve frequency-tripling is *fundamentally* THG. The means to achieve it are naturally very different. A pair of non-linear crystals, a doubler and a mixer are used. The first generates a second-harmonic beam, and the second generates a third-harmonic beam, through sum-frequency generation. Phase-matching conditions need to be fulfilled, by adjusting the input polarisation states, so that the conversion processes have optimal efficiency.

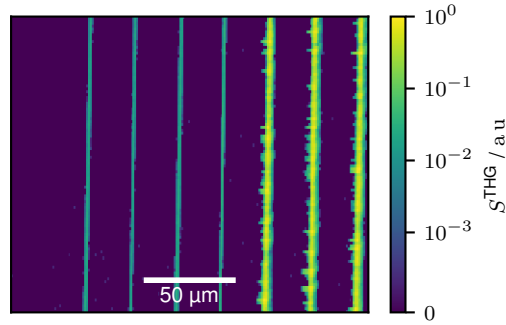


Figure IV.5: THG scanning image of waveguides (four leftmost lines), switching to porous, etcheable nanostructures (three rightmost lines), with increasing linear pulse density (i.e., decreasing speed, here going to the right). THG is significantly higher in the second case, highlighting the effect of optical interfaces for THG compared to smooth refractive index changes.

Figure IV.5 shows a scanning THG image of the region of interest: lines are inscribed vertically, and the pulse density increases gradually from the left to the right. The first four lines are low-loss waveguides, and appear as continuous, thin THG-enhancers. The further three lines appear as more diffuse, yet stronger THG-enhancers: they correspond to etcheable structures, without waveguiding capability. Scanning THG offers the capacity of observing such a transition, and potentially evaluating the quality of the nanogratings.

Figure IV.6 shows a stitched scanning THG image (a), scanned along five lines separated by circa $2\ \mu\text{m}$. This time, the associated THG fingerprints are reported in (b). Lines appear here horizontal, and their associated linear pulse densities are reported (increasing upwards). As previously, the same four waveguides appear as continuous modifications. Their full-field THG images appear thin and oblong. The other lines appear, as previously seen, more chaotic, suggesting the presence of scattering centres, as was discussed in §III.2.1.

The oblong, thin appearance of THG fingerprints of the waveguides for $n_l \leq 4.2\ \mu\text{m}^{-1}$ contrasts starkly with that of the porous modifications. These appear bound by a 6×2 pixels rectangle. Considering the beam size of $2.5\ \mu\text{m}$, and the calibrated system resolution of $\simeq 1$ pixel/ μm , we hypothesise that the width of the waveguides lies in a range from 1 to $2\ \mu\text{m}$. This range could be narrowed using higher magnification. The aspect ratio may be caused by the refractive index profile of the waveguiding, appearing as a cylindrical lens for the probe beam.

Porous modifications appear as highly diffused THG fingerprints, in contrast to the smoother, continuous waveguides. It is therefore possible to achieve single-shot quality assessment of the inscribed waveguides, as scattering centres are detrimental to their operation. Direct-write waveguide inscription, using UV femtosecond lasers, is potentially

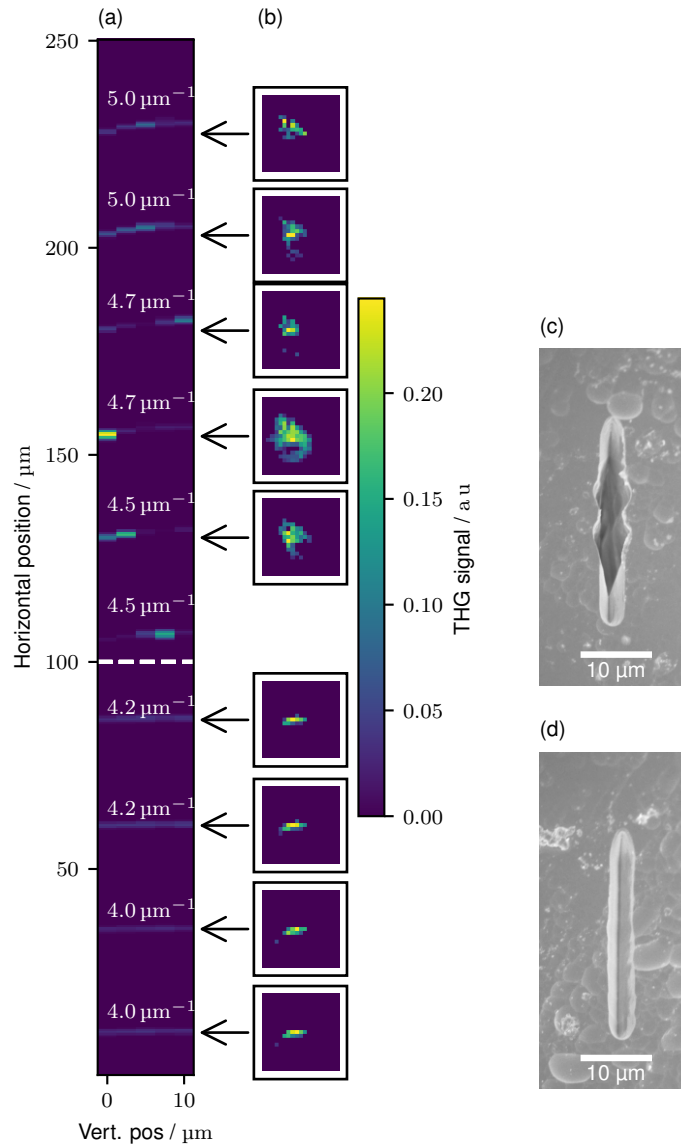


Figure IV.6: THG images acquired when travelling along a set of lines, with (a) inscribed with increasing pulse density (bottom to top, i.e., lowering speed). Insets (b) report associated THG fingerprints. Waveguides appear for low pulse densities, randomly turning into porous media, for $n_l > 4.2 \mu\text{m}^{-1}$. Scanning electron microscope images of cross sections are also reported, for (c) a porous line, and (d) a waveguide. Note that waveguides have a poor etching selectivity compared to pores. To enhance the visibility of the modified structures, the cut material has been polished, and etched for 4 h in 2.5 wt% HF at room temperature. For maximum contrast, the probing fluence is adapted depending on signal: the dashed white line at $100 \mu\text{m}$ indicates a change in value – below which is $F_p = 0.87 \text{ J cm}^{-2}$, and above $F_p = 0.3 \text{ J cm}^{-2}$. Lines were inscribed with UV femtosecond pulses at $F \simeq 10 \text{ J cm}^{-2}$.

interesting as exposure requires few pulses. However, a slight decrease of speed would generate porous modifications, preventing efficient guiding. This could notably happen when writing curved waveguides. Combining single-shot characterisation and a pulse-on-demand system⁴ could ensure high quality waveguide writing. However, this requires two independent femtosecond laser-lines, a UV one for processing, and one IR for probing.

Further comments regarding the generation of porous defects can be made from these observations. These pores appear above a certain pulse density threshold $n_{l,th} \in [4.2 \text{ to } 4.5 \mu\text{m}^{-1}]$ for $F \simeq 10.5 \text{ J cm}^{-2}$. Physically, it means that incoming pulses are mostly absorbed in already written, non-porous, waveguiding modifications. The material relaxes into a porous defect when above this threshold, and into a smooth waveguiding modification below it.

IV.2.3 Case study III: sub-surface exposure of multilayers

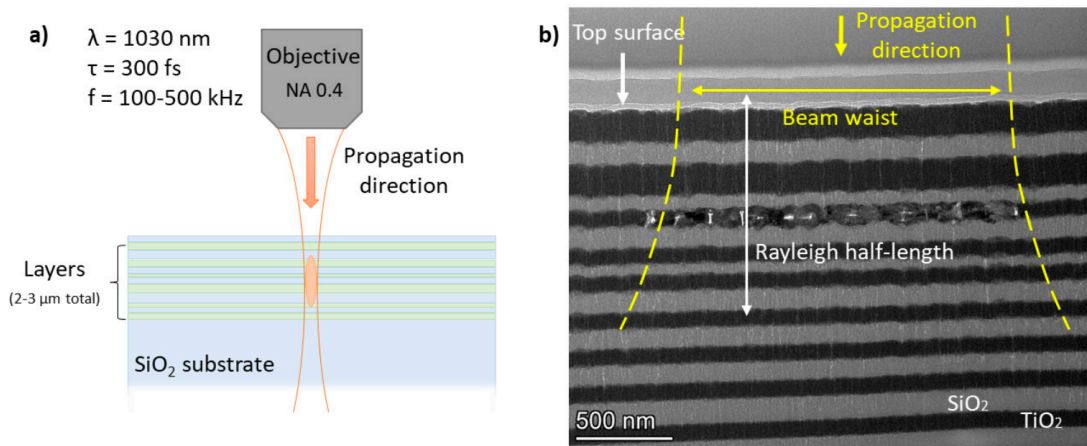


Figure IV.7: Principle of the ultrafast laser-exposure of multilayers. Constructive interference form in one of the layers that, under extreme field intensity, induce special types of modifications. An example thereof is (b) a crystallised layer of TiO_2 (rutile), as seen under bright-field transmission electron microscope. This appeared from the exposure of multilayers of amorphous SiO_2 and TiO_2 . Reprinted from Ricca and Bellouard. [126]

Ultrafast laser exposure of multilayered surfaces proves to be a promising path towards studying exotic material phases, given the extreme conditions attained, as illustrated by Figure IV.7. [127] By carefully designing these multilayers, a single layer can achieve an extremely high local field through N -wave constructive interference. The layered structures also act as *confinement* apparatus, keeping the laser-induced plasma from expanding in 3D. [127, 128] However, modifications confined in single layers are difficult

⁴A recent development in laser amplifier technology allows to vary the pulse-picker repetition rate with a fixed pulse energy. [125]

IV.2 Observation of laser-induced modifications in complex environments with THG: case studies

to observe or detect, as they are typically not observable under optical microscopy. As they do not affect the substrate topography, they are not readily visible in a scanning electron microscope, or any topographic method.

Tsang [84] showed in his first reported observation of surface enhanced THG, that layered dielectric surfaces may enhance or inhibit THG, depending on the layer structure. We hypothesise that a change of structure embedded in the multilayers, here caused by extreme laser irradiation, should be visible under THG.

In this case study, we expose a fused silica substrate coated with successive layers of both amorphous SiO_2 and TiO_2 .⁵ Dots are inscribed on a matrix, with pulse fluence varying linearly from 1.25 to 0.6 J cm^{-2} , along the x-axis. Because of the high sensitivity on the relative positioning between the focal plane and the substrate's surface, points are inscribed with varying z positions on the y-axis (called 'z-shift'). Dots are inscribed with 8 pulses.

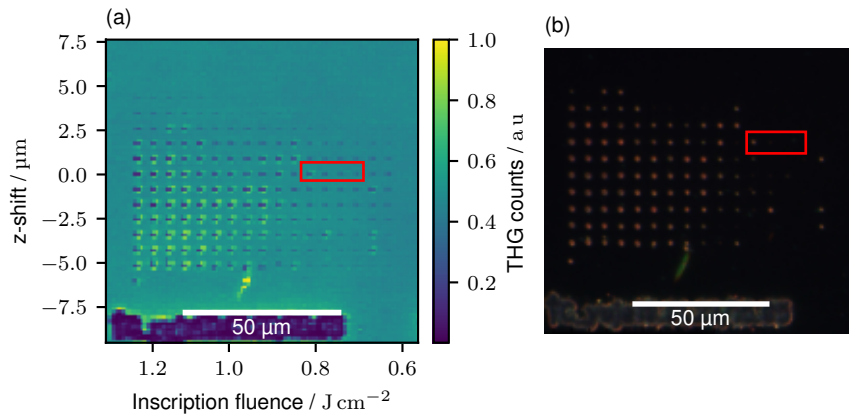


Figure IV.8: Dots machined with 8 pulses at the surface of $\text{SiO}_2 + \text{TiO}_2$ multilayers. (a) shows the THG image (captured at a z-shift of $0 \mu\text{m}$) of the experimental matrix inscribed. Inscription fluence varies along the x-axis, while exposure shifts in z relative to the surface, along the y-axis. The same matrix is shown under a dark-field digital microscope (b). THG highlights more affected microlayered areas than conventional microscopy. The red rectangles highlight the same area on both images – where machined dots appear with THG and do not with conventional microscopy.

Figure IV.8 reports both the scanning THG image (a), and a dark-field digital microscopy image (b) of the inscribed matrix. Similarly to what has been observed with THG in bulk fused silica, several more points appear in the THG image compared to conventional microscopy methods.

Here, most points which appear in both methods are ablated dots. With scanning THG, these points appear as craters: their centre has a dip in THG signal, surrounded by an annulus of generally increased signal. Under dark-field microscopy, these appear as dots

⁵The appendices in Ref. [128] report full characterisation of the multilayers.

in an otherwise black environment. Dots which appear only with THG have a lower signal relative to pristine zones. We suggest that these dots are modifications buried several layers deep into the material – the nature of which decreases the overall effectiveness of THG when probing the surface.

To investigate this nature, we selected a succession of dots in a row of the experimental matrix, to observe it with transmission electron microscopy (TEM). Namely, we chose the one highlighted by the red rectangle in Figure IV.8, corresponding to $\Delta z = 0 \mu\text{m}$ (i.e., focal plane on the surface of the sample), and $F \in [0.85 \text{ to } 0.7 \text{ J cm}^{-2}]$.

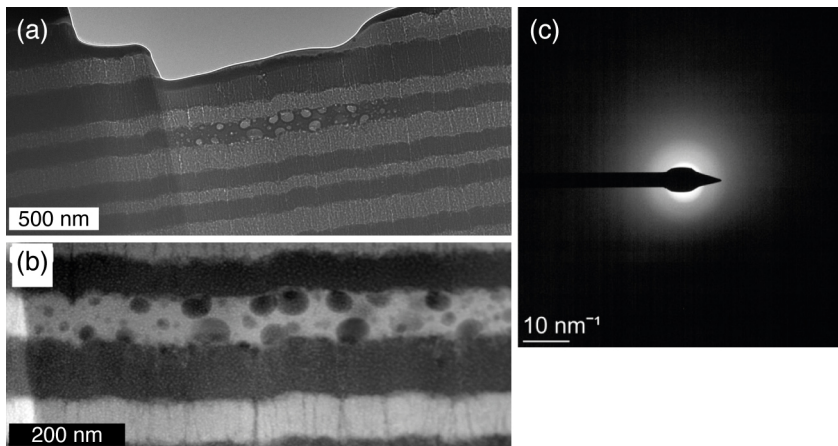


Figure IV.9: Electron microscopy of a machined dot invisible under conventional microscopy but observable under THG (see red rectangles in Figure IV.8). Nanostructures confined inside a single layer appear in (a) bright field transmission electron microscopy. (b) high-angle annular dark-field imaging reveals that these take the form of nanobubbles, with a foam-like morphology. The absence of (c) electron diffraction patterns confirms the absence of crystalline phases.

Figure IV.9 shows a lamella⁶ containing the second dot starting from the left (as pictured in the red rectangle on Figure IV.8(a)), visible under THG but not under dark-field microscopy. Bright-field TEM (a) shows that the modification is indeed bound by a single microlayer (here, the fifth). High-angle annular dark-field TEM (b) shows that the modification takes the shape of a foam-like structure, containing disordered pores whose diameters range 10 to 50 nm. Their diameters decrease with the distance from the centre. Electron diffractometry (c) confirms the absence of crystalline structures.

As a conclusion to this case study, THG is indeed capable of detecting modifications of non-crystalline nature buried below the surface of materials. This may prove a practical advancement for studying laser-induced sub-surface modifications in dielectric materials, as their position can be identified non-destructively, but also as a read-out method for subsurface encoded nanoscale information. An aspect to investigate would be the case

⁶TEM requires ultra-thin samples, so that electrons can travel through. After processing the sample, the sample was cut into a $\simeq 100 \text{ nm}$ -thin lamella, using focused-ion-beam direct-write lithography. Here, we used gallium ions.

of crystalline modifications. The latter may enhance SHG if their atomic structures were non-centrosymmetric, metal species crystallise, or photo-induced poling occur. Two-photon nonlinear scattering, a well-established method for characterising nanoparticles, may also occur.

IV.3 Modification threshold frontier modelling using THG experiments

As previously seen in §III.2.1, a clear border in the parameter space separates an area where modifications enhance THG from areas where they do not. This border is a *modification threshold*, that is deducible directly from such experiments. This threshold writes $F_{\text{th}}(N)$, i.e., the minimum number of pulses of a given fluence F needed to trigger an observable modification with THG.

This section will first cover the observation of the incubation law in the case of THG-observable defects in fused silica, followed by a reliability analysis of threshold measurements. Finally, we will investigate the incubation law in other glass types.

IV.3.1 Incubation law

This empirical rule states that, in the case of surface ablation, the threshold fluence F_{th} for several material groups can be related to the number of pulses N to the exponent of a free parameter, $S \in]0; 1[$, [129, 130] according to:

$$F_{\text{th}}(N) = F_{\infty} + (F_0 - F_{\infty})N^{S-1} \quad (\text{IV.1})$$

where F_0 , F_{∞} are the threshold fluence values for the first incoming pulse, and for an infinitely high number of pulses, respectively.

Here, we postulate that this empirical law also applies in the case of bulk modifications. To identify the parameters in Equation IV.1, we inscribe several laser-affected dots, for which we measure the THG signal after each pulse n . We discretise the parameter mapping in 27 processing fluence values F ranging from 6.5 to 9.8 J cm⁻². Each experimental data point is repeated 24 times, for statistical reliability, ($i \in \{0, 1, \dots, 23\}$). For every point, we obtain a list containing the sum of the signal over the whole sensor array $S_{F,i}[n] = \sum_{\forall x,y} s_{F,i}[n; x, y]$. Each element of the list corresponds to the THG signal probed after exposing with n accumulated pulses. If the signal reaches a detection threshold S_{th} after a given number of pulses $n < 100$, we define the experimental threshold number of pulses $n_{\text{th}}[F, i] = \min \{n \text{ if } S_{F,i}[n] > S_{\text{th}}\}$. This detection threshold

is determined based on the overall noise measured in the detector. If after 100 pulses the signal remains below this detection threshold, we consider that there is no modification. The data point is therefore skipped, and $n_{\text{th}}[F, i]$ is undefined (as $n_{\text{th}}[F, i] = \min(\emptyset)$).

For each fluence value, we can therefore determine a mean value $\overline{n_{\text{th}}}$, and a standard deviation $\sigma(n_{\text{th}})$. These values are fed into a Levenberg-Marquardt curve-fitting algorithm [107] with the incubation law defined in Equation IV.1, to identify the parameters F_{∞} , F_0 , and S .

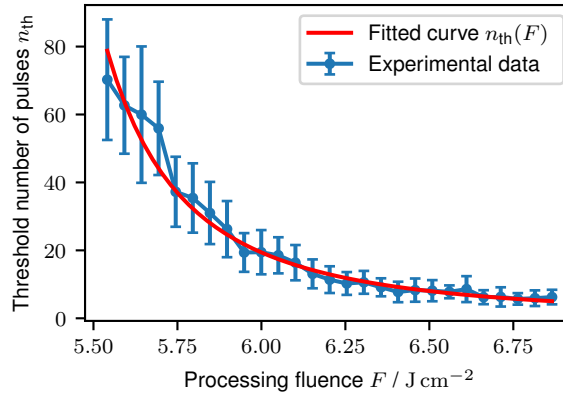


Figure IV.10: Measured threshold of laser-induced modifications with direct third-harmonic observation, and law of incubation. Blue points are the average experimental points $\overline{n_{\text{th}}}$, with their associated error bars $\sigma(n_{\text{th}})$ in blue. The data is fitted with the incubation law $F_{\text{th}}(N) = F_{\infty} + (F_0 - F_{\infty})N^{S-1}$, in red.

Figure IV.10 reports the results. The fitting algorithm returns the following parameters for fused silica: $F_0 = (5.1 \pm 0.1) \text{ J cm}^{-2}$, $F_{\infty} = (9.0 \pm 0.4) \text{ J cm}^{-2}$, $S = 0.51 \pm 0.07$. This empirical incubation law fits well with the measured THG threshold. As such, it can be used as a tool for predicting accurately the threshold for modifications occurring in the material, although this ansatz was developed for ablation studies. However, according to results previously reported for single-pulse exposure on fused silica surfaces, the fluence threshold for single pulse exposure at $\tau_p = 150 \text{ fs}$ and $\lambda = 1030 \text{ nm}$ is expected to reach $F \simeq 3 \text{ J cm}^{-2}$. [131] Our results are hence threefold higher. Given that we consider in-bulk exposure, such an increase is intuitive, as the boundary conditions differ from the surface ablation case: more energy is needed to ‘break-up’ the material.

Interestingly, standard deviation $\sigma(n_{\text{th}})$ decreases with high fluences, up until the point where any pulse of a given fluence systematically leads to modifications observable by THG. This observation highlights a relationship between THG and the occurrence of a physical phenomenon of statistical nature. Events of this kind could be for instance, crack formation (usually analysed with a Weibull distribution) or nano-bubble nucleation events (governed by an exponential growth according to Gibbs theory).

IV.3.2 Reliability analysis

Here, we perform a reliability analysis on the experimental values of threshold. We consider the values $n_{\text{th}}[F, i]$ as a random variable $X(F)$. Out of several types of distribution considered, the best fit is found for a log-logistic distribution [132]. Its probability density PDF $_X$ and cumulative density CDF $_X$ functions write as follows:

$$\text{PDF}_X(n_{\text{th}}; \lambda, k) = \frac{(k/\lambda)(n_{\text{th}}/\lambda)^{k-1}}{(1 + (n_{\text{th}}/\lambda)^k)^2} \quad (\text{IV.2})$$

$$\text{CDF}_X(n_{\text{th}}; \lambda, k) = \frac{1}{1 + (n_{\text{th}}/\lambda)^{-k}} \quad (\text{IV.3})$$

with $\lambda > 0$ and $k > 0$ being the shape and scale parameters of the distribution, respectively. There, we consider both parameters to be dependent of the fluence F .

To test the suitability of this law in this case, we conducted the same experiment as before. All values of $n_{\text{th}}[F, i]$ are arranged into a weighted cumulative histogram, then fitted to Equation IV.3, and plotted using a reliability analysis library. [133]

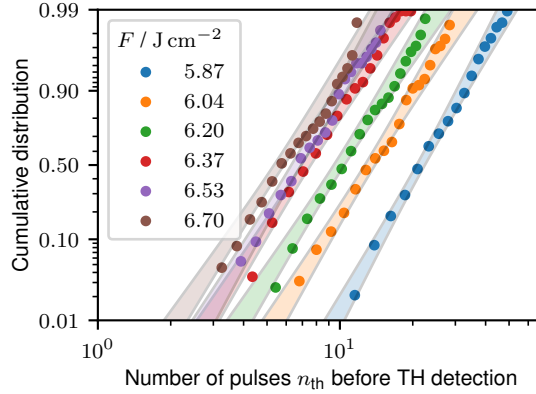


Figure IV.11: Log-logistic plot of the measured threshold values. Datasets, here differently coloured, are acquired using six different values of fluences ranging from 5.87 to 6.70 J cm $^{-2}$. Data is arranged in a cumulative histogram and the cumulative function of the log-logistic distribution is fitted. Dots report data points, and lines report the associated 95 % confidence range of the fitted distributions. Both axes are adjusted so that log-logistic distributions appear as lines.

Figure IV.11 reports the experimental cumulative distribution data, and the fitted log-logistic distribution $X(F)$. Table IV.1 reports the optimised distribution parameters, as well as the mean $E(X) \sim \bar{n}_{\text{th}}[F]$, the median $Q_{50\%}(X) \sim \text{median}(n_{\text{th}}[F])$, and the standard deviation $\sigma(X) \sim \sigma(n_{\text{th}}[F])$. While the shape parameter k is barely varying (reported values range from 4.7 to 5.6), the scale factor λ strongly varies negatively with pulse fluence. The quantile function of this distribution writes: $Q_p(X) =$

Chapter IV. Demonstrations and applications

$F / \text{J cm}^{-2}$	λ	k	$E(X)$	$\sigma(X)$	$Q_{50\%}(X)$	$Q_{99\%}(X)$
5.87	21.6(4)	5.6(3)	22.8	7.9	21.6	49.1
6.04	13.3(3)	5.1(3)	14.2	5.5	13.3	32.9
6.20	9.9(3)	4.9(3)	10.6	4.3	9.9	25.5
6.37	7.2(2)	4.9(3)	7.8	3.1	7.2	18.4
6.53	6.6(2)	5.2(3)	7.0	2.6	6.6	15.9
6.70	5.6(1)	4.7(2)	6.0	2.6	5.6	15.0

Table IV.1: Fitted parameters of the log-logistic distribution for the random variable $X(F)$, and the associated expected value $E(X)$, standard deviation $\sigma(X)$, median $Q_{50\%}(X)$, and 99 %-quantile $Q_{99\%}(X)$.

$\text{CDF}_X^{-1}(p; \lambda, k) = \lambda(p/(1-p))^{1/k}$. The median of the log-logistic distribution is therefore equal to its shape parameter $Q_{50\%}(X) = \lambda(F)$. We can therefore estimate the number of pulses needed for getting a 99 % chance to generate a defect $Q_{99\%}(X)$.

The log-logistic distribution used here has notably been developed and used as a more robust variation of the Weibull distribution, [134] especially in the case of censored data. [132] In our case, experiments terminate at 100 pulses, whether THG signal is detected or not. We deemed this choice optimal for our experimental setup, considering the time required to acquire data, and its statistical relevance. Statistically, the data is therefore right censored.

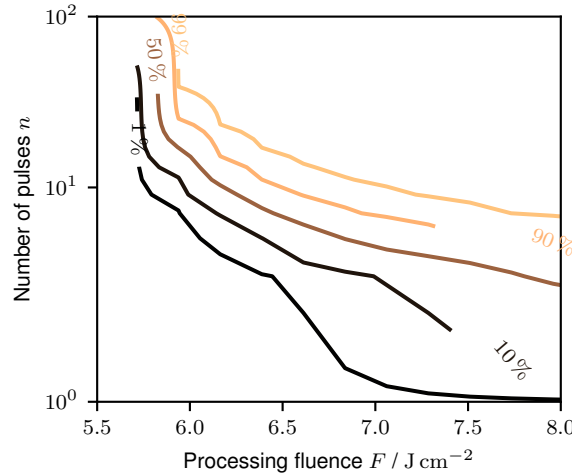


Figure IV.12: Contour map of the cumulative probability of generating a THG-enhancing modification in fused silica.

Using the cumulative density function, and by extrapolating the distribution parameters as functions of fluence, we calculate the cumulative probability to generate a modification, for a range of fluence values, as reported in Figure IV.12. ⁷

⁷We performed extrapolation by curve-fitting the values of λ to Equation IV.1, by substituting $\lambda(F) \Leftrightarrow n_{\text{th}}(F)$.

IV.3.3 Comparison between different types of transparent materials

The methodology presented earlier allows for a fast assessment of the behaviour of glass under exposure. As exposed in §III.2.1, THG can highlight different regimes of laser-induced modifications, and it can identify *in situ* the modification threshold as a function of the number of pulses, as shown above.

We generalise this method to other dielectrics. To this end, we perform the same study for three different common types of glass. To this effect, we replicate the experiment performed previously on different dielectrics types, to compare their behaviours. A selection of common dielectrics, with high scientific and industrial interest, is chosen, namely: sapphire, fused quartz (i.e., high purity silica glass, Heraeus Quarzglas GmbH & Co. KG Suprasil® 3002), and borosilicate float glass (Schott AG BOROFLOAT® 33).

Figure IV.13 reports the results for all three types of dielectrics. Each type exhibits strong variations in the THG map, and different regions composing them can be highlighted.

Strong boundaries between non-THG-enhancing and enhancing modification regions appear in all cases. Using the incubation law presented earlier, we can characterise the incubation parameters for each material.

To fit this law with our experimental results, we apply a count threshold on the sum of maps, and identify the points located at the border, plotted with white points on Figure IV.13. Numerically, we consider $S_t[F, n] = \text{sgn}(S_t[F, n])$.⁸ From there, we compute the numerical Laplacian $\hat{s}_t[F, n] = \nabla^2 s_t[F, n] = (\partial_F^2 + \partial_n^2)s_t[F, n]$. Only positions $[F, n]$ around the border come out as non-nought in $\hat{s}_t[F, n]$. White dots, in Figure IV.13, report these positions. The arguments of $\hat{s}_t[F, n] > 0$, \hat{F}_t and \hat{n}_t are then retrieved, and used to curve-fit the incubation law, reported as white lines.

Table IV.2 reports the fitted average parameters. Figure IV.13(a) shows the plots of the optimised functions with a solid white line. The minimisation algorithm used, trust region reflective, outputs the covariance matrix $\text{Var}(\mathbf{X})$, from which we deduce the standard deviation $\sigma_i = \sqrt{\text{Var}(\mathbf{X})_{ii}}$, with $\mathbf{X} = (F_0, F_\infty, S)$ being the vector containing the independent variables.

Sapphire shows a relatively flat THG signal: no strong variations appear across the parameter space, when looking at the sum of signals (a). Full-field images seem equally scattered, although they appear less so than what can be observed on other types of glass. Interestingly, THG does not unveil additional regions compared to conventional bright field microscopy. No modifications are observable using cross-polarised light, besides

⁸The sign function is here defined as such $\text{sgn} : x \geq 0 \mapsto \{0 \text{ if } x = 0; 1 \text{ otherwise}\}$.

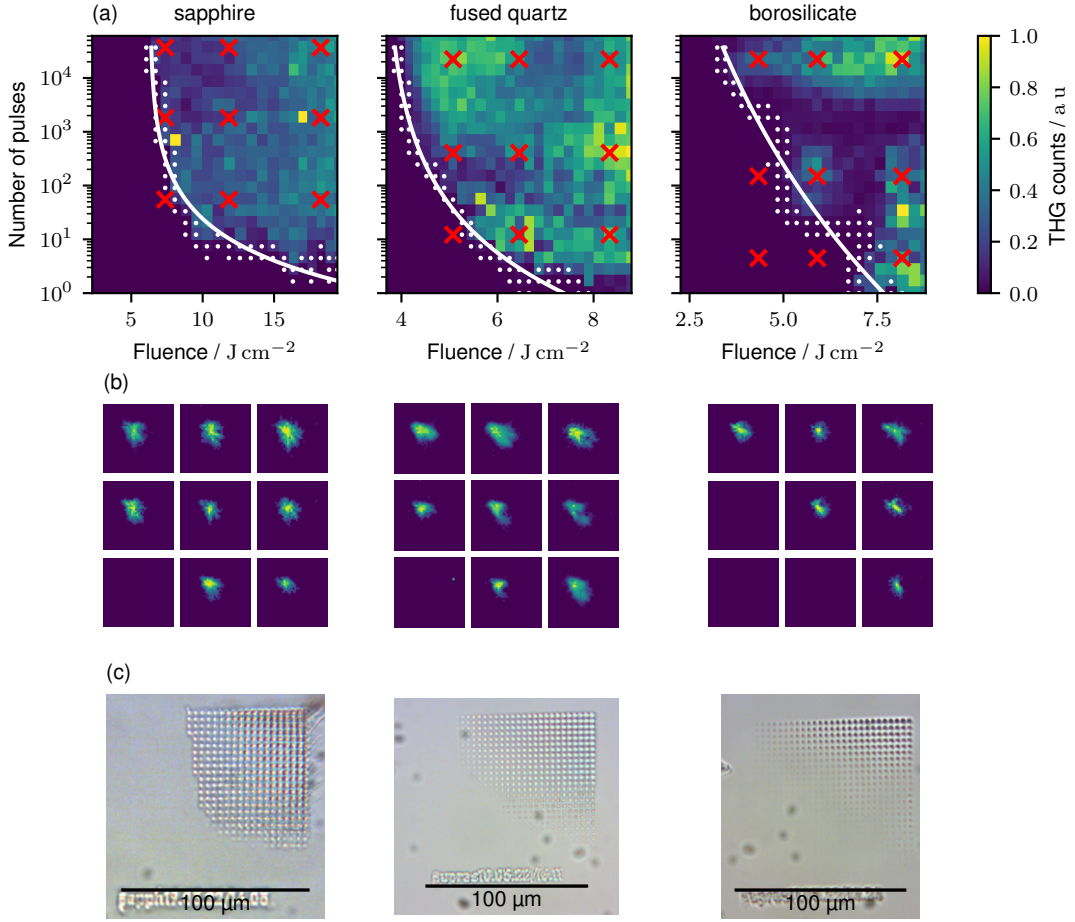


Figure IV.13: Comparison between different dielectrics (arranged from left to right): sapphire, quartz glass Suprasil® 3002, and floated borosilicate glass BOROFLOAT® 33. (a) shows the retrieved THG matrices, (b) a selection of wide-field THG images, and (c) bright-field images of the experimental matrices. Red crosses in (a) highlight the selected points on the matrix plotted in (b). Small white points in (a) indicate the measured threshold points, and the solid white curve indicate the fitting incubation law.

Glass type	$F_0/\text{J cm}^{-2}$	$F_\infty/\text{J cm}^{-2}$	$S/1$
fused silica Corning® 7980 0F	9.0(4)	5.1(1)	0.51(7)
quartz glass Suprasil® 3002	7.4(1)	3.6(2)	0.73(4)
borosilicate BOROFLOAT® 33	7.7(2)	0(3) [†]	0.92(3)
sapphire	23(1)	6.3(5)	0.42(7)

Table IV.2: Fitted values of the incubation law for different types of glass using *in situ* THG experiments, with corresponding standard deviations. †: the value reached the bounds of curve-fitting algorithm, set at 0 J cm^{-2} – given that the minimum fluence value tested for $n = 1 \times 10^5$ was 3 J cm^{-2} , the actual value is expected to be $F_\infty \in]0 \text{ to } 3 \text{ J cm}^{-2}$].

IV.3 Modification threshold frontier modelling using THG experiments

birefringence induced by photoelasticity in neighbouring regions. A region with slightly lower overall signal can be observed at $F \in [8 \text{ to } 12 \text{ J cm}^{-2}]$, $n > 100$ pulses. Note that the value of F_0 for sapphire is much higher than in the studied glass.

Fused quartz has a similar behaviour to fused silica, see Figure III.6, with less contrasted regions. The main difference between these two types of amorphous silicon dioxide is their OH-content: here 1 ppm, against 800 to 1000 ppm for fused silica. We can hypothesise that OH-defects slightly enhance the differentiation between different modification regimes.

Finally, borosilicate glass exhibits an analogous-yet-different behaviour compared to fused silica: wide rifts in THG signal clearly define regions, with widely different shapes compared to both types of fused silica. The first one, obtained by exposing with $F > 4 \text{ J cm}^{-2}$, $n > 1000$ pulses, shows strongly scattered images, and is visible by conventional microscopy. A second one, centred around $F \simeq 4 \text{ J cm}^{-2}$, $n \simeq 6$ pulses, not visible with conventional microscopy, shows little scattering. The third region appears for $F > 7.5 \text{ J cm}^{-2}$, $n < 1000$ pulses and is very similar to the latter.

With this study, we have shown that THG can be a valuable tool for studying *any* transparent material – interaction regions can be highlighted similarly to what has been shown with fused silica. THG also seems to confirm the poor variety of laser-induced defects in sapphire. The case of borosilicate is however remarkable, as these otherwise undetectable regions may prove to have significant functional properties, especially for such an economical and common glass.

Conclusion

In this chapter, we have explored how the methods presented in the two previous chapters can be implemented in practical cases. We have mainly considered two aspects here: (a) expanding these methods towards studying or improving manufacturing in a scanning context, and (b) highlighting the behaviour of modification growth under exposure.

We have first shown that the inscription method presented in Chapter II is expandable towards inscription of large waveplates using raster scanning. This method allows for fast computing and high throughput for inscribing large structures. Thanks to full-field THG microscopy, we demonstrated the stochastic nature behind the appearance of certain modifications and hypothesised that efficient etching emerges from continuous generation thereof, and vanishes with overexposure. In the context of UV-processing, we have also shown that full-field THG microscopy discriminates single-shot waveguides inscription regime from porous modifications. This observation allows to comment on the physical mechanisms behind the formation of porous modifications. We have also demonstrated that THG is sensitive to laser-induced modifications in multilayers, otherwise optically undetectable.

Chapter IV. Demonstrations and applications

Finally, we have expanded this study to show that THG is a suitable tool for detecting modification thresholds in a variety of substrates, but also the statistical nature thereof, performed with a reliability analysis. The ability to automatically detect modification thresholds is of industrial relevance as it allows for a machine to automatically tune its processing map for an arbitrary transparent substrate.

V Conclusion

In this thesis work, we have developed *in situ* methods to improve, characterise, and study bulk glass fabrication using femtosecond laser pulses. We believe that these tools have the potential of being used in the context of control, to enhance inscription quality and throughput, proving to be valuable scientific methods for further investigating laser-matter interactions, especially in the context of processing.

V.1 Summary of observations

Let us summarise in this section the main observations performed in this thesis work, for further discussion and outlooks.

Towards path-independent, sub-diffraction limit arbitrary retardance patterns.

In Chapter II, we showed that *in situ* digital holographic microscopy, although not a fast enough model to drive a feedback loop, provides sufficient throughput for a predictive model of the process. Specifically, it allows for a fast calculation of the predicted phase map, given an arbitrary scanning path. Through optimisation, an energy modulation signal is computed, so that an arbitrary phase map is experimentally inscribed. This method provides a path towards reducing quill effects in laser inscription, and a model for predicting and correcting beam anisotropy. It also allows inscribing sub-diffraction limit structures. We showed in §IV.1 that such an inscription mechanism can be expanded to several mm-wide structures.

Multiphoton microscopy as a tool for identifying nature of modifications.

In Chapter III we showed that the morphological structures of laser-induced defects in fused silica enhance nonlinear conversion processes, thanks to strong refractive index modulation at the nanoscale. In this context, polarisation-resolved third-harmonic generation (THG) microscopy allows to discriminate the nature of laser-induced modifications. In addition, we identified a strong correlation between the peak signal lying in region Z1 and the wet-etching rate, a result which has a strong application potential for optimising inscription for wet-etching fused silica. In §IV.3.3, we have shown that the method can be used for several types of dielectrics. Finally, in §IV.2.3, we showed that tightly localised defects in multi-layered surface enhance THG.

Single-shot method for modification characterisation, and focal-plane tomography.

High sensitivity allowed by new image sensing technologies allowed us to expand THG, an inefficient microscopy process, towards *full-field* imaging. We showed several variations of THG imprints, associated with different regimes of modifications in §III.2.1. In §IV.2.2, we illustrated the use of THG for differentiating waveguiding modifications that appear as quasi-diffraction limited structures, from porous modifications, appearing as strongly diffused THG fingerprints. We have finally shown fast THG focal-plane tomography in §III.2.4. By performing focal-plane tomography between successive bursts of pulses, we could observe the appearance and evolution of strongly scattering, spherical-like modifications towards plume-shaped ones, the expected shape of nanogratings.

Stochastic nature of the interaction, and thresholds thereof.

Finally, we highlighted the stochastic behaviour of the interaction. In §IV.2.1 we showed that lines appear with increasing continuity under THG as a function of linear pulse density, up to the value for which efficient etching is achieved. We hypothesised that efficient etching comes from the complete coverage of lines with modifications. This property vanishes with overexposure, and underexposure leads to incomplete lines. After demonstrating the validity of the incubation law for THG-enhancing bulk modifications, we performed a reliability analysis on the experimentally measured thresholds in §IV.3. We have shown that the probability to generate such a modification emerges from a log-logistic distribution, a distribution robust to censored data analogous to the Weibull distribution. This hints towards a correlation between their generation with fracture mechanics. We carried the study of the modification threshold to a study on other dielectrics, where we identified both that the law of incubation is valid.

V.2 Discussion and outlooks

Anomalous nonlinear scattering by porous materials

A striking result shown in this thesis is the shape of THG distribution on the imager, induced by nanopores and nanogratings. They appear as up to $6 \times 6 \mu\text{m}$ -wide images, while their shape has a maximum cross-section of $2 \times 2 \mu\text{m}$. As discussed in Chapter III, this discrepancy therefore comes from the *nature* of nonlinear laser-matter interactions in porous materials. We suggest that the overall dephasing caused by individual, nonlinearly scattering elements causes this effective *defocus*.

There is a lack of theory regarding such behaviour in scattering media. Nonetheless, the throughput of the experiment, combined with adaptive optics and computational methods, would shed light on the nonlinear interaction between ultrafast pulses, and complex

Chapter V. Conclusion

media. We foresee that such methods could hint towards more detailed knowledge of the irradiated structures. Such an approach would facilitate theoretical developments, and possibly expand THG towards characterising porous and structured materials, whose dimensions are smaller than the visible spectrum. ¹

On the appearance of pores, correlation with etching rate enhancement, and line continuity.

A significant demonstration is the correlation between THG signal and wet etching rate, particularly in the case of NaOH wet etching. Compared to literature, this result is surprising, as molecular defects are known to induce efficient etching, as it can be annealed at low temperatures $T < 300^\circ\text{C}$. The annealing experiment shown in §III.10 demonstrates that etcheable defects *do not cause* THG, yet are correlated. Interestingly, some laser-induced defects may, with sufficient exposure, cause local degassing of silicon dioxide, an accumulation of which may prove a fertile ground for growth of dioxygen-filled nanopores, themselves enhancing THG.

On using spectral activity for monitoring

As presented in §I.4, *in situ* observation of the spectral activity of laser-induced defects is possible. Photoluminescence measurements typically require a UV source as excitation source, which is difficult to implement in IR-exposure experiments. Defect-induced absorption measurements have the same problem for most defects. However, as shown by Beaudier *et al.*, implementing defect monitoring is much more convenient. [75] While Raman scattering is usually too inefficient to achieve in situ monitoring, ² implementing mid-IR spectroscopy for controlling defect formation is of interest. ³

On applications

A natural development of the first point addressed in the previous section is the inscription and characterisation of refractive or diffractive optical elements. This would allow inscribing beam shaping elements in fused silica, in space-tight environment, like in a compact packaged product, or where material selection is problematic, like in vacuum. Such an inscription method can be accelerated by using type X, or porous, modifica-

¹This project has been awarded a ‘Sinergia’ (# 213521, ‘DigiLight - Programmable Third-Harmonic Generation (THG) Microscopy Applied to Advanced Manufacturing’) grant by the Fonds national suisse.

²Stimulated Raman techniques, such as stimulated Raman spectroscopy (SRS), can improve sensitivity, although with more intricate optical setup and signal processing (e.g., lock-in amplifiers).

³Project ‘ClosedLoop-LM: Ultrafast Laser Closed-loop Manufacturing using mid-IR Spectroscopy’, funded by the Strategic Focus Area: Advanced Manufacturing of the ETH-Rat.

tions, which show high direct-write retardance with low scattering. Another possible development is data storage. Complex, data rich patterns observable using DHM can be inscribed and retrieved.

THG may be a valuable monitoring tool for the 3D manufacturing community itself. It will find its sensitivity to etching rate in the few pulses regime useful in detecting defects during fabrication, or even develop feedback systems that will maximise its signal, controlling particularly the linear pulse density, through speed modulation or pulse-on-demand. On one hand, the stochastic behaviour shown in this thesis may imply that pulse frequency modulation, coupled with THG measurement, could yield higher modification throughput for etching. On the other hand, the same method can monitor waveguide quality as presented in §IV.2.2, and possibly be able to control their formation, this time minimising porous-induced THG.

Implementing control

The objective of this thesis was to identify control methods for implementing feedback loops in ultrafast laser-exposure processes. As we showed in Chapter II, quantitative phase-contrast imaging typically requires too significant computational power to achieve active control – hence using it for feedforward control.

THG behaves in a complex manner, however, we identified a peak of THG signal corresponding to efficient etching in fused silica. This peak corresponds to a region where high process throughput occurs, thanks to the few pulses required. As we have seen in §IV.2.1, line continuity is essential to ensure percolation of the etchant. Setting a feedback loop where THG is maximised in this regime could allow to reach very high speeds and significantly decrease processing times. Requirements for such an experiment include: a second IR beam (similarly to a pump-probe), and a method to remove radiation emitted from the plasma (e.g., triggering electrics, or optical methods).

A Appendices

A.1 Interactions of ultrafast laser pulses in dielectric media

This section aims at providing a wide overlook on the physical fundamentals allowing bulk processing of dielectric materials. We will take advantage of this review to highlight the possible undermining perturbations, showcasing the need for control in this specific technique. Some fundamental aspects for the monitoring methods studied in this thesis will also be addressed, as they are concomitant with fundamental aspects of the laser-matter interaction. We will address the nature of femtosecond laser pulses, their propagation in transparent materials, and how they induce modifications.

A.1.1 On ultrashort laser pulses

The first element to consider is the *tool*: light, arranged in intense pulses. It is comprised of electromagnetic waves. In a vacuum, a single electromagnetic wave consists of local electric and magnetic fields, written \tilde{E} and \tilde{B} , respectively.¹ In linear approximation and in a vacuum, according to the classical laws of electrodynamics (Maxwell's equations), these contributions follow the general wave equation: $\square_c \tilde{f} = \frac{1}{c^2} \frac{\partial^2}{\partial t^2} \tilde{f} - \nabla^2 \tilde{f} = \vec{0}$ with c being the speed of light. Let us consider the case of an electric field wave, in planar propagation, which can here be simply written as a solution of the wave equation:

$$\tilde{E}(\vec{r}, t) = \vec{E}_0(\vec{r}) e^{i(\vec{k} \cdot \vec{r} - \omega t)} \quad (\text{A.1})$$

¹In this work, we use the notation with a tilde, e.g. \tilde{E} , to denote a vector field rapidly varying in time. Otherwise vector fields are denoted with an arrow, e.g. \vec{E}_0 .

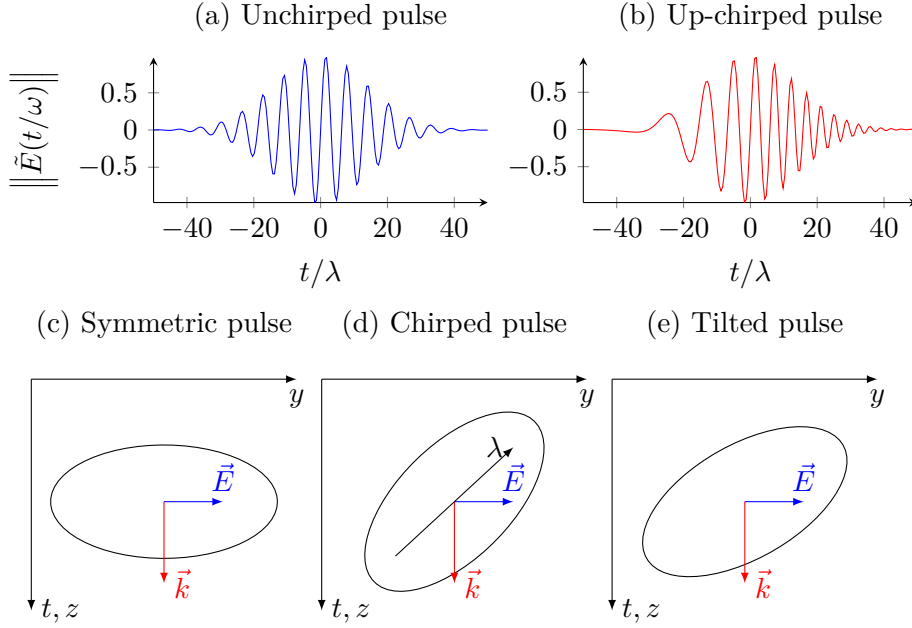


Figure A.1: Representation of several shapes of ultrafast pulses. (a) and (b) are the normed fields as a function of time for an unchirped and an up-chirped pulses, respectively. (c-d) are cuts in the y, z plane, with a symmetric (c), a up-chirped (d), and a pulse-front tilted (e) pulse.

with ω being the angular frequency, \vec{k} the wavevector, and parameters \vec{r} , and t , being the position vector and time, respectively. Both parameters are defined as $\omega = 2\pi c/\lambda$, and $\vec{k} = 2\pi/\lambda \vec{e}_k$, with λ being the wavelength, and \vec{e}_k the direction of propagation. $\vec{E}_0(\vec{r})$ is the envelope of the electric field, with the polarisation direction $\|\vec{E}_0\|$.

Considering now a *pulsed* wave, a simple way to write it is by applying a Gaussian envelope to Equation A.1. For simplicity, let us consider the case where $\vec{r} = \vec{0}$, we can write $\vec{E}(t) = \vec{E}_0 e^{-i\omega t} e^{-t^2/\tau_p^2}$, where τ_p is the pulse duration.

Ultrashort pulses can also be *chirped*, which means they can have a temporally varying instantaneous frequency. Increasing and decreasing frequency with respect to time is called up-, or down-chirp, respectively. In this more general, case the temporal envelope takes an imaginary part, which can be described as :

$$\vec{E}(t) = \vec{E}_0 e^{-i\omega t} e^{-t^2(1/\tau_p^2 + ib^2)} \quad (\text{A.2})$$

where b is a parameter so that πb is the linear variation of the instantaneous frequency $\nu(t) = \nu_0 + b/t$. $b > 0$ and $b < 0$ correspond to up- and down-chirp, respectively. Note that chirping is the basis for chirped-pulse amplification, [135] allowing to spread out the pulse's energy in time, to alleviate the intensity in the gain medium to prevent damage. Unwanted chirp can also appear with broadband pulses, in case of improperly aligned

A.1 Interactions of ultrafast laser pulses in dielectric media

compressor, or in general if dispersive optics, are present in the experimental setup. Pulse-front tilt may also happen, i.e. both spatial and temporal chirps are compensated, which makes a homogeneous pulse whose wavefront orientation is dependent on the wavelength. [65] Pulse-front tilt can emerge from the same source as chirping, and also in the presence of wedged optical surfaces. The effects of such asymmetries on the process is further discussed in §I.3.3.

Let us consider now that the beam is focused into an area A we assume to be circular $A = \pi w_0^2/4$, with w_0 being the beam waist diameter. Pulses occur periodically at a repetition rate ν_p , fixed by the user using a pulse picker.² We can easily measure the power of the beam P , averaged over a high number of pulses. The energy of a single pulse E_p can therefore be determined as $E_p = P/\nu_p$. A common quantity in laser processing, the pulse fluence F , is defined as the energy received by a surface per unit area for a single pulse, with $F = E_p/(\pi w_0^2/4)$ for a circular beam. Optical intensity I is defined as the pulse fluence over the exposure duration, which we can write as $I = F/\tau_p$. From this quantity we can estimate the amplitude of the electric field caused by the laser pulse :

$$\|\vec{E}_0\| = \sqrt{\frac{2I}{\epsilon_0 c}} \quad (\text{A.3})$$

with $\epsilon_0 \simeq 8.85 \text{ F m}^{-1}$ being the vacuum permittivity.

Now that we have discussed the formal definition of a laser pulse, and some physical aspects important when considering ultrashort pulses, let us now address the propagation of light in a transparent medium.

A.1.2 Nonlinear propagation of pulses in matter

Intense, ultrashort pulse lasers are indeed absorbed in the vicinity of the focal spot, in a material that is otherwise transparent to such radiation. This effect is caused by the nonlinear response of the material to intense exposure, allowing some photons to trigger local ionisation. Other wave mixing process explained by this theory occur concurrently, some of which will be used for performing monitoring. Let us discuss in this section how nonlinear optical theory in the context of this case study.

Propagation in bulk materials. An electric field $\tilde{E}(t)$ generates, in all cases, an electric displacement field $\tilde{D}(t)$, equivalent to charges flowing through a surface. In the case of travelling through a dielectric medium, light locally polarises surrounding matter. We can

²Laser oscillators have a fixed repetition rate, that can in some cases be finely tuned with a motorised stage. They have usually repetition rates too high for processing and often amplifying, hence the need for a pulse picker.

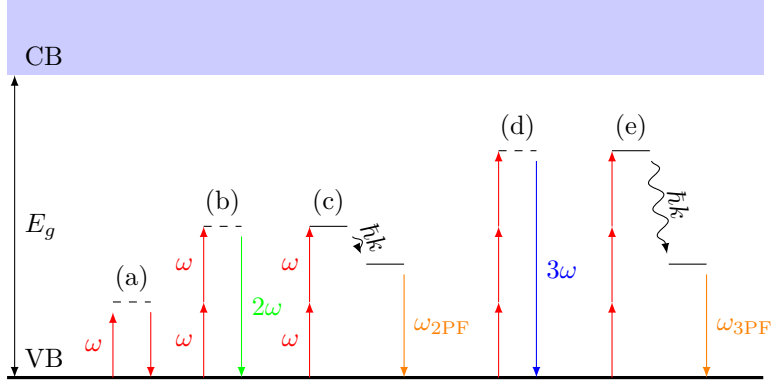


Figure A.2: Selection of single- and multi-photon processes. (a) is linear transmission. (b) is second-harmonic generation, and (c) is two-photon fluorescence, while (d) and (e) are third-harmonic generation and three-photon fluorescence, respectively. Arrows labelled $\hbar k$ represent non-radiative or low-energy radiative relaxation between two states. VB and CB represent the valence and conduction bands, respectively, and E_g the band gap.

define the light-induced dipole moment per unit volume $\tilde{P}(t)$. The electric displacement field is defined as such: $\tilde{D}(t) \equiv \epsilon_0 \tilde{E}(t) + \tilde{P}(t)$. In a linear, homogeneous, and isotropic material, polarisation is linearly related to the electric field: $\tilde{P}(t) = \epsilon_0 \chi \tilde{E}(t)$, with χ being the electric susceptibility of the material. We therefore have: $\tilde{D}(t) = \epsilon_0 (1 + \chi) \tilde{E}(t)$. In the case of linear, homogeneous but anisotropic materials (such as some crystals), this relation becomes more complex as electric susceptibility develops into a second-rank tensor $\chi^{(1)}$, we therefore write[55]:

$$\tilde{P}_k(t) = \sum_l \chi_{kl}^{(1)} \tilde{E}_l(t) \text{ with } \chi^{(1)} = \begin{pmatrix} \chi_{xx}, \chi_{xy}, \chi_{xz} \\ \chi_{yx}, \chi_{yy}, \chi_{yz} \\ \chi_{zx}, \chi_{zy}, \chi_{zz} \end{pmatrix} \quad (\text{A.4})$$

With high intensity lasers, nonlinear contributions become significant, and Equation A.4 can be generalised by a power series:

$$\tilde{P} = \epsilon_0 \sum_k \vec{q}_k \left(\sum_l \chi_{kl}^{(1)} \tilde{E}_l + \sum_{lm} \chi_{klm}^{(2)} \tilde{E}_l^* \tilde{E}_m + \sum_{lmn} \chi_{klmnp}^{(3)} \tilde{E}_l^* \tilde{E}_m \tilde{E}_n + \dots \right) \quad (\text{A.5})$$

with $\chi^{(i)}$ being the susceptibility tensor of the i -th order, of $i + 1$ -th-rank. While $\chi^{(1)}$ is dimension-less, the dimensions of the higher orders are the inverse of an electric field, to the power of $i - 1$ (m V^{-1} , $\text{m}^2 \text{V}^{-2}$, etc.). The increasing tensor order implies that processes are highly polarisation-dependent.

This behaviour allows for several frequency conversion processes. Second-order nonlinearity allows for second-harmonic generation (SHG), sum and difference frequency generation (SFG, DFG), parametric amplification, or the electro-optic effect, amongst other effects induced by *three-wave mixing*. Third-order nonlinearity allows for third-harmonic gen-

A.1 Interactions of ultrafast laser pulses in dielectric media

eration (THG), stimulated Brillouin and Rayleigh scattering, and coherent anti-Stokes scattering (CARS), amongst other *four-wave mixing* processes. These processes are notably enhanced by electronic resonance, allowing for multiphoton absorption.

In practice, values for nonlinear susceptibility are very low, and decrease exponentially with increasing orders, we will therefore only consider second- and third-order linearities in the context of this thesis. Even order susceptibility arises in the particular case of noncentrosymmetric media. Such materials range from α -quartz (d_{11}) to lithium niobate (d_{32}), with 0.3×10^{-12} to $-30 \times 10^{-12} \text{ m V}^{-1}$. Some mid-infrared glass show much higher values, such as $235 \times 10^{-12} \text{ m V}^{-1}$ (CdGeAs₂). Odd order susceptibility appear for all materials. Examples range from lithium fluoride to diamond, with $\chi_{1111} = 1.4 \times 10^{-22}$ to $21 \times 10^{-22} \text{ m}^2 \text{ V}^{-2}$, respectively.[136] These processes are therefore minute, they nonetheless become significant for high intensities, such as those allowed by ultrafast lasers.

Intensity-dependent refractive index. From the electric susceptibility, a significant dimensionless number in the field of optics is defined – refractive index $n_0 = \sqrt{1 + \chi^{(1)}}$. Given that, as we have seen beforehand, electric susceptibility is dependent on local optical intensity, refractive index is dependent as well. The intensity-dependent refractive index can be written

$$n = n_0 + n_2 I, \text{ with } n_2 = \frac{3}{4n_0^2 \epsilon_0 c} \chi^{(3)} \quad (\text{A.6})$$

with n_2 being the second-order index of refraction (unit $\text{cm}^2 \text{ W}^{-1}$). In the case of fused silica, we have $n_2 = 3.2 \times 10^{-16} \text{ cm}^2 \text{ W}^{-1}$. This effect implies that the pulse ‘sees’ a varying refractive index, depending on the local optical intensity, i.e. the closer to the optical axis, the higher n for $n_2 > 0$.

Under intense exposure with non-ionising radiation, matter reacts in a much more complex way than what predicted by linear electromagnetics. Several photons can indeed ‘merge’ to form higher-energy photons, however very inefficiently in bulk glass. This inefficiency however becomes significant under overwhelming exposure, sufficient to trigger ionisation. We will address the breakdown mechanisms in the following section.

A.1.3 Breakdown mechanisms

Several mechanisms causing material breakdown by non-ionising radiation exist, the prevalence of each being typically dependent on the optical intensity reached.

Appendix A. Appendices

Linear breakdown. Linear breakdown happens at high average powers but low intensities, where nonlinear optical effects are insignificant. This typically happens with continuous wave lasers, or long pulses $\tau_p > 1 \mu\text{s}$. This is caused by linear absorption of light. The little proportion of light being absorbed becomes overwhelming, and the material starts to heat up locally, until permanent change of material properties, or phase change occurs. This mechanism is not what happens with ultrashort pulses, as linear breakdown implies the presence of a wider heat-affected zone, and over the whole path of light inside the material, i.e. three-dimensional processing is not achievable this way. To achieve breakdown in the focal area only, the material needs to be locally ionised. Given that dielectrics exhibit a significant bandgap E_g , especially in the case of fused silica, where $E_g \simeq 9 \text{ eV}$, direct photoionisation could only be achieved with UV exposure, i.e. 138 nm for fused silica. Achieving photoionisation with longer wavelengths such as those of Yb-based lasers, i.e. 1.2 eV, relies on more complex processes.

Multiphoton ionisation. As discussed in §A.1.2, wave mixing can occur for the high pulse intensities allowed by ultrashort pulse lasers. Considering pulses containing photons of energy $E_{\text{ph}} = 1.2 \text{ eV}$ and a bandgap of $E_g = 9 \text{ eV}$, $N = \lceil E_g/E_{\text{ph}} \rceil = 8$ photons would need to be absorbed in order to overcome the band gap. Such a process is called multiphotonic ionisation.[137] The higher the value of N , the lower the probability of direct multiphotonic ionisation, in an exponential manner. It is important to note that dielectric materials usually have a non-nil amount of pre-existing defects in their bulk. These defects can induce virtual states in the gap, which enhance the probability of multiphotonic ionisation, through these virtual states which ‘split’ the process. Different grades of fused silica for instance, have a very similar bandgap but show very different probability of multiphotonic ionisation. [138]

Tunnelling ionisation, alias Keldysh mechanism. At higher intensities, strong electric fields can also induce a distortion of the band structure. Such a distortion can effectively lower the band gap, narrowing down the Coulomb potential well linking the atom with a valence electron. This facilitates quantum tunnelling of the electron into the conduction band. [139]

Adiabatic parameter, alias Keldysh parameter. Both types of mechanisms have the same output and occur for relatively similar optical intensities, with multiphotonic ionisation typically at $I < 1 \times 10^{13} \text{ W cm}^{-2}$ and tunnel ionisation at $I > 1 \times 10^{14} \text{ W cm}^{-2}$. Between those values, both mechanisms happen concurrently. The preponderance of one over the other is estimated using the Keldysh parameter:

$$\gamma = \frac{\omega}{e} \sqrt{\frac{\mu c n \epsilon_0 E_g}{2I}} \quad (\text{A.7})$$

A.1 Interactions of ultrafast laser pulses in dielectric media

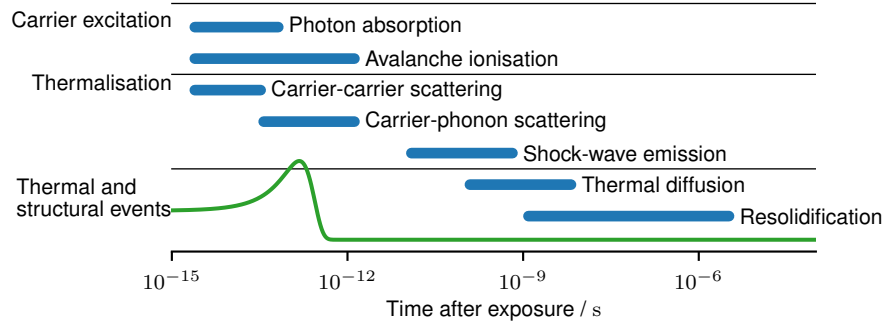


Figure A.3: Time-scales of the key mechanisms occurring during femtosecond laser exposure in dielectrics. The green line at the bottom represents the envelope of a typical femtosecond laser pulse, $\tau_p = 150$ fs. While excitation of the carriers occurs in the time frame of the actual laser exposure, i.e. about 1 ps, the thermalisation process takes up to 1 μ s. Reproduced from Gattass and Mazur. [140]

with μ being the electron-hole reduced effective mass $\mu = 0.64m_e = 5.82 \times 10^{-31}$ kg. $\gamma \gg 1$ implies that multiphoton ionisation is more significant than tunnel ionisation, and $\gamma \ll 1$ implies the opposite.

Avalanche breakdown. Once the first free electrons are created by the aforementioned photoionisation mechanisms, they are able to absorb the rest of the photons in the pulse through inverse Bremsstrahlung. This increases their energy, until the point they are able to excite other valence electrons into the conduction band. The increasing amount of electrons therefore increases absorbance by the free electrons cloud near the focal spot, further exponentially increasing their numbers in an avalanche phenomenon. This effect, called *avalanche breakdown* is significant for optical intensities ranging 1×10^9 to 1×10^{12} W cm $^{-2}$. The threshold intensity for avalanche breakdown writes [136]

$$I_{\text{th}} = n\epsilon_0 c \langle \tilde{E}^2 \rangle = 2n\epsilon_0 c \frac{E_g m_e}{f e^2 \tau T_p} \ln \left(\frac{N_{\text{th}}}{N_0} \right) \quad (\text{A.8})$$

Summary. Ultrafast laser pulses modify materials with three different mechanisms. The most significant ones, and unlike shorter-pulse lasers, are both multiphoton ionisation and tunnelling ionisation, which have very similar outcomes. In the regime we are studying, optical intensities are above the threshold for avalanche breakdown as well. Several studies showed that contributions to ionisation mostly comes from multiphoton ionisation.

Appendix A. Appendices

In this section, we have addressed the fundamental description of an ultrashort laser pulse, its propagation in matter, and the mechanisms through which they damage matter. Once the pulse has been absorbed, matter can resolidify in several ways, depending on several process parameters and the material itself. These modifications are the functional elements of the process.

A.2 Custom wide-field THG objective

For the purpose of this research on THG emission, a custom-made objective lens using off-the-shelf components was made. We hereby reproduce the parameters used, and the optimal components used for building up this lens assembly, as well as simulation results (Ansys, Inc., Zemax Opticstudio®).

Type	Comment	Radius	Thickness	Material	Coating
STANDARD		Infinity	2.0	SILICA	
STANDARD	SLSQ-15-20N	9.2	59.0		
STANDARD		Infinity	3.0	C79-80	EO_UVVIS
STANDARD	EO #84-300	-27.5	0		EO_UVVIS
STANDARD		Infinity	18.75		
EVENASPH	EO #33-956	11.46	4.36	C79-80	EO_MGF2(475NM)
STANDARD		Infinity	18.25		EO_UVVIS

Table A.1: Optics used in the lens design, Zemax Opticstudio® (Ansys, Inc.) table. Aspheric elements of sixth surface are omitted. The first surface is at the entrance pupil, and the last one at the exit.

A.2 Custom wide-field THG objective

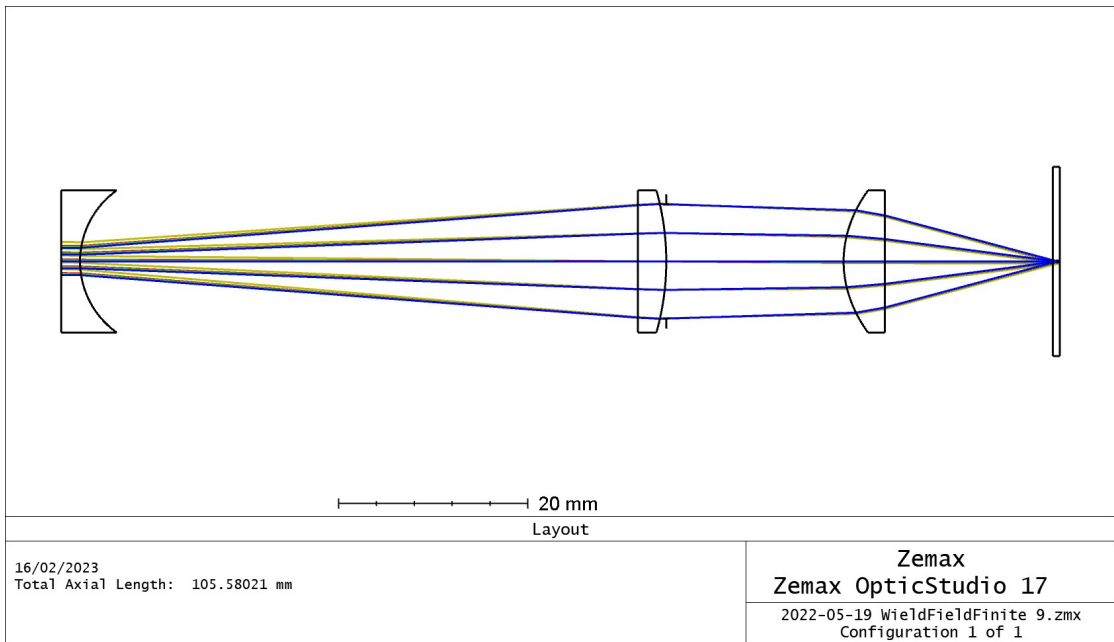


Figure A.4: Layout of the arrangement of lenses in the custom objective, with ray-traced beams.

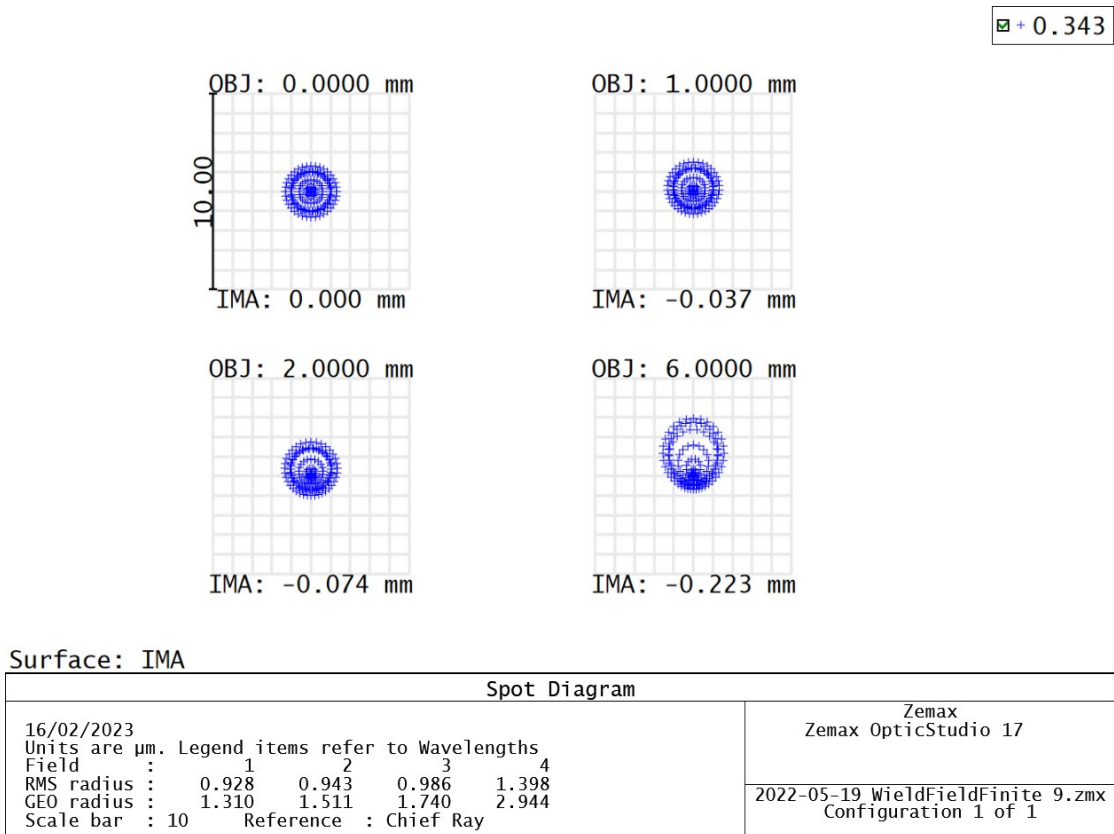


Figure A.5: Ray-traced spot diagrams for spots at 0, 37, 74 and 223 μm from the optical axis, corresponding to positions on the sensor at 0, 1, 2 and 6 mm, respectively.

Bibliography

- [1] N. Bloembergen. ‘Laser-induced electric breakdown in solids’. In: *IEEE Journal of Quantum Electronics* 10.3 (1974), pp. 375–386. DOI: 10.1109/JQE.1974.1068132.
- [2] A. A. Manenkov and A. M. Prokhorov. ‘Laser-induced damage in solids’. In: *Soviet Physics Uspekhi* 29.1 (1986), pp. 104–122. DOI: 10.1070/PU1986v029n01ABEH003117.
- [3] B. C. Stuart, M. D. Feit, A. M. Rubenchik, B. W. Shore and M. D. Perry. ‘Laser-Induced Damage in Dielectrics with Nanosecond to Subpicosecond Pulses’. In: *Physical Review Letters* 74.12 (1995), pp. 2248–2251. DOI: 10.1103/PhysRevLett.74.2248.
- [4] D. Du, X. Liu, G. Korn, J. Squier and G. Mourou. ‘Laser-induced breakdown by impact ionization in SiO₂ with pulse widths from 7 ns to 150 fs’. In: *Applied Physics Letters* 64.23 (1994), pp. 3071–3073. DOI: 10.1063/1.111350.
- [5] M. Göppert-Mayer. ‘Über Elementarakte mit zwei Quantensprüngen’. In: *Annalen der Physik* 401.3 (1931), pp. 273–294. DOI: 10.1002/andp.19314010303.
- [6] K. M. Davis, K. Miura, N. Sugimoto and K. Hirao. ‘Writing waveguides in glass with a femtosecond laser’. In: *Optics Letters* 21.21 (1996), pp. 1729–1731. DOI: 10.1364/OL.21.001729.
- [7] Y. Shimotsuma, P. G. Kazansky, J. Qiu and K. Hirao. ‘Self-Organized Nanogratings in Glass Irradiated by Ultrashort Light Pulses’. In: *Physical Review Letters* 91.24 (2003), p. 247405. DOI: 10.1103/PhysRevLett.91.247405.
- [8] A. Marcinkevičius, S. Juodkazis, M. Watanabe, M. Miwa, S. Matsuo, H. Misawa and J. Nishii. ‘Femtosecond laser-assisted three-dimensional microfabrication in silica’. In: *Optics Letters* 26.5 (2001), pp. 277–279. DOI: 10.1364/OL.26.000277.
- [9] Y. Bellouard, A. Said, M. Dugan and P. Bado. ‘Fabrication of high-aspect ratio, microfluidic channels and tunnels using femtosecond laser pulses and chemical etching’. In: *Optics Express* 12.10 (2004), pp. 2120–2129. DOI: 10.1364/OPEX.12.002120.
- [10] M. Beresna, M. Gecevičius and P. G. Kazansky. ‘Polarization sensitive elements fabricated by femtosecond laser nanostructuring of glass [Invited]’. In: *Optical Materials Express* 1.4 (2011), p. 783. DOI: 10.1364/OME.1.000783.
- [11] J. Zhang, M. Gecevičius, M. Beresna and P. G. Kazansky. ‘Seemingly Unlimited Lifetime Data Storage in Nanostructured Glass’. In: *Physical Review Letters* 112.3 (2014), p. 033901. DOI: 10.1103/PhysRevLett.112.033901.
- [12] G. Torun, T. Kishi and Y. Bellouard. ‘Direct-write laser-induced self-organization and metallization beyond the focal volume in tellurite glass’. In: *Physical Review Materials* 5.5 (2021), p. 055201. DOI: 10.1103/PhysRevMaterials.5.055201.

Bibliography

- [13] T. Kononenko, M. Meier, M. Komlenok, S. Pimenov, V. Romano, V. Pashinin and V. Konov. ‘Microstructuring of diamond bulk by IR femtosecond laser pulses’. In: *Applied Physics A* 90.4 (2008), pp. 645–651. DOI: 10.1007/s00339-007-4350-9.
- [14] C. Hnatovsky, R. S. Taylor, P. P. Rajeev, E. Simova, V. R. Bhardwaj, D. M. Rayner and P. B. Corkum. ‘Pulse duration dependence of femtosecond-laser-fabricated nanogratings in fused silica’. In: *Applied Physics Letters* 87.1 (2005), p. 014104. DOI: 10.1063/1.1991991.
- [15] Y. Bellouard and M.-O. Hongler. ‘Femtosecond-laser generation of self-organized bubble patterns in fused silica’. In: *Optics Express* 19.7 (2011), pp. 6807–6821. DOI: 10.1364/OE.19.006807.
- [16] N. Groothoff, M.-O. Hongler, P. Kazansky and Y. Bellouard. ‘Transition and self-healing process between chaotic and self-organized patterns observed during femtosecond laser writing’. In: *Optics Express* 23.13 (2015), pp. 16993–17007. DOI: 10.1364/OE.23.016993.
- [17] C.-E. Athanasiou, M.-O. Hongler and Y. Bellouard. ‘Unraveling Brittle-Fracture Statistics from Intermittent Patterns Formed During Femtosecond Laser Exposure’. In: *Physical Review Applied* 8.5 (2017), p. 054013. DOI: 10.1103/PhysRevApplied.8.054013.
- [18] C. Maclair, M. Zamfirescu, J. P. Colombier, G. Cheng, K. Mishchik, E. Audouard and R. Stoian. ‘Control of ultrafast laser-induced bulk nanogratings in fused silica via pulse time envelopes’. In: *Optics Express* 20.12 (2012), p. 12997. DOI: 10.1364/OE.20.012997.
- [19] R. Stoian, K. Mishchik, G. Cheng, C. Maclair, C. D’Amico, J. P. Colombier and M. Zamfirescu. ‘Investigation and control of ultrafast laser-induced isotropic and anisotropic nanoscale-modulated index patterns in bulk fused silica’. In: *Optical Materials Express* 3.10 (2013), pp. 1755–1768. DOI: 10.1364/OME.3.001755.
- [20] B. Fischer, W. Rohringer, N. Panzer and S. Hecker. ‘Acoustic Process Control for Laser Material Processing: Optical microphone as a novel “ear” for industrial manufacturing’. In: *Laser Technik Journal* 14.5 (2017), pp. 21–25. DOI: 10.1002/latj.201700029.
- [21] S. Hecker, M. Scharun and T. Graf. ‘Process monitoring based on plasma emission for power-modulated glass welding with bursts of subpicosecond laser pulses’. In: *Applied Optics* 60.12 (2021), p. 3526. DOI: 10.1364/AO.420037.
- [22] P. Bado, A. A. Said, M. Dugan, T. S. Sosnowki and S. Wright. ‘Dramatic improvements in waveguide manufacturing with femtosecond lasers’. In: *Technical Proceedings*. National Fiber Optic Engineers Conference. Dallas, TX, USA, 2002, pp. 1153–1158.
- [23] K. Sugioka, Y. Cheng and K. Midorikawa. ‘Three-dimensional micromachining of glass using femtosecond laser for lab-on-a-chip device manufacture’. In: *Applied Physics A* 81.1 (2005), pp. 1–10. DOI: 10.1007/s00339-005-3225-1.
- [24] Y. Kondo, J. Qiu, T. Mitsuyu, K. Hirao and T. Yoko. ‘Three-Dimensional Microdrilling of Glass by Multiphoton Process and Chemical Etching’. In: *Japanese Journal of Applied Physics* 38.10 (1999), p. L1146. DOI: 10.1143/JJAP.38.L1146.
- [25] S. Kiyama, S. Matsuo, S. Hashimoto and Y. Morihira. ‘Examination of Etching Agent and Etching Mechanism on Femtosecond Laser Microfabrication of Channels Inside Vitreous Silica Substrates’. In: *The Journal of Physical Chemistry C* 113.27 (2009), pp. 11560–11566. DOI: 10.1021/jp900915r.
- [26] C. A. Ross, D. G. MacLachlan, D. Choudhury and R. R. Thomson. ‘Optimisation of ultrafast laser assisted etching in fused silica’. In: *Optics Express* 26.19 (2018), pp. 24343–24356. DOI: 10.1364/OE.26.024343.

- [27] E. Casamenti, S. Pollonghini and Y. Bellouard. ‘Few pulses femtosecond laser exposure for high efficiency 3D glass micromachining’. In: *Optics Express* 29.22 (2021), p. 35054. DOI: 10.1364/OE.435163.
- [28] Y. Bellouard. ‘The Femtoprint Project’. In: *Journal of Laser Micro/Nanoengineering* 7.1 (2012), pp. 1–10. DOI: 10.2961/jlmn.2012.01.0001.
- [29] A. Schaap, T. Rohrlack and Y. Bellouard. ‘Optical classification of algae species with a glass lab-on-a-chip’. In: *Lab on a Chip* 12.8 (2012), p. 1527. DOI: 10.1039/c2lc21091f.
- [30] V. Tielen and Y. Bellouard. ‘Three-Dimensional Glass Monolithic Micro-Flexure Fabricated by Femtosecond Laser Exposure and Chemical Etching’. In: *Micromachines* 5.3 (2014), pp. 697–710. DOI: 10.3390/mi5030697.
- [31] Nazir and Bellouard. ‘A Monolithic Gimbal Micro-Mirror Fabricated and Remotely Tuned with a Femtosecond Laser’. In: *Micromachines* 10.9 (2019), p. 611. DOI: 10.3390/mi10090611.
- [32] E. Casamenti, T. Yang, P. Vlugter and Y. Bellouard. ‘Vibration monitoring based on optical sensing of mechanical nonlinearities in glass suspended waveguides’. In: *Optics Express* 29.7 (2021), p. 10853. DOI: 10.1364/OE.414191.
- [33] M. Will, S. Nolte, B. N. Chichkov and A. Tünnermann. ‘Optical properties of waveguides fabricated in fused silica by femtosecond laser pulses’. In: *Applied Optics* 41.21 (2002), p. 4360. DOI: 10.1364/AO.41.004360.
- [34] G. Li, K. A. Winick, A. A. Said, M. Dugan and P. Bado. ‘Waveguide electro-optic modulator in fused silica fabricated by femtosecond laser direct writing and thermal poling’. In: *Optics Letters* 31.6 (2006), p. 739. DOI: 10.1364/OL.31.000739.
- [35] L. Sansoni, F. Sciarrino, G. Vallone, P. Mataloni, A. Crespi, R. Ramponi and R. Osellame. ‘Polarization Entangled State Measurement on a Chip’. In: *Physical Review Letters* 105.20 (2010), p. 200503. DOI: 10.1103/PhysRevLett.105.200503.
- [36] C. Florea, K. Winick, Y. Sikorski, A. Said and P. Bado. ‘Optical waveguide amplifier in Nd-doped glass written with near-IR femtosecond laser pulses’. In: *Conference on Lasers and Electro-Optics (CLEO 2000). Technical Digest. Postconference Edition. TOPS Vol.39 (IEEE Cat. No.00CH37088)*. Conference on Lasers and Electro-Optics (CLEO 2000). Technical Digest. Postconference Edition. TOPS Vol.39. San Francisco, CA, USA: IEEE, 2000, pp. 128–129. ISBN: 978-1-55752-634-2. DOI: 10.1109/CLEO.2000.906817.
- [37] J. Morizet, G. Ducourthial, W. Supatto, A. Boutillon, R. Legouis, M.-C. Schanne-Klein, C. Stringari and E. Beaurepaire. ‘High-speed polarization-resolved third-harmonic microscopy’. In: *Optica* 6.3 (2019), p. 385. DOI: 10.1364/OPTICA.6.000385.
- [38] M. Sakakura, Y. Lei, L. Wang, Y.-H. Yu and P. G. Kazansky. ‘Ultralow-loss geometric phase and polarization shaping by ultrafast laser writing in silica glass’. In: *Light: Science & Applications* 9.1 (2020), p. 15. DOI: 10.1038/s41377-020-0250-y.
- [39] R. D. Simmonds, P. S. Salter, A. Jesacher and M. J. Booth. ‘Three dimensional laser microfabrication in diamond using a dual adaptive optics system’. In: *Optics Express* 19.24 (2011), pp. 24122–24128. DOI: 10.1364/OE.19.024122.
- [40] Y. Hayasaki, T. Sugimoto, A. Takita and N. Nishida. ‘Variable holographic femtosecond laser processing by use of a spatial light modulator’. In: *Applied Physics Letters* 87.3 (2005), p. 031101. DOI: 10.1063/1.1992668.

Bibliography

- [41] D. Grojo, M. Gertsvolf, S. Lei, T. Barillot, D. M. Rayner and P. B. Corkum. ‘Exciton-seeded multiphoton ionization in bulk SiO₂’. In: *Physical Review B* 81.21 (2010), p. 212301. DOI: 10.1103/PhysRevB.81.212301.
- [42] P. Martin, S. Guizard, P. Daguzan, G. Petite, P. D’Oliveira, P. Meynadier and M. Perdrix. ‘Subpicosecond study of carrier trapping dynamics in wide-band-gap crystals’. In: *Physical Review B* 55.9 (1997), pp. 5799–5810. DOI: 10.1103/PhysRevB.55.5799.
- [43] L. Skuja. ‘Optical properties of fused silica’. In: *Defects in SiO₂ and Related Dielectrics: Science and Technology, NATO Science Series II*. NATO ASI school on SiO₂. Vol. 2. Erice, Italy: Kluwer Academic Publishers, Dodrecht-Boston-London, 2000, pp. 73–116.
- [44] M. Beresna, M. Gecevičius, M. Lancry, B. Poumellec and P. G. Kazansky. ‘Broadband anisotropy of femtosecond laser induced nanogratings in fused silica’. In: *Applied Physics Letters* 103.13 (2013), p. 131903. DOI: 10.1063/1.4821513.
- [45] W. H. Zachariasen. ‘THE ATOMIC ARRANGEMENT IN GLASS’. In: *Journal of the American Chemical Society* 54.10 (1932), pp. 3841–3851. DOI: 10.1021/ja01349a006.
- [46] N. S. Shcheblanov, M. E. Povarnitsyn, K. N. Mishchik and A. Tanguy. ‘Raman spectroscopy of femtosecond multipulse irradiation of vitreous silica: Experiment and simulation’. In: *Physical Review B* 97.5 (2018), p. 054106. DOI: 10.1103/PhysRevB.97.054106.
- [47] F. Galeener. ‘Planar rings in glasses’. In: *Solid State Communications* 44.7 (1982), pp. 1037–1040. DOI: 10.1016/0038-1098(82)90329-5.
- [48] F. L. Galeener. ‘Planar rings in vitreous silica’. In: *Journal of Non-Crystalline Solids* 49.1 (1982), pp. 53–62. DOI: 10.1016/0022-3093(82)90108-9.
- [49] J. Hernandez-Rueda, J. Clarijs, D. van Oosten and D. M. Krol. ‘The influence of femtosecond laser wavelength on waveguide fabrication inside fused silica’. In: *Applied Physics Letters* 110.16 (2017), p. 161109. DOI: 10.1063/1.4981124.
- [50] P. Vlugter and Y. Bellouard. ‘Elastic properties of self-organized nanogratings produced by femtosecond laser exposure of fused silica’. In: *Physical Review Materials* 4.2 (2020), p. 023607. DOI: 10.1103/PhysRevMaterials.4.023607.
- [51] G. Corrielli, A. Crespi, R. Geremia, R. Ramponi, L. Sansoni, A. Santinelli, P. Mataloni, F. Sciarrino and R. Osellame. ‘Rotated waveplates in integrated waveguide optics’. In: *Nature Communications* 5.1 (2014), p. 4249. DOI: 10.1038/ncomms5249.
- [52] V. R. Bhardwaj, E. Simova, P. P. Rajeev, C. Hnatovsky, R. S. Taylor, D. M. Rayner and P. B. Corkum. ‘Optically Produced Arrays of Planar Nanostructures inside Fused Silica’. In: *Physical Review Letters* 96.5 (2006), p. 057404. DOI: 10.1103/PhysRevLett.96.057404.
- [53] P. G. Kazansky, H. Inouye, T. Mitsuyu, K. Miura, J. Qiu, K. Hirao and F. Starrost. ‘Anomalous Anisotropic Light Scattering in Ge-Doped Silica Glass’. In: *Physical Review Letters* 82.10 (1999), pp. 2199–2202. DOI: 10.1103/PhysRevLett.82.2199.
- [54] J. D. Mills, P. G. Kazansky, E. Bricchi and J. J. Baumberg. ‘Embedded anisotropic microreflectors by femtosecond-laser nanomachining’. In: *Applied Physics Letters* 81.2 (2002), pp. 196–198. DOI: 10.1063/1.1492004.
- [55] M. Born, E. Wolf and A. B. Bhatia. *Principles of optics: electromagnetic theory of propagation, interference, and diffraction of light*. Seventh (expanded) anniversary edition, 60th anniversary edition. Cambridge: Cambridge University Press, 2019. ISBN: 978-1-108-47743-7.

- [56] R. Taylor, C. Hnatovsky and E. Simova. ‘Applications of femtosecond laser induced self-organized planar nanocracks inside fused silica glass’. In: *Laser & Photonics Review* 2.1 (2008), pp. 26–46. DOI: 10.1002/lpor.200710031.
- [57] A. Rudenko, J.-P. Colombier and T. E. Itina. ‘From random inhomogeneities to periodic nanostructures induced in bulk silica by ultrashort laser’. In: *Physical Review B* 93.7 (2016), p. 075427. DOI: 10.1103/PhysRevB.93.075427.
- [58] J. Bonse and S. Gräf. ‘Maxwell Meets Marangoni—A Review of Theories on Laser-Induced Periodic Surface Structures’. In: *Laser & Photonics Reviews* 14.10 (2020), p. 2000215. DOI: 10.1002/lpor.202000215.
- [59] A. Rudenko, J.-P. Colombier, T. E. Itina and R. Stoian. ‘Genesis of Nanogratings in Silica Bulk via Multipulse Interplay of Ultrafast Photo-Excitation and Hydrodynamics’. In: *Advanced Optical Materials* 9.20 (2021), p. 2100973. DOI: 10.1002/adom.202100973.
- [60] E. Bricchi, B. G. Klappauf and P. G. Kazansky. ‘Form birefringence and negative index change created by femtosecond direct writing in transparent materials’. In: *Optics Letters* 29.1 (2004), pp. 119–121. DOI: 10.1364/OL.29.000119.
- [61] Y. Shimotsuma, M. Sakakura, P. G. Kazansky, M. Beresna, J. Qiu, K. Miura and K. Hirao. ‘Ultrafast Manipulation of Self-Assembled Form Birefringence in Glass’. In: *Advanced Materials* 22.36 (2010), pp. 4039–4043. DOI: 10.1002/adma.201000921.
- [62] W. Cai, A. R. Libertun and R. Piestun. ‘Polarization selective computer-generated holograms realized in glass by femtosecond laser induced nanogratings’. In: *Optics Express* 14.9 (2006), p. 3785. DOI: 10.1364/OE.14.003785.
- [63] A. Couairon and A. Mysyrowicz. ‘Femtosecond filamentation in transparent media’. In: *Physics Reports* 441.2 (2007), pp. 47–189. DOI: 10.1016/j.physrep.2006.12.005.
- [64] Y. Lei, H. Wang, L. Skuja, B. Kühn, B. Franz, Y. Svirko and P. G. Kazansky. ‘Ultrafast Laser Writing in Different Types of Silica Glass’. In: *Laser & Photonics Reviews* (2023), p. 2200978. DOI: 10.1002/lpor.202200978.
- [65] J. Hebling. ‘Derivation of the pulse front tilt caused by angular dispersion’. In: *Optical and Quantum Electronics* 28.12 (1996), pp. 1759–1763. DOI: 10.1007/BF00698541.
- [66] S. Akturk, X. Gu, E. Zeek and R. Trebino. ‘Pulse-front tilt caused by spatial and temporal chirp’. In: *Optics Express* 12.19 (2004), p. 4399. DOI: 10.1364/OPEX.12.004399.
- [67] D. N. Vitek, E. Block, Y. Bellouard, D. E. Adams, S. Backus, D. Kleinfeld, C. G. Durfee and J. A. Squier. ‘Spatio-temporally focused femtosecond laser pulses for nonreciprocal writing in optically transparent materials’. In: *Optics Express* 18.24 (2010), pp. 24673–24678. DOI: 10.1364/OE.18.024673.
- [68] P. G. Kazansky, W. Yang, E. Bricchi, J. Bovatsek, A. Arai, Y. Shimotsuma, K. Miura and K. Hirao. ‘“Quill” writing with ultrashort light pulses in transparent materials’. In: *Applied Physics Letters* 90.15 (2007), p. 151120. DOI: 10.1063/1.2722240.
- [69] W. Yang, P. G. Kazansky, Y. Shimotsuma, M. Sakakura, K. Miura and K. Hirao. ‘Ultrafast-pulse laser calligraphy’. In: *Applied Physics Letters* 93.17 (2008), p. 171109. DOI: 10.1063/1.3010375.
- [70] S. Zhang, D. Asoubar, R. Kammel, S. Nolte and F. Wyrowski. ‘Analysis of pulse front tilt in simultaneous spatial and temporal focusing’. In: *Journal of the Optical Society of America A* 31.11 (2014), p. 2437. DOI: 10.1364/JOSAA.31.002437.

Bibliography

- [71] D. Kühn, A. Treffer, F. Wyrowski and R. Grunwald. ‘Simultaneous spatio-temporal focusing with pulse front symmetrization’. In: *Optics Letters* 47.4 (2022), p. 750. DOI: 10.1364/OL.449597.
- [72] C. Hnatovsky, R. S. Taylor, E. Simova, V. R. Bhardwaj, D. M. Rayner and P. B. Corkum. ‘High-resolution study of photoinduced modification in fused silica produced by a tightly focused femtosecond laser beam in the presence of aberrations’. In: *Journal of Applied Physics* 98.1 (2005), p. 013517. DOI: 10.1063/1.1944223.
- [73] K. Bergner, B. Seyfarth, K. A. Lammers, T. Ullsperger, S. Döring, M. Heinrich, S. Kumkar, D. Flamm, A. Tünnermann and S. Nolte. ‘Spatio-temporal analysis of glass volume processing using ultrashort laser pulses’. In: *Applied Optics* 57.16 (2018), pp. 4618–4632. DOI: 10.1364/AO.57.004618.
- [74] Y. Bellouard, T. Colomb, C. Depeursinge, M. Dugan, A. A. Said and P. Bado. ‘Nanoindentation and birefringence measurements on fused silica specimen exposed to low-energy femtosecond pulses’. In: *Optics Express* 14.18 (2006), p. 8360. DOI: 10.1364/OE.14.008360.
- [75] A. Beaudier, F. R. Wagner and J.-Y. Natoli. ‘Using NBOHC fluorescence to predict multi-pulse laser-induced damage in fused silica’. In: *Optics Communications* 402 (2017), pp. 535–539. DOI: 10.1016/j.optcom.2017.06.073.
- [76] M. D. Young, J. J. Field, K. E. Sheetz, R. A. Bartels and J. Squier. ‘A pragmatic guide to multiphoton microscope design’. In: *Advances in Optics and Photonics* 7.2 (2015), pp. 276–378. DOI: 10.1364/AOP.7.000276.
- [77] M. Delfino. ‘A comprehensive optical second harmonic generation study of the non-centrosymmetric character of biological structures’. In: *Journal of Biological Physics* 6.3 (1978), pp. 105–117. DOI: 10.1007/BF02328933.
- [78] I. Freund and M. Deutsch. ‘Second-harmonic microscopy of biological tissue’. In: *Optics Letters* 11.2 (1986), p. 94. DOI: 10.1364/OL.11.000094.
- [79] P. Karpinski, V. Shvedov, W. Krolikowski and C. Hnatovsky. ‘Laser-writing inside uniaxially birefringent crystals: fine morphology of ultrashort pulse-induced changes in lithium niobate’. In: *Optics Express* 24.7 (2016), p. 7456. DOI: 10.1364/OE.24.007456.
- [80] T. J. Driscoll and N. M. Lawandy. ‘Optically encoded second-harmonic generation in bulk silica-based glasses’. In: *Journal of the Optical Society of America B* 11.2 (1994), p. 355. DOI: 10.1364/JOSAB.11.000355.
- [81] R. A. Myers, N. Mukherjee and S. R. J. Brueck. ‘Large second-order nonlinearity in poled fused silica’. In: *Optics Letters* 16.22 (1991), p. 1732. DOI: 10.1364/OL.16.001732.
- [82] V. Dominic and J. Feinberg. ‘High-resolution map of the dc electric field in second-harmonic-generating glass’. In: *Journal of the Optical Society of America B* 11.10 (1994), p. 2016. DOI: 10.1364/JOSAB.11.002016.
- [83] G. Papon, N. Marquestaut, Y. Petit, A. Royon, M. Dussauze, V. Rodriguez, T. Cardinal and L. Canioni. ‘Femtosecond single-beam direct laser poling of stable and efficient second-order nonlinear optical properties in glass’. In: *Journal of Applied Physics* 115.11 (2014), p. 113103. DOI: 10.1063/1.4869058.
- [84] T. Y. F. Tsang. ‘Optical third-harmonic generation at interfaces’. In: *Physical Review A* 52.5 (1995), pp. 4116–4125. DOI: 10.1103/PhysRevA.52.4116.

- [85] Y. Barad, H. Eisenberg, M. Horowitz and Y. Silberberg. ‘Nonlinear scanning laser microscopy by third harmonic generation’. In: *Applied Physics Letters* 70.8 (1997), pp. 922–924. DOI: 10.1063/1.118442.
- [86] M. Müller, J. Squier, K. R. Wilson and G. J. Brakenhoff. ‘3D microscopy of transparent objects using third-harmonic generation’. In: *Journal of Microscopy* 191.3 (1998), pp. 266–274. DOI: 10.1046/j.1365-2818.1998.00399.x.
- [87] J. Squier, M. Muller, G. Brakenhoff and K. R. Wilson. ‘Third harmonic generation microscopy’. In: *Optics Express* 3.9 (1998), pp. 315–324. DOI: 10.1364/oe.3.000315.
- [88] P. J. Campagnola, A. C. Millard, M. Terasaki, P. E. Hoppe, C. J. Malone and W. A. Mohler. ‘Three-Dimensional High-Resolution Second-Harmonic Generation Imaging of Endogenous Structural Proteins in Biological Tissues’. In: *Biophysical Journal* 82.1 (2002), pp. 493–508. DOI: 10.1016/S0006-3495(02)75414-3.
- [89] D. Oron, E. Tal and Y. Silberberg. ‘Depth-resolved multiphoton polarization microscopy by third-harmonic generation’. In: *Optics Letters* 28.23 (2003), p. 2315. DOI: 10.1364/OL.28.002315.
- [90] J. A. Squier and M. Müller. ‘Third-harmonic generation imaging of laser-induced breakdown in glass’. In: *Applied Optics* 38.27 (1999), p. 5789. DOI: 10.1364/AO.38.005789.
- [91] C. B. Schaffer, J. Aus der Au, E. Mazur and J. A. Squier. ‘Micromachining and material change characterization using femtosecond laser oscillators’. In: *Proc. SPIE 4633, Commercial and Biomedical Applications of Ultrafast and Free-Electron Lasers. High-Power Lasers and Applications*. 2002. DOI: 10.1117/12.461370.
- [92] G. D. Marshall, A. Jesacher, A. Thayil, M. J. Withford and M. Booth. ‘Three-dimensional imaging of direct-written photonic structures’. In: *Optics Letters* 36.5 (2011), p. 695. DOI: 10.1364/OL.36.000695.
- [93] A. Jesacher, P. S. Salter and M. J. Booth. ‘Refractive index profiling of direct laser written waveguides: tomographic phase imaging’. In: *Optical Materials Express* 3.9 (2013), p. 1223. DOI: 10.1364/OME.3.001223.
- [94] M. Ams, P. Dekker, S. Gross and M. J. Withford. ‘Fabricating waveguide Bragg gratings (WBGs) in bulk materials using ultrashort laser pulses’. In: *Nanophotonics* 6.5 (2017), pp. 743–763. DOI: 10.1515/nanoph-2016-0119.
- [95] J. Guan, X. Liu and M. J. Booth. ‘Ultrafast laser writing quill effect in low loss waveguide fabrication regime’. In: *Optics Express* 26.23 (2018), p. 30716. DOI: 10.1364/OE.26.030716.
- [96] J. Guan, X. Liu and M. Booth. ‘Investigation of structural mechanisms of laser-written waveguide formation through third-harmonic microscopy’. In: *Optics Letters* 44.4 (2019), pp. 1039–1042. DOI: 10.1364/OL.44.001039.
- [97] M. Samim, S. Krouglov and V. Barzda. ‘Three-photon Stokes-Mueller polarimetry’. In: *Physical Review A* 93.3 (2016), p. 033839. DOI: 10.1103/PhysRevA.93.033839.
- [98] R. Grigutis, V. Jukna, M. Navickas, G. Tamošauskas, K. Staliunas and A. Dubietis. ‘Conical third harmonic generation from volume nanogratings induced by filamentation of femtosecond pulses in transparent bulk materials’. In: *Optics Express* 29.24 (2021), p. 40633. DOI: 10.1364/OE.444901.
- [99] K. Ardaneh, R. Meyer, M. Hassan, R. Giust, B. Morel, A. Couairon, G. Bonnaud and F. Courvoisier. ‘Femtosecond laser-induced sub-wavelength plasma inside dielectrics: I. Field enhancement’. In: *Physics of Plasmas* 29.7 (2022), p. 072715. DOI: 10.1063/5.0086708.

Bibliography

- [100] O. Bernard and Y. Bellouard. ‘On the use of a digital twin to enhance femtosecond laser inscription of arbitrary phase patterns’. In: *Journal of Physics: Photonics* 3.3 (2021), p. 035003. DOI: 10.1088/2515-7647/abf743.
- [101] F. Beltrame, B. Bianco, A. Geraci, G. Laub and P. Schwarzman. ‘Three dimensional imaging of cells through digital holographic microscopy’. In: *Proceedings of SPIE - The International Society for Optical Engineering* 515 (1984), pp. 232–235. DOI: 10.1117/12.964763.
- [102] E. Cuche, F. Bevilacqua and C. Depeursinge. ‘Digital holography for quantitative phase-contrast imaging’. In: *Optics Letters* 24.5 (1999), pp. 291–293. DOI: 10.1364/OL.24.000291.
- [103] E. Cuche, P. Marquet and C. Depeursinge. ‘Simultaneous amplitude-contrast and quantitative phase-contrast microscopy by numerical reconstruction of Fresnel off-axis holograms’. In: *Applied Optics* 38.34 (1999), pp. 6994–7001. DOI: 10.1364/AO.38.006994.
- [104] P. Marquet, B. Rappaz, P. Magistretti, E. Cuche, Y. Emery, T. Colomb and C. Depeursinge. ‘Digital holographic microscopy: A noninvasive contrast imaging technique allowing quantitative visualization of living cells with subwavelength axial accuracy’. In: *Optics Letters* 30.5 (2005), pp. 468–470. DOI: 10.1364/OL.30.000468.
- [105] B. N. Chichkov, C. Momma, S. Nolte, F. von Alvensleben and A. Tünnermann. ‘Femtosecond, picosecond and nanosecond laser ablation of solids’. In: *Applied Physics A* 63.2 (1996), pp. 109–115. DOI: 10.1007/BF01567637.
- [106] M. Kaganov, I. Lifshitz and L. Tanatarov. ‘Relaxation between Electrons and the Crystalline Lattice’. In: *Journal of Experimental and Theoretical Physics* 4.2 (1955), p. 173.
- [107] P. Virtanen *et al.* ‘SciPy 1.0: fundamental algorithms for scientific computing in Python’. In: *Nature Methods* 17.3 (2020), pp. 261–272. DOI: 10.1038/s41592-019-0686-2.
- [108] A. Champion, M. Beresna, P. Kazansky and Y. Bellouard. ‘Stress distribution around femtosecond laser affected zones: effect of nanogratings orientation’. In: *Optics Express* 21.21 (2013), pp. 24942–24951. DOI: 10.1364/OE.21.024942.
- [109] Y. Bellouard, A. Champion, B. McMillen, S. Mukherjee, R. R. Thomson, C. Pépin, P. Gillet and Y. Cheng. ‘Stress-state manipulation in fused silica via femtosecond laser irradiation’. In: *Optica* 3.12 (2016), pp. 1285–1293. DOI: 10.1364/OPTICA.3.001285.
- [110] O. Bernard, A. Kraxner, A. Boukhayma, C. Enz, Y. Bellouard and J. Squier. *Third-harmonic generation monitoring of femtosecond laser-induced in-volume functional modifications*. preprint. 2023. DOI: 10.1364/opticaopen.22040459.v1.
- [111] B. Weigelin, G.-J. Bakker and P. Friedl. ‘Third harmonic generation microscopy of cells and tissue organization’. In: *Journal of Cell Science* 129.2 (2016), pp. 245–255. DOI: 10.1242/jcs.152272.
- [112] Schott AG. *Optical Glass Data Sheets*. 2021.
- [113] A. Boukhayma, A. Kraxner, A. Caizzone, M. Yang, D. Bold and C. Enz. ‘Comparison of Two in Pixel Source Follower Schemes for Deep Subelectron Noise CMOS Image Sensors’. In: *IEEE Journal of the Electron Devices Society* 10 (2022), pp. 687–695. DOI: 10.1109/JEDS.2022.3200520.
- [114] G. Wagnière. ‘Optical activity of higher order in a medium of randomly oriented molecules’. In: *The Journal of Chemical Physics* 77.6 (1982), pp. 2786–2792. DOI: 10.1063/1.444166.

- [115] S. Rajesh and Y. Bellouard. ‘Towards fast femtosecond laser micromachining of fused silica: The effect of deposited energy.’ In: *Optics Express* 18.20 (2010), pp. 21490–21497. DOI: 10.1364/OE.18.021490.
- [116] M. Ochoa, P. Roldán-Varona, J. F. Algorri, J. M. López-Higuera and L. Rodríguez-Cobo. ‘Polarisation-independent ultrafast laser selective etching processing in fused silica’. In: *Lab on a Chip* (2023), p. 10.1039.D3LC00052D. DOI: 10.1039/D3LC00052D.
- [117] Y. Bellouard, E. Barthel, A. A. Said, M. Dugan and P. Bado. ‘Scanning thermal microscopy and Raman analysis of bulk fused silica exposed to low-energy femtosecond laser pulses’. In: *Optics Express* 16.24 (2008), pp. 19520–19534. DOI: 10.1364/OE.16.019520.
- [118] T. Dolgova, M. Martemyanov, N. Didenko, A. Fedyanin and O. Aktsipetrov. ‘Giant third-harmonic generation in porous silicon photonic crystals and microcavities’. In: *Postconference digest. Quantum Electronics and Laser Science Conference (QELS)*. Ed. by American Physical Society, Lasers and Electro-optics Society (Institute of Electrical and Electronics Engineers) and Optical Society of America. Trends in optics and photonics series. Long Beach, California, USA: Optical Society of America, 2002. ISBN: 978-1-55752-707-3.
- [119] V. Mel’nikov, L. Golovan, S. Konorov, D. Muzychenko, A. Fedotov, A. Zheltikov, V. Timoshenko and P. Kashkarov. ‘Second-harmonic generation in strongly scattering porous gallium phosphide’. In: *Applied Physics B* 79.2 (2004), pp. 225–228. DOI: 10.1007/s00340-004-1530-6.
- [120] R. Genthial, E. Beaurepaire, M.-C. Schanne-Klein, F. Peyrin, D. Farlay, C. Olivier, Y. Bala, G. Boivin, J.-C. Vial, D. Débarre and A. Gourrier. ‘Label-free imaging of bone multiscale porosity and interfaces using third-harmonic generation microscopy’. In: *Scientific Reports* 7.1 (2017), p. 3419. DOI: 10.1038/s41598-017-03548-5.
- [121] N. V. Mitetelo, S. E. Svyakhovskiy, A. D. Gartman, A. A. Kudrinskii, T. V. Murzina and A. I. Maydykovskiy. ‘Enhancement of Nonlinear Optical Effects in Porous Composite Plasmonic Structures’. In: *JETP Letters* 107.5 (2018), pp. 297–301. DOI: 10.1134/S0021364018050107.
- [122] H. Bach and N. Neuroth. *The Properties of Optical Glass*. Berlin: Springer Berlin, 2013. ISBN: 978-3-642-63349-2.
- [123] L. Shah, A. Y. Arai, S. M. Eaton and P. R. Herman. ‘Waveguide writing in fused silica with a femtosecond fiber laser at 522 nm and 1 MHz repetition rate’. In: *Optics Express* 13.6 (2005), pp. 1999–2006. DOI: 10.1364/OPEX.13.001999.
- [124] B. Hermann and Y. Bellouard. ‘Femtosecond UV laser processing of fused silica for rapid fabrication of direct-write waveguides’. In: *to be published* (2023).
- [125] C. Hönninger, F. Morin and M. Delaigue. ‘Pulse laser system that is temporally variable in terms of rhythm and/or amplitude’. U.S. pat. 11108207B2. 2017.
- [126] R. Ricca and Y. Bellouard. ‘Femtosecond laser-induced confined nanocrystallization in dielectric multilayers’. In: *CLEO 2022*. San Jose, CA, USA: Optica Publishing Group, 2022.
- [127] R. Ricca, V. Boureau and Y. Bellouard. ‘Ultrafast laser interaction with transparent multi-layer $\text{SiO}_2/\text{Si}_3\text{N}_4$ films’. In: *Journal of Applied Physics* 130.24 (2021), p. 243105. DOI: 10.1063/5.0065726.

Bibliography

- [128] R. Ricca and Y. Bellouard. *Single layer, sub-wavelength, femtosecond laser-induced confined nano-crystallization in a multi-stack dielectrics*. 2022.
- [129] D. Ashkenasi, M. Lorenz, R. Stoian and A. Rosenfeld. ‘Surface damage threshold and structuring of dielectrics using femtosecond laser pulses: the role of incubation’. In: *Applied Surface Science* 150.1 (1999), pp. 101–106. DOI: 10.1016/S0169-4332(99)00228-7.
- [130] Z. Sun, M. Lenzner and W. Rudolph. ‘Generic incubation law for laser damage and ablation thresholds’. In: *Journal of Applied Physics* 117.7 (2015), p. 073102. DOI: 10.1063/1.4913282.
- [131] B. Chimier, O. Utéza, N. Sanner, M. Sentis, T. Itina, P. Lassonde, F. Légaré, F. Vidal and J. C. Kieffer. ‘Damage and ablation thresholds of fused-silica in femtosecond regime’. In: *Physical Review B* 84.9 (2011), p. 094104. DOI: 10.1103/PhysRevB.84.094104.
- [132] S. Bennett. ‘Log-Logistic Regression Models for Survival Data’. In: *Applied Statistics* 32.2 (1983), p. 165. DOI: 10.2307/2347295.
- [133] M. Reid. *MatthewReid854/reliability: v0.5.1*. Version v0.5.1. 2020. DOI: 10.5281/ZENODO.3938000.
- [134] W. Weibull. ‘A statistical distribution function of wide applicability’. In: *Journal of Applied Mechanics* (1951).
- [135] D. Strickland and G. Mourou. ‘Compression of amplified chirped optical pulses’. In: *Optics Communications* 56.3 (1985), pp. 219–221. DOI: 10.1016/0030-4018(85)90120-8.
- [136] R. W. Boyd. *Nonlinear Optics: Third Edition*. 2008. ISBN: 978-0-12-369470-6.
- [137] V. Nathan, S. S. Mitra and A. H. Guenther. ‘Review of multiphoton absorption in crystalline solids’. In: *Journal of the Optical Society of America B* 2.2 (1985), p. 294. DOI: 10.1364/JOSAB.2.000294.
- [138] M. Royon. ‘Ingénierie de verres de silice : influence de pré-traitements sur la variation d’indice de réfraction de guides d’ondes photo-inscrits par laser femtoseconde’. PhD thesis. 2018.
- [139] L. Keldysh *et al.* ‘Ionization in the field of a strong electromagnetic wave’. In: *Soviet Physics-JETP [translation of Zhurnal Eksperimentalnoi i Teoreticheskoi Fiziki]* 20.5 (1965), pp. 1307–1314.
- [140] R. R. Gattass and E. Mazur. ‘Femtosecond laser micromachining in transparent materials’. In: *Nature Photonics* 2.4 (2008), pp. 219–225. DOI: 10.1038/nphoton.2008.47.
- [141] O. Bernard, E. Audouard, B. Schöps, M. Delaigue, G. Dalla-Barba, K. Mishchik, C. Hönninger and E. Mottay. ‘Efficient micro processing with high power femtosecond lasers by beam engineering and modelling’. In: *Procedia CIRP*. 10th CIRP Conference on Photonic Technologies [LANE 2018] 74 (2018), pp. 310–314. DOI: 10.1016/j.procir.2018.08.121.
- [142] H.-P. Chung, P. Kumar, K. Wang, O. Bernard, C. Shirpurkar, W.-C. Su, T. Pertsch, A. A. Sukhorukov, Y.-H. Chen and F. Setzpfandt. ‘Spectral mapping of polarization-correlated photon-pair sources using quantum-classical correspondence’. In: *arXiv:2007.00880 [physics, physics:quant-ph]* (2020).
- [143] O. Bernard. ‘Controlling inscription in bulk dielectrics using femtosecond laser irradiation through adaptive predictive modelling.’ Dresden, D, 2022.

- [144] O. Bernard, A. Kraxner, A. Boukhayma, A. Golparvar, Y. Bellouard and C. Enz. ‘Towards in situ monitoring and feedback control of femtosecond laser-induced nanogratings formation in dielectrics’. In: *Ablation, Drilling and Cutting*. Lasers in Manufacturing 2021. online: WLT e.V., 2021.
- [145] O. Bernard. ‘In-situ monitoring of femtosecond laser-induced modifications in dielectrics using digital holographic microscopy’. Orlando, FL, USA, 2019.
- [146] Y.-X. Lin, C.-H. Lee, H.-P. Chung, M. Younesi, P. Kumar, K. Wang, O. Bernard, C. Shirpurkar, W.-C. Su, R. Geiss, T. Pertsch, A. Sukhorukov, F. Setzpfandt and Y.-H. Chen. ‘Integrated Photonic Sources and Circuits in Lithium Niobate Platform’. In: *26th Optoelectronics and Communications Conference*. Optoelectronics and Communications Conference. Hong Kong: Optica Publishing Group, 2021, T2D.2. ISBN: 978-1-943580-92-7. DOI: 10.1364/OECC.2021.T2D.2.
- [147] H.-P. Chung, P. Kumar, K. Wang, O. Bernard, C. Shirpurkar, W.-C. Su, T. Pertsch, A. Sukhorukov, Y.-H. Chen and F. Setzpfandt. ‘Spectral mapping of an integrated type-II photon-pair source using quantum-classical correspondence’. In: *Frontiers in Optics + Laser Science APS/DLS*. Frontiers in Optics. Washington, DC: OSA, 2019, JTu3A.46. ISBN: 978-1-943580-67-5. DOI: 10.1364/FIO.2019.JTu3A.46.

Curriculum vitae

Olivier Bernard
born 7 April 1995
French citizen

Caroline 17
CH-1003 Lausanne (Switzerland)
olivierbernard033@gmail.com

professional experience

2018–2023	doctoral assistant Galatea laboratory, IEM, STI École polytechnique fédérale de Lausanne, Neuchâtel, CH
2017–2018	junior R&D engineer, and MSc work Amplitude Laser Group, Pessac, F <i>analytical modelling of femtosecond laser ablation of metallic surfaces</i>
2017	research intern Nano-optics group, IAP, Friedrich-Schiller-Universität Jena, Jena, D <i>developing a characterisation setup for entangled photon sources</i>
2016	research intern, and BSc work LOMA, UMR-5798, CNRS, Université de Bordeaux, Talence, F <i>automatising, and data processing of thermal characterisation of thin films</i>

education

2018–2023	Doctoral programme in advanced manufacturing École polytechnique fédérale de Lausanne, Lausanne, CH
2016–2018	MSc in instrumental physics Université de Bordeaux, Talence, F
2013–2016	BSc in physics Université de Bordeaux, Talence, F

publications

- peer reviewed
 - O. Bernard and Y. Bellouard. 'On the use of a digital twin to enhance femtosecond laser inscription of arbitrary phase patterns'. In: *Journal of Physics: Photonics* 3.3 (2021), p. 035003. ISSN: 2515-7647. DOI: 10.1088/2515-7647/abf743

- O. Bernard, E. Audouard, B. Schöps, M. Delaigue, G. Dalla-Barba, K. Mishchik, C. Hönniger and E. Mottay. 'Efficient micro processing with high power femto-second lasers by beam engineering and modelling'. In: *Procedia CIRP*. 10th CIRP Conference on Photonic Technologies [LANE 2018] 74 (2018), pp. 310–314. ISSN: 2212-8271. DOI: 10.1016/j.procir.2018.08.121
- pre-prints
 - O. Bernard, A. Kraxner, A. Boukhayma, C. Enz, Y. Bellouard and J. Squier. *Third-harmonic generation monitoring of femtosecond laser-induced in-volume functional modifications*. preprint. 2023. DOI: 10.1364/opticaopen.22040459.v1
 - H.-P. Chung, P. Kumar, K. Wang, O. Bernard, C. Shirpurkar, W.-C. Su, T. Pertsch, A. A. Sukhorukov, Y.-H. Chen and F. Setzpfandt. 'Spectral mapping of polarization-correlated photon-pair sources using quantum-classical correspondence'. In: *arXiv:2007.00880 [physics, physics:quant-ph]* (2020)
- conferences
 - O. Bernard. 'Controlling inscription in bulk dielectrics using femtosecond laser irradiation through adaptive predictive modelling.' 25th Congress of the International Commission for Optics (ICO) / 16th International Conference on Optics Within Life Sciences (OWLS). Dresden, D, 2022
 - O. Bernard, A. Kraxner, A. Boukhayma, A. Golparvar, Y. Bellouard and C. Enz. 'Towards in situ monitoring and feedback control of femtosecond laser-induced nanogratings formation in dielectrics'. In: *Ablation, Drilling and Cutting*. Lasers in Manufacturing 2021. online: WLT e.V., 2021
 - O. Bernard. 'In-situ monitoring of femtosecond laser-induced modifications in dielectrics using digital holographic microscopy'. ICALEO, Laser Nanomanufacturing (Nano). Orlando, FL, USA, 2019
- proceedings
 - Y.-X. Lin, C.-H. Lee, H.-P. Chung, M. Younesi, P. Kumar, K. Wang, O. Bernard, C. Shirpurkar, W.-C. Su, R. Geiss, T. Pertsch, A. Sukhorukov, F. Setzpfandt and Y.-H. Chen. 'Integrated Photonic Sources and Circuits in Lithium Niobate Platform'. In: *26th Optoelectronics and Communications Conference*. Optoelectronics and Communications Conference. Hong Kong: Optica Publishing Group, 2021, T2D.2. ISBN: 978-1-943580-92-7. DOI: 10.1364/OECC.2021.T2D.2
 - H.-P. Chung, P. Kumar, K. Wang, O. Bernard, C. Shirpurkar, W.-C. Su, T. Pertsch, A. Sukhorukov, Y.-H. Chen and F. Setzpfandt. 'Spectral mapping of an integrated type-II photon-pair source using quantum-classical correspondence'. In: *Frontiers in Optics + Laser Science APS/DLS*. Frontiers in Optics. Washington, DC: OSA, 2019, JTU3A.46. ISBN: 978-1-943580-67-5. DOI: 10.1364/FIO.2019.JTU3A.46